EVANESCENT FIELD SENSING IN HYBRID INTEGRATED OPTICAL MEMS DEVICES

Geert Altena
Evanescent field sensing in hybrid integrated optical MEMS devices
Ph. D. Thesis University of Twente, June 2006
ISBN: 90-365-2361-3
Copyright © 2006 by G. Altena, Enschede, The Netherlands

Typeset by the author with LaTeX

The work described in this thesis was performed at the Integrated Optical MicroSystems group of the Faculty of Electrical Engineering, Mathematics and Computer Science, University of Twente, The Netherlands. It was part of OCMMM research project funded by the European Committee under project number IMS-1999-00014.

EVANESCENT FIELD SENSING IN HYBRID INTEGRATED OPTICAL MEMS DEVICES

PROEFSCHRIFT

ter verkrijging van
de graad van doctor aan de Universiteit Twente,
op gezag van de rector magnificus,
prof.dr. W.H.M. Zijm,
volgens het besluit van het College voor Promoties
in het openbaar te verdedigen
op woensdag 7 juni 2006 om 13:15 uur

door

Geert Altena

geboren op 26 maart 1974
te Doetinchem.

Dit proefschrift is goedgekeurd door:
de promotor: Prof. Dr. P.V. Lambeck
de assistent-promotor: Dr. H.J.W.M. Hoekstra

Contents

Contents **i**

Preface **v**

1 Introduction **1**
- 1.1 On-chip techniques 2
- 1.2 Planned demonstrators 9
- 1.3 Task definition 13
- 1.4 Organisation of thesis 14

2 Theory **17**
- 2.1 Analysis of the effects using loss free materials 18
- 2.2 Implementation of the ray picture model 26

3 Free-standing membrane waveguides **29**
- 3.1 Choice of the membrane material 29
- 3.2 Preliminary experiments 32
- 3.3 The final tapered membrane section 38
- 3.4 Summary 43

4 The micro-mirror demonstrator **45**
- 4.1 Introduction 45
- 4.2 Qualitative Analysis 48
- 4.3 Quantitative analysis 51
- 4.4 Influence of IO wafer on the electrical field 57
- 4.5 New technological challenges 58
- 4.6 The final design and the realisation of the structures. 65
- 4.7 Characterisation of the mirror demonstrator 68
- 4.8 Measurement of the relation between actuation voltage and optical transmission losses 70
- 4.9 Summary 72

5 The PZT Membrane demonstrator **73**
5.1 MEMS characteristics 73
5.2 Relevant properties of the membrane devices 73
5.3 Requirements to the read out of the membrane system . . . 74
5.4 The design of the PZT-membrane demonstrator 74
5.5 Summary 79

6 The MEMS gyroscope demonstrator **81**
6.1 Introduction 81
6.2 MEMS gyroscopes 83
6.3 Analysis 86
6.4 The structural parameters of the IO structure 97
6.5 The structure of the demonstrator device 102
6.6 Fabrication process 104
6.7 MOEMS in which the MEMS is a Si wafer containing Si membranes 109
6.8 Characterisation of the MEMS 113
6.9 Read out of Si-plate movements by monitoring the throughput of a free-standing waveguiding channel 122
6.10 Discussion 127

7 Summary **129**
7.1 Summary of the main results 129
7.2 General evaluation of the research presented in this PhD thesis 134

A Bonding techniques **137**
A.1 Silicon-fusion bonding 137
A.2 SU-8 polymer bonding 138

B Process scheme for fabrication of MZI demonstrator **141**

C Sourcecode listings of used Matlab programs **145**
C.1 Main program 145
C.2 Auxiliary program 148

D Electrical Through Wafer Interconnects **151**

E Processflow for the IO wafer of the attenuation based demonstrator **155**

F Processflow for creating the silicon membranes **159**

Bibliography **161**

Publications **167**

Samenvatting (Dutch) **169**
Samenvatting van de belangrijkste resultaten 169
Algemene evaluatie van het onderzoek gepresenteerd in dit proefschrift 174

Dankwoord **177**

Biografie **179**

Preface

The work reported in this thesis was performed within the framework of the European Community (EC) project entitled 'Optical Characterisation Methods for MEMS Manufacturing' (OCMMM) funded under the Competitive and Sustainable Growth program (GROWTH) in order to develop new testability procedures for the characterisation of mechanical behaviour of Micro-Electro-Mechanical Systems (MEMS). This project has been carried out in the period 2001 - 2004.

The general objective of the project is mainly to respond to the increasing need for testability techniques of MEMS components, during the development of the micro-mechanical structures, their production and assemblage and during the life cycle of the completed product. As formulated in the OCMMM proposal, the development of novel or improved testing methods is expected to contribute to the achievement of more general goals such as

- a reduction of the cost of developing and producing MEMS products;
- an increase of the yield in industrial MEMS fabrication;
- an improvement of the quality and especially the reliability of MEMS products;
- an increase of the acceptance and application of MEMS products by industry.

In this project the testing implies an optical characterisation of the static and dynamic behaviour of moving parts in MEMS devices and the results of the project have to indicate (the limits of) the performance and the prospects of the application of several optical methods for measuring displacement and/or deformation of mechanical parts of MEMS devices. The absence of any practical influence of probing light beams on the MEMS properties in most optical characterisation methods can be considered as one of the principal strong points of optical probing and, as a consequence, the

application of optical testing methods in general will play second fiddle in the design the MEMS structure. Notice here, for example, that in capacitive methods the moving part has to be loaded with an electrode, potentially changing the properties of the moving part or affecting the MEMS device as a whole.

The optical techniques investigated within the project are divided into two categories:

- 'On-chip' techniques, using integrated optics (IO), expected to deliver information on a weighted average of the displacement of a moving or moved MEMS part;
- 'full-field' techniques, using external full-field interferometry, delivering information on the full spatial distribution of the deformation of the moving MEMS part.

A large number of partners were gathered into a consortium, each partner having his specific expertise. The consortium consisted of:

- Research institutes:
  - Université de Franche-Comté, Département d'Optique P.-M. Duffieux (LOPDM), Besançon, France, Project coordinator;
  - University of Twente, Integrated Optical MicroSystems group of the MESA^{+} institute for nanotechnology (MESA), Enschede, The Netherlands;
  - Fraunhofer Gesellschaft zur Förderung der angewandten Forschung e.V. (IWU), Chemnitz, Germany;
  - Chemnitz University of Technology / Center of Microtechnologies (TUC), Chemnitz, Germany;
  - Warsaw University of Technology (WUT), Warsaw, Poland.
- Large companies:
  - Thales Avionionics (TH-AV), Valance, France
  - Thales Research & Technology (TH-RT), Paris, France
- Small and Medium sized Enterprises (SME's):
  - GF Messtechnik (GFM), Berlin, Germany
  - LioniX (LION), Enschede, The Netherlands

– Yole Développement (YOLE), Lyon, France

The MESA contribution to the project was mainly incorporated in one of the work packages defined within the 'on-chip' area; evanescent field based methods. MESA was also coordinating this work package. The research of MESA in this work package forms the basis of this PhD thesis.

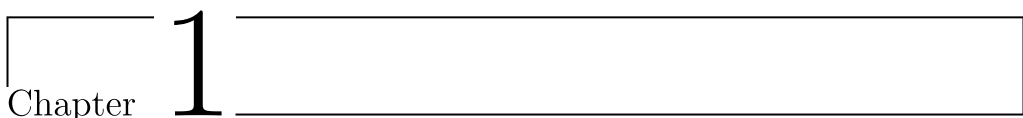

Introduction

Testing of MEMS systems is required during R&D, during fabrication and during use (life cycle). And indeed, the optical testing methods, which will be developed and investigated in the OCMMM project, aim at providing means for testing during all these three stages.

Optical external full-field measurement methods requiring bulky and expensive equipment are rather well suited for application at manufacturers site, implying their use during R&D and fabrication; they require free entrance of free space beams to the moving parts of the MEMS, which hampers their use in packaged MEMS. For monitoring performance of the MEMS during practical application (life cycle), integrated optics is expected to be used fruitfully.

Due to their nature – they need similar production methods and their dimensions are in the same order of magnitude as the MEMS – integrated optical structures (optical chips) can be closely integrated with the MEMS. The costs of IO based read out systems are expected to be low compared to the full field equipment and continuous in-situ monitoring of the (spatially averaged) position of the moving part during MEMS application is expected to be feasible. Notice however that the information obtained from full field methods will be much richer than that obtained from integrated optics: a spatially resolved displacement pattern versus a (spatially weighted) average value of the displacement. If needed, IO methods can be calibrated using full field methods. For all methods performance aspects like range, resolution and reliability are very relevant. In this EC project, the research performed by MESA was on the area of read out by integrated optics and so we will not discuss the full field methods anymore.

1.1 On-chip techniques

Read out of displacements by guided beams propagating within an integrated optical system requires that, as a result of the displacement, in a section of an IO channel the spatial distribution of the (complex) refractive index is changed. Notice that the imaginary part of the refractive index represents optical losses. This change of refractive index distribution manifests itself as a change of one or more characteristics of the mode propagating through that channel section. Appropriate IO circuitry enables a conversion of the change of modal characteristics into a change of output power, where the information can be presented as the value of a output power of a single output channel or can be coded in the spatial or time domain.

Many types of such conversion circuits are known and many information about principles, implementation and performance of such circuits have been reported in literature. Already in the definition stage of the project it had been decided to apply the SiON technology for realising the integrated optical systems. This technology has been chosen for various reasons: on the one hand it is a flexible technology, which is expected to be well compatible with the technologies commonly used in realising MEMS systems, on the other hand, in the MESA+ institute a well controlled SiON technology had already been developed by the IOMS-group.

To give an impression of the structure of an IO channel realised in SiON technology, we present in Figure 1.1(a) a monomodal channel which is usually applied in the IOMS group for chemical IO sensors. This structure has been optimised for application in so-called evanescent field based homogeneous type chemical IO sensors. Because application requirements for read out of displacements in specific MEMS devices are expected to be different from those of the chemical sensors it can be envisaged that the optimal channel structures will also be different.

From Maxwell theory it has been derived that the propagation of a guided mode through a straight channel (see Figure 1.1(b)) with a z-invariant refractive index distribution can be mathematically described as

$$\vec{E}(x,y,z,t) = \vec{E}(x,y)e^{-\jmath k_0 \bar{N}_{\mathrm{eff}} z} e^{\jmath \omega t} \tag{1.1}$$

$$\vec{H}(x,y,z,t) = \vec{H}(x,y)e^{-\jmath k_0 \bar{N}_{\mathrm{eff}} z} e^{\jmath \omega t} \tag{1.2}$$

With:

$\vec{E}(x,y,z,t)$ the complete electrical field distribution

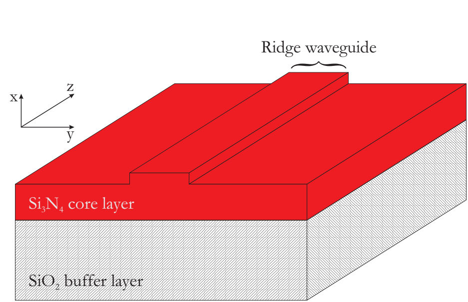

(a) Illustration of a monomodal channel waveguide

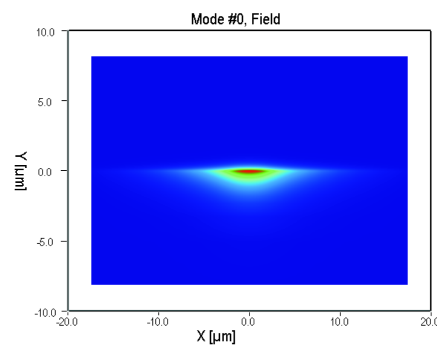

(b) Calculated mode profile of the fundamental TE mode propagating in the waveguide shown in Figure 1.1(a)

Figure 1.1: A channel waveguide and its calculated fundamental TE mode

$\vec{E}(x, y)$ the transverse field distribution, the so-called *field profiles*, independent of z and t

k_0 $(=\frac{2\pi}{\lambda})$ the free space wave-number with λ the free space wavelength

$\bar{N}_{\mathbf{eff}}$ $(= N'_{\text{eff}} + \jmath N''_{\text{eff}})$ the effective refractive index or modal index

For every value of the wavelength of the applied light the maximum number of modes that can propagate through the channel and all modal (wavelength dependent) parameters are completely given by the spatial distribution of the (complex) refractive index in the regions through which the mode is propagating. In most IO sensors there are good reasons to apply monomodal channels and monochromatic light only. For most types of (complex) refractive index distributions commercial software, the so-called mode solvers, are available to calculate all modal parameters.

For very simple systems such as three-layer slabguides (see Figure 1.2), the field profiles can be given as a analytical function of the structural parameters and the effective refractive index N_{eff}.

Here we have to distinguish between so-called TE and TM modes, being characterised by having one single component of the electric and magnetic field respectively (a transverse component parallel to the material boundaries) and two components of the other field orthogonal to the first one. (In general the longitudinal component is relatively small). If one of the components is known, Maxwell's theory delivers the means to calculate from that all other ones. So, generally field profiles are given for the transverse

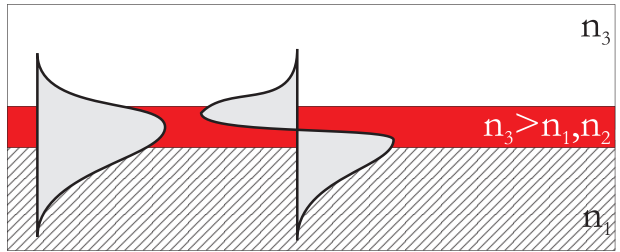

Figure 1.2: Illustration of a three-layer slab waveguide with the transverse field profiles of two propagating modes.

component only, the E-field for TE modes and the H-field for TM modes. In the channel guides the TE- and TM- character is an approximation only, but in the type of channels we shall use finally, it is a very good approximation. For illustration, we present here the formulas for the field profiles of the TE mode of a monomodal slabguide.

$$E_{y,1}(x) = A_1 e^{-\bar{k}_{x,1}x} \tag{1.3}$$
$$E_{y,2}(x) = C e^{\jmath k_{x,2}x} + D e^{-\jmath k_{x,2}x} \tag{1.4}$$
$$E_{y,3}(x) = A_3 e^{\bar{k}_{x,3}x} \tag{1.5}$$

with

$$\bar{k}_{x,1} = k_0\sqrt{N_{\text{eff}}^2 - n_1^2} \tag{1.6}$$
$$k_{x,2} = k_0\sqrt{n_2^2 - N_{\text{eff}}^2} \tag{1.7}$$
$$\bar{k}_{x,3} = k_0\sqrt{N_{\text{eff}}^2 - n_3^2} \tag{1.8}$$

and A_1, C, D and A_3 being constants whose values can be calculated from boundary conditions.

Notice the exponential decay of the fields in both outer layers. These decaying fields are called *evanescent fields* and their decay length is given as

$$l_{\text{decay}} = \frac{1}{k_0\sqrt{N_{\text{eff}}^2 - n_{1,3}^2}} \tag{1.9}$$

A similar exponential decay occurs in the channel guides. In Figure 1.1(b), the field profile of the fundamental TE mode propagating through the monomodal channel, as defined in Figure 1.1(a), is given.

Sensing generally relies on a measurand induced change of the (complex) refractive index distribution within the modal field region. A change of the real part of the refractive index distribution manifests itself always as a change of the real part of N_{eff} and a change of the field profile (although the latter generally can be neglected); in some special cases and such a case will be met in this PhD thesis it also causes a change of the imaginary part of the effective refractive index. Changes of the imaginary part of the refractive index distribution always influence the value of the imaginary part of the effective refractive index (and hence the modal attenuation) while its influence on the real part of the N_{eff} and on the field profile are generally negligible. In this PhD thesis we shall also meet systems in which the real and the imaginary part of the refractive index distribution are changing simultaneously and as a consequence both the change of the real part as well of the imaginary part of N_{eff} have to be considered.

During definition of the project it has been envisaged that in most of the intended measurement methods the change of the real part of the N_{eff} will be dominant and that it is this change which has to be read out. It had been decided in advance to apply for this read out preferentially an IO Mach-Zehnder Interferometer (MZI) circuit. Main reasons for this decision have been the easy implementation of the bare MZI circuit, its good performance (especially a very good resolution) and the experience of both integrated optical groups (MESA and LOPMD) with these systems. Because these circuits will be applied in this project in practise we now give a short description.

A schematic top view of an IO MZI is shown in Figure 1.3. At the first junction, the light from the input channel is divided over two branches. After a certain length, the two channels are combined again, leading to an interference of the beams exiting the two individual branches. This interference results in a output power that is dependant on the phase difference of the two beams. For sensing applications, usually the phase in one of the branches (termed *reference* branch) is left unperturbed; the phase in the other branch (*signal* branch), and hence the phase *difference*, is made (within an interaction window of length L_{int}) dependant on the measurand.

When in the interaction window the refractive index distribution changes within the evanescent field region (due to the measurand), this results into a change of the effective index N_{eff} of the guided mode in the branch and hence into a phase change $\Delta\varphi_{\text{m(easurand)}}$:

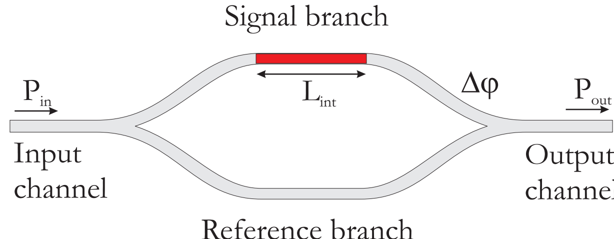

Figure 1.3: Schematic illustration of the MZI principle. The sensing branch (top) contains an interaction window of length L_{int}.

$$\Delta\varphi_m = \frac{2\pi}{\lambda_0} L_{\text{int}} \Delta N_{\text{eff}} \tag{1.10}$$

It can be shown that, assuming perfect technology, a monochromatic light source and single-mode operation, the output power of the MZI depends on $\Delta\varphi_m$ and can be written as:

$$P_{\text{out}} = \frac{1}{2} P_{\text{in}} (1 + \cos(\Delta\varphi_m) \tag{1.11}$$

The transfer function, that is, the ratio of the output power and the input power $P_{\text{out}}/P_{\text{in}}$ is shown as a function of $\Delta\varphi_m$ in Figure 1.4. From this function, $\Delta\varphi_m$ can be derived when the input power is known.

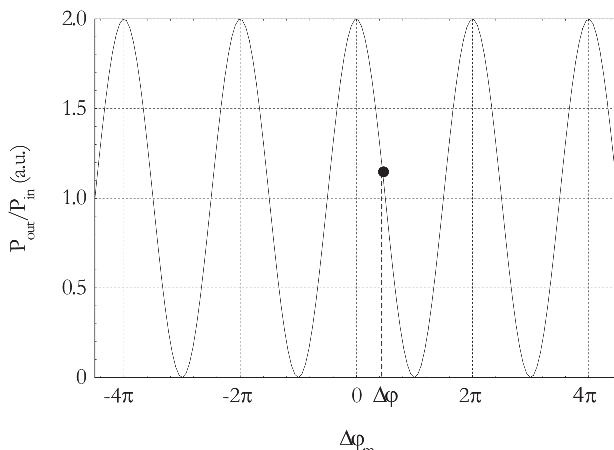

Figure 1.4: Plot of the transfer function of the MZI versus the phase difference φ_m.

The resolution of such basic MZI implementation is, in terms of ΔN_{eff}, approximately $10^{-6} - 10^{-7}$. When an electro-optic *serrodyne* modulator is implemented within the MZI structure, as proposed in [HL99], the resolution can be improved to 6×10^{-9}. In addition, this modulation method eliminates several intrinsic and technological problems associated with the basic MZI implementation.

The on-chip measurement methods which will be investigated can be divided in two classes termed 'loaded' and 'unloaded'. Both classes will be described in the next section.

The 'unloaded' class

In the unloaded class, the MEMS part is moving into or within the evanescent field region of a channel mode (see Figure 1.5) and the change of the refractive index distribution in the modal field region will depend on the change of the position of the lower boundary of the moving MEMS part. Here we meet a special modification of the evanescent field sensing principle. This principle is mostly applied for determining concentrations of chemical compounds in gasses or solutions. Within the IOMS group, much research has been performed on these IO chemical sensors and knowledge gained over there can be fruitfully applied in investigations about the IO-MEMS measuring systems. This special modification has been introduced by Lukosz et al. [Luk92] in the nineties, but has not been worked out in full detail nor has it been applied in practical systems. Notice that this method can be utilised not only for sensing but also for actuating. In the latter case one aims at a well controlled change of N_{eff}, which can be utilised in optical telecommunication, for example, for the switching of signals from one channel to the other (IO switches such as the digital optical switch [Luk92, DL97, DL98]), for tuning of wavelength filters applied for wavelength demultiplexing [Luk92, GL97, GL98] or in optical sensing, for example, as an acoustical sensor [PL91, PL94].

This method affords for a hybrid integration of a MEMS chip and an IO chip, for example, by bonding (permanent bond) or possibly by pressing even (non-permanent bond) both chips together. Conditional for this however, is that the moving part is positioned at the outside of the MEMS device in that way enabling to be driven into the evanescent field extending from the outside of the IO chip. Permanent bonded hybrids can be utilised in monitoring the life cycle during use, while non-permanent bonded systems may be used for intermediate characterisation during the production stage. In these hybrids the integrity of the MEMS is maintained.

A schematic picture of such a hybrid system is given in Figure 1.5

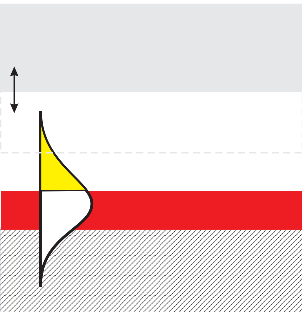

Figure 1.5: Mechano-optic evanescent field sensing

The 'loaded' class

In the loaded class, the integrated optical layer structure is deposited on top of the moving part (monolithic integration). This method can be used only if the moving part shows some deformation (for example, a vibrating membrane). An example of such a loaded type system is shown in Figure 1.6.

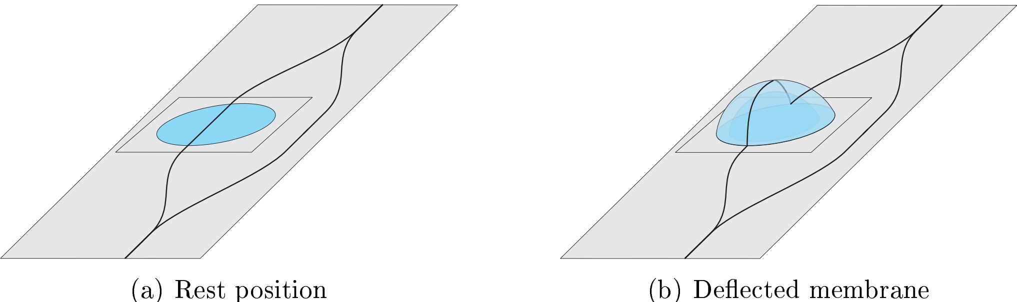

(a) Rest position (b) Deflected membrane

Figure 1.6: Illustration of a loaded type demonstrator

The figure shows a vibrating membrane consisting of a thin layer of silicon on top of which the optical films have been deposited. In these films a Mach-Zehnder Interferometer (MZI) is defined; one of the branches of the MZI, the sensing branch, runs across the vibrating membrane, the other branch, the reference branch, runs outside the membrane. When the middle of the originally flat Si membrane is displaced perpendicularly to the membrane plane, the membrane will deform. As a consequence the optical path of the light in the signal branch is elongated. In addition, the channel will contract somewhat along the transverse direction and the stress distribution within the optical channel will change. Both latter factors immediately lead to a change of the N_{eff} of the propagating mode. All

three effects together will cause a change of the phase difference between the modes in both branches and hence also cause a change of the output power of the MZI.

For both methods, further in-depth analysis is required for calculating the relation between the optical output signal and the displacement of the moving MEMS-part.

Comparison of the different characterisation methods

In table 1.1 the two on-chip methods have been compared as to their most relevant aspects. In addition, the respective aspects for the full-field methods have been included in the table.

Table 1.1: Comparison of the OCMMM characterisation methods

Method	Obtained information	production phase	MEMS requirements	MEMS integrity
full-field	total distribution	R&D, production	moving part accessible to detection beam	++
loaded type	average value	life time	MEMS fabrication allows integration of IO fabrication steps	-
unloaded type	average value	life time, production	outer surface suitable for wafer bonding	+

In the framework of the OCMMM project MESA should focus on the evanescent field based sensing method, while University of Besançon should concentrate on the other class of IO sensing methods, the loaded systems. Results of the latter have been reported by Şabac [Ş04].

1.2 Planned demonstrators

For showing the feasibility of evanescent field sensing as a means for MEMS testability static and dynamic measurements of displacements of moving parts in three different MEMS devices are aimed at. These MEMS are:

- an electrostatically driven rotating micromirror as developed by TUC;
- a piezo-electrically driven vibrating membrane as developed by Thales-RT;
- a micromachined 'vibratory' gyroscope, as developed by Thales-AV.

In this section we shall give a qualitative description of these MEMS devices and we shall indicate which displacements have to be measured.

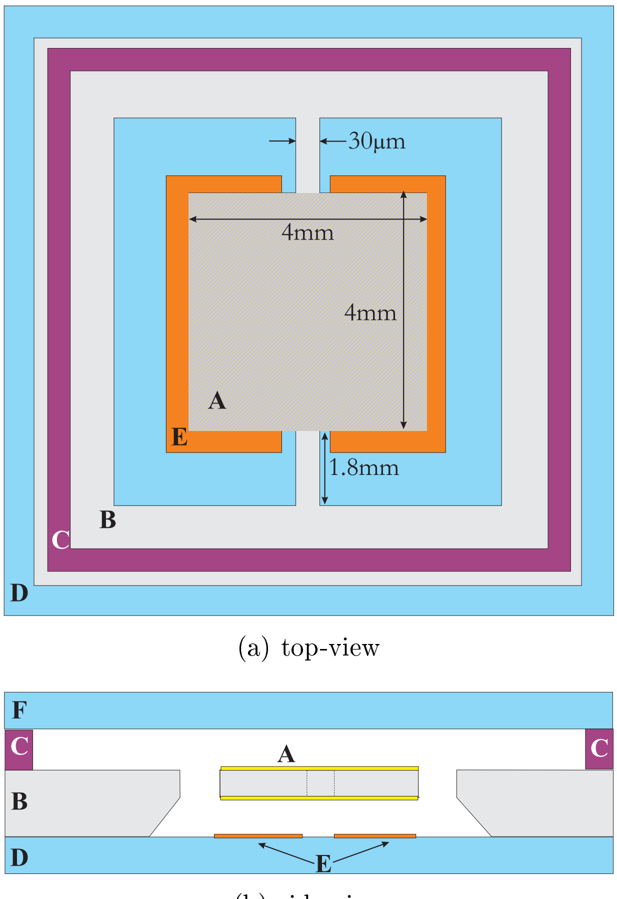

(a) top-view

(b) side-view

Figure 1.7: micro-mirror picture

The rotatable mirror

A schematic picture of a MEMS mirror as designed and produced by TUC [GKK+00] is presented in Figure 1.7.

Such a mirror system encompasses a thin silicon plate (A), coated with metal layers on the top and bottom side. The plate is connected to the bulk of the wafer (B) by two thin hinges only. The plate can be rotated over some degrees around the axis defined by the length direction of the hinges. The change of orientation is obtained by applying a voltage between the bottom side metal layer of the plate and a couple of electrodes (E) provided on top of a glass slide(D), which is properly bonded to the mechanical wafer. At the upper side the mirror wafer is bonded to an intermediate distance wafer (C) and the hole in that wafer is covered with a glass slide for protection. (see Figure 1.7(b)).

The aim of this structure is to reflect a light beam incident on the upper well-reflecting metal layer of the plate into a direction that is controlled by the rotation angle of the reflecting plate: a mirror enabling controlled reflection of an incident light beam into a desired direction. Arrays of such type of mirrors – but then implemented in a more complicated structure which affords for rotation along two mutual perpendicular axes – have been applied in optical telecommunication as switching matrices in between two bundles of optical fibers [APB+00]. TUC has developed a large series of these rotatable mirrors mutually differing in type and dimension of the hinges and in the dimensions of the rotatable mirror plate.

Aim of the demonstrator is to show the feasibility of an evanescent field based IO sensing structure hybridised with the MEMS system for measuring the rotation angle over the full angle range of the device with a resolution better than 1% (if possible 0.1%) of the full angle range. And this in the frequency range between zero (static) and a frequency somewhat higher than the resonance frequency of the mirror.

Piezo-electrically driven membranes

A schematic picture of a piezo-electrically actuated vibrating membrane device as produced by Thales-RT is presented in Figure 1.8.

These membranes are built as thin Si layers (A) on top of which a piezo-electrical (poled) PZT layer (B), sandwiched between two platinum electrodes (C and D), has been applied for driving the membrane. Thales-RT has developed many modifications of these membranes mutually differing in thickness, lateral shape and dimensions. Aim of the demonstrator is to show the feasibility of an evanescent field based IO sensing structure hybridised with such a MEMS system for measuring displacements of the middle of the membrane and to determine what best value of the resolution can be obtained. This in the frequency range 0 - somewhat higher than the resonance frequency of the fundamental mode of the membrane.

The MEMS Gyro device

A schematic picture of vibratory micro-gyroscope as has been developed by Thales-AV is presented in Figure 1.9.

The device is manufactured from a SOI (silicon-on-insulator) wafer using sacrificial layer etching. Both plates can vibrate in lateral direction by virtue of electrostatically driven comb-drives. A rotation of the whole system along the horizontal axis leads, as a result of Coriolis forces, to a contra-directional movement of both plates along the vertical directional.

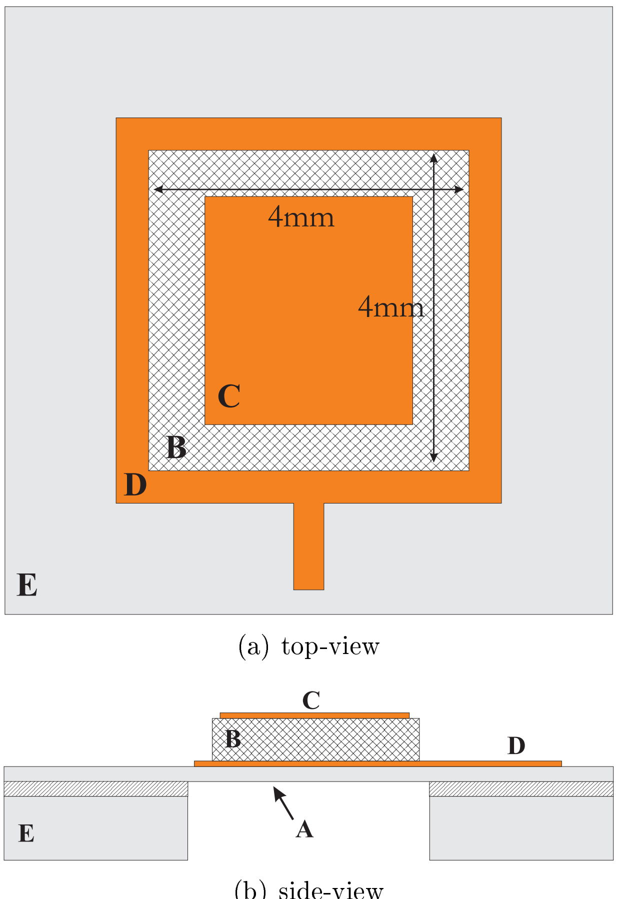

(a) top-view

(b) side-view

Figure 1.8: Schematic picture of the PZT membrane system

Effects are the largest if the resonance frequencies of the lateral and vertical movements of the plates are identical. Up to now these displacements have been determined from capacitive measurements. The aim of this part of the project is to investigate whether hybridisation of this device with an IO read out system may afford for the following two applications:

- Readout within a non-permanently bonded system, in which MEMS and IO system are pressed together, to be used for measuring the vertical resonance frequency during the production stage. Its difference to the lateral resonance frequency will define the duration of a subsequent technological process which aims at equalising both resonance frequencies.
- Read out of the vertical plate displacements during use. Here the IO system is added not for testing purposes but for sensing!

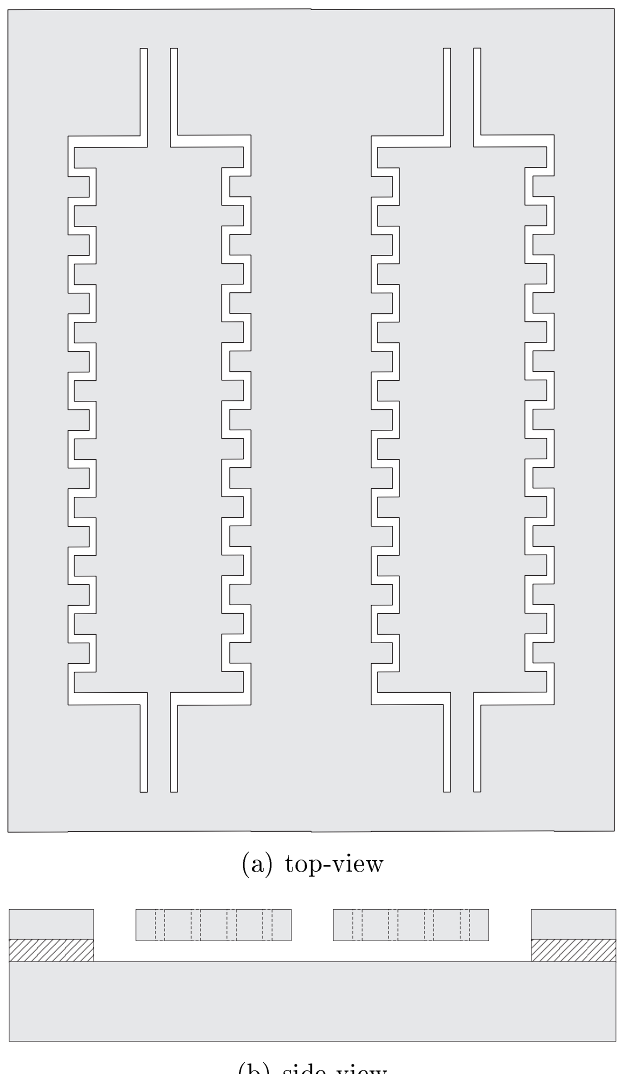

(a) top-view

(b) side-view

Figure 1.9: MEMS gyroscope

1.3 Task definition

The various tasks of the different partners within the development of the three demonstrator devices are listed below:

Micro-mirror demonstrator MEMS mirror systems of a given type have been designed, produced and characterised by TUC and a choice has to be made which of them is most suited for implementation in the demonstrator. Obtaining the required compatibility of the IO and

MEMS chip should be discussed by both partners. TUC should produce the MEMS, MESA design and produce the IO read out system, possible technological problems related to the bonding were of common concern, while the testing should be the task of MESA.

PZT Membrane demonstrator MEMS membrane systems, with piezoelectric PZT layers for actuation of the membrane, should be produced by Thales-RT, with, in principle, a further task division similar to that described for the mirror demonstrators.

MEMS Gyro demonstrator Production of MEMS gyro systems suited for hybridisation with an IO read out system was the responsibility of Thales-Av, again with a similar task division as in the other demonstrators.

After two years it was recognised that for practical demonstrators with high-resolution MZI read out, implementation of electrical feed-throughs (Electrical Through-Wafer Interconnects) in the optical wafers was required. The development and production of these feed-throughs became a task of Lionix. Reason for this, and the role played by the feed-throughs in the project, will be treated in more detail in chapter 4.

1.4 Organisation of thesis

The next chapter, Chapter 2, describes the theoretical background used to model the different demonstrators. It first gives a qualitative analysis of the waveguiding systems, outlining the principles of evanescent field sensing and the effects of using different MEMS materials. One of the main conclusions of the analysis is that free-standing membrane waveguides are required to achieve acceptable measurement ranges. Then, a quantitative analysis follows where a mathematical model based on the ray picture approach is presented, which be used in the following chapters to model the free-standing waveguide systems. Chapter 3 describes the activities performed to realise these free-standing waveguides in SiON technology. Different materials and fabrication methods are investigated followed by a study of the technologically feasible minimum thickness of such membrane waveguide. The chapter is concluded by a characterisation of the realised membranes in terms of surface roughness and insertion loss. Chapter 4 deals with the design, fabrication and characterisation of the first OCMMM demonstrator: the micro-mirror demonstrator. An analysis of the micro-mirror system, dealing, for

example, with geometry and materials, is given which sets several boundary conditions for the design of the optical circuitry. The consequences of these boundary conditions are discussed; the main conclusion is that a bridge-type waveguide comprising a free-standing membrane is required in this demonstrator. Then, the technological procedure for fabricating such bridge-type waveguides is described. Finally, the complete demonstrator and measurements performed with it are presented. The next chapter (5) describes the design of the optical circuitry for the second demonstrator: the PZT actuated membrane MOEMS. Unfortunately, the work on this demonstrator is limited to the design only as technology related problems with the MEMS component of the demonstrator, prevented its further development. Chapter 6 deals with the design, fabrication and characterisation of the last demonstrator: the MEMS gyroscope MOEMS. First, different sensing configurations are analysed to find the maximum achievable sensitivity. A 'common' type optical waveguide with an attenuation based sensing scheme is chosen. Then, a design of the optical part of the demonstrator is presented. Due to technological problems with the fabrication of the MEMS part of the demonstrator, the gyroscope, this demonstrator could not be finalised. However, alternative MEMS structures, designed to mimic the behaviour of the gyroscope, were fabricated and characterised. Results of these characterisations are presented next and these qualitatively show the operation of the optical parts; unpredictable behaviour of the alternative MEMS prevented a thorough quantitative analysis of these experimentally obtained data. The final chapter (7) presents a summary of the previous chapters and a general evaluation of the conducted research.

Chapter 2

Theory

When an object, for example, the moving part of a MEMS device, with refractive index n_{object} moves into or within the evanescent field of an optical waveguide, the effects on the effective index N_{eff} of the optical mode propagating in the waveguide are within two extremes:

a purely refractive effect the mode experiences a change in the real part of the effective index, N'_{eff}, only; conditions for this are $N'_{\text{eff}} < n_{\text{object}}$ and all materials are optically loss free.

a purely absorptive effect the imaginary part of N_{eff}, N''_{eff}, is affected only; condition for this is that the real part of n_{object} is exactly equal to the refractive index of the cladding of the unperturbed waveguide (for example, a solution), while its imaginary part is $\neq$ zero.

In practice these conditions will be never met exactly and as a consequence both the real and imaginary part of N_{eff} will be affected, but often one of both changes will be dominant. Most IO sensing circuits measure a change of whether the real or the imaginary part of N_{eff}, and a minor simultaneous change of the other part is considered as a small perturbation of which the effects have to be minimised. For example when using a refractive sensor like the Mach-Zehnder interferometer one has to optimise the optical structure in the sensing region to large changes of N'_{eff} and small changes of N''_{eff} or one has to rely on the MZI modification [HL99] which is nearly insensitive to changes of N''_{eff}. Notice also that in measuring modal attenuation the sensitivity to changes of N'_{eff} is generally small. So in future analysis it is fruitful not only to consider the originally intended MZI as basic sensor circuit but also to pay attention to measuring the attenuation.

In next sections we will present a general analysis of the $\bar{N}_{\text{eff}}$ changes caused by a change of the refractive index distribution in the evanescent field

region caused by a moving object. In this analysis, we will assume that the lower boundary of the moving object is parallel to the upper boundary of the core layer of the waveguide. Systems without this parallelism can be approximated as consisting of a series of small parallel sections, each section having another distance between both aforementioned plane boundaries.

2.1 Analysis of the effects using loss free materials

At first we shall consider slab type systems consisting of loss free materials. We will start with presenting a qualitative discussion, based on the ray model because in our opinion this offers a clearer picture than the Maxwell theory. We will rely on the resonance condition as given by the ray picture which is given as

$$\psi_0 = 2d_c n_c k_0 \cos(\theta) + \varphi_{c,cl} + \varphi_{c,b} + 2\pi m = 0 \tag{2.1}$$

where k_0, n_c, d_c, $\varphi_\mathrm{c,cl}$ and $\varphi_\mathrm{c,b}$ denote the vacuum wave number, the core refractive index, the core thickness and the phase jumps at total reflection of light at the core-cladding and core-buffer interface, respectively. θ is the angle of the incident ray and $m = 0, 1, \ldots$ indicates the mode order.

Even with loss free materials , the effective refractive index can be a complex quantity. We have to distinguish two types of systems:

Systems in which $N'_\mathrm{eff} > n_\mathrm{object}$ The total reflection condition is conserved. In the ray picture, a ray hitting the upper boundary of the core layer will be totally reflected by the layer stack above this boundary. The phase jump as a result of this reflection remains real, the mode remains perfectly guided and N_eff remains a real quantity.

Systems in which $N'_\mathrm{eff} < n_\mathrm{object}$ At the lower boundary plane of the object, the total reflection is frustrated and part of the incident power will be transmitted by this boundary as free space radiation. At that boundary, power leaks away. As a consequence, the mode becomes a *leaky* mode. Both the reflection coefficient and the phase jump at reflection at the upper boundary of the core layer become complex quantities and as a consequence, N_eff also becomes complex.

Qualitative analysis

We will first present a qualitative analysis of the first type of systems and here we will start from the low loss monomodal SiON waveguiding structures commonly used in chemical sensing. They consist of a Si_3N_4 (Silicon-Nitride) waveguiding core layer on top of a SiO_2 (Silicon-dioxide) buffer layer (as shown in Figure 2.1) and wether a SiO_2 or an air cladding.

These structures can be approximated as purely refractive sensing systems provided that $n_{\text{object}} < N'_{\text{eff}}$. In monomodal slabguides of this type with an air cladding, the N_{eff} of the TE_0 mode (at 1550 nm wavelength) can be calculated by to be in between $n_{SiO_2} = 1.457$ (cut-off of the fundamental mode) and 1.852 (cut off of the first order mode). The range of these N'_{eff} values can be realised by choosing a value of the thickness of the core layer in between 119 nm and 688 nm. So, to guarantee purely refractive sensing, it is safe to choose $n_{\text{object}} < 1.457$. However, the number of suitable materials is small, for example, (porous) SiO_2 or teflon-materials (polytetrafluoroethylene, $n \sim 1.30$).

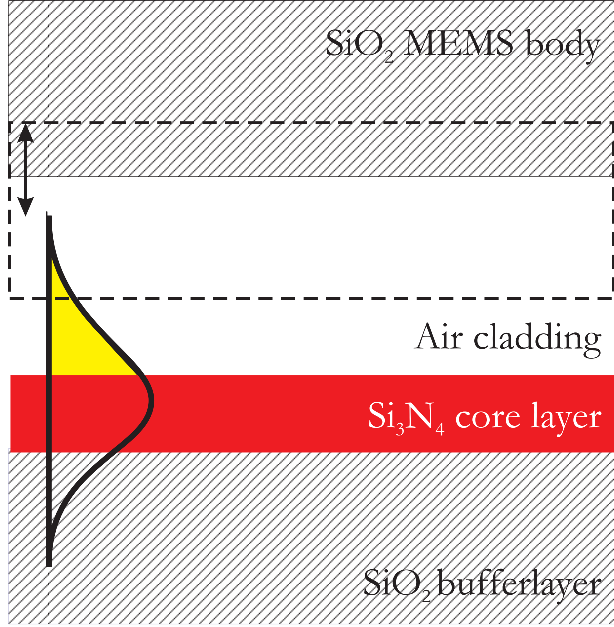

Figure 2.1: Illustration of the evanescent field sensing principle using a common type waveguide

For illustration purposes we have calculated using a common mode solver [McD], for several values of the core thickness, the relation between N'_{eff} and the distance between the upper boundary of the core layer and the lower

boundary of the object, the so-called air gap z_0. The wavelength λ_0 is chosen to be 1550 nm. The object will consist of thermally oxidised SiO_2 ($n = 1.457$ at $\lambda = 1550$ nm), a material often used in MEMS structures. A representative result ($t = 150$ nm)is given in Figure 2.2.

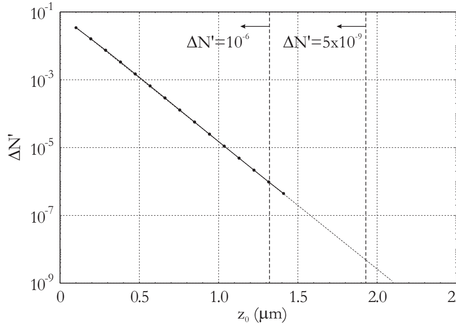

Figure 2.2: The change of the real part of N_{eff} as a function of the airgap width z_0 for a common waveguide waveguide structure with a core layer thickness of 150 nm and SiO_2 as penetrating material ($\lambda = 1550$ nm, TE polarisation)

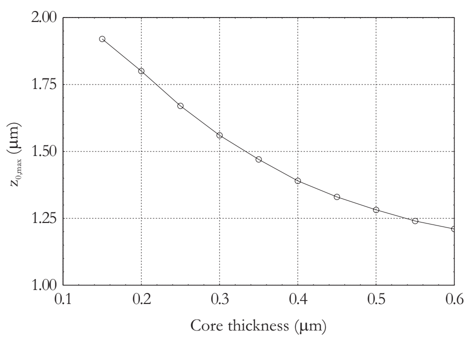

Figure 2.3: z_0-value corresponding to a $\Delta N'_{\text{eff}}$ value of 5×10^{-9} for a common waveguide waveguide structure and SiO_2 as penetrating material versus the core layer thickness ($\lambda = 1550$ nm, TE polarisation)

The measurement range of z_0 depends on the resolution of sensing principle. A bare MZI shows a resolution in N'_{eff}, $\Delta N'_{\text{eff}}$, of about 10^{-6}. The electro-optically modulated MZI enables to detect changes in the effective index down to a value of approximately 5×10^{-9}. The maximum value of the z_0 range is given by $N'_{\text{eff}}(z_{0,\text{max}}) - N'_{\text{eff}}(z_0 = \infty) = \Delta N'_{\text{eff}}$. For both systems these limits have been indicated in the Figure 2.2. Figure 2.3 shows the maximum usable z_0 -values (that is, the z_0 -value that corresponds to a $\Delta N'_{\text{eff}}$ value of 5×10^{-9}) for this type of waveguide and wavelength.

Also, we have calculated the decay length of the evanescent field and the power fraction in that layer in the state $z_0 = \infty$ for this value the wavelength and have presented them in Figure 2.4(a) as a function of the core layer thickness or as a function of N'_{eff} in Figure 2.4(b).

From comparing Figures 2.3 and 2.4 it is concluded that the range is approximately proportional to the decay length. Also, it can be concluded that, for this type waveguiding structure, the maximum value of the airgap which delivers a measurable change of N'_{eff} is limited to about 1.9 µm. So this type of systems requires a very intimate contact between the MEMS and the

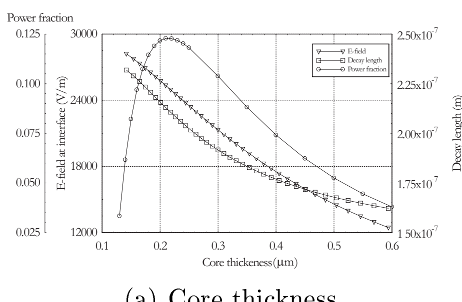

(a) Core thickness

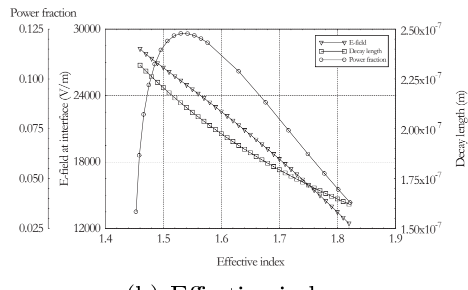

(b) Effective index

Figure 2.4: Graphs of the power fraction supported by the evanescent field in the air layer, E-field at the core-cladding interface and decay length in the air cladding for a common type waveguide ($\lambda = 1550\,\text{nm}$, TE polarisation), as a function of the core layer thickness (2.4(a)) or the effective index (2.4(b)) for $z_0 = \infty$

optical waveguide. Because many MEMS devices show a greater amplitude of the moving parts than one micrometre, this also would makes the list of MEMS devices that can be measured rather short. So for extending the measurement range we have to look for other waveguiding systems. So we have to look for systems with larger decay length and a larger fraction of power in the evanescent field. Also, TM-modes in which two electrical field components interact with the refractive index distribution may be favourable.

Considering the formula for the decay length, Equation 1.9, we can conclude that this length will increase the higher the wavelength and the lower the N_{eff} value. In the aforementioned type of waveguides the lowest value of N_{eff} was limited by the cut off condition $N_{\text{eff}} = n_{\text{substrate layer}}$.

So, at first sight, we have to choose (low loss) substrate materials with low refractive index and the lowest possible value is $n = 1$, air. This means free-standing waveguides: a core layer surrounded by two air layers, while for having the lowest N_{eff} value the core layer has to be as thin as possible and has to show a low refractive index. However, as soon as N_{eff} would be lower than the value of the refractive index of the moving object (in the case of SiO_2, $n = 1.45$) we arrive at a leaky waveguide system. Hence, to remain into a perfectly guided waveguide system, also the refractive index of the moving object has to be lowered, where the limit of SiON technology is a porous SiO_2 with a refractive index around $n = 1.2$. However, the lower the refractive index of the moving object the lower the refractive index contrast with air and the lower the effects of local replacement of air by the object. So we see a lot of contra-directional effects and a quantitative approach is

necessary for optimising the system according requirements of range and resolution of the displacement. This analysis has to extend to both type of systems, the 'common' and the free-standing configurations, and also to a variety of moving object materials, amongst others, silicon with a refractive index 3.47 at a wavelength of 1550 nm.

Quantitative analysis

Maxwell theory does not deliver analytical formulas for the quantitative description of the performance of this type of waveguide systems. So it appears straightforward to apply numerical methods implemented in the common mode solvers such as ATRguide [LDG], SimuLayer [McD] and Selene [C2V]. However, they cannot cope with leaky waveguiding systems in which one of the outer materials shows a refractive index larger than the N'_{eff} of the guided mode. If we would wish to use these mode solvers, we would have to adapt our systems by structuring or theoretically approaching the moving object also as a free-standing layer. The first option would complicate the MEMS system drastically hence being in contradiction with our wish to conserve the integrity of this system.

We have performed some preliminary calculations with these mode solvers, approximating the systems as a layer stack without lateral structures. The object was to see whether results at increasing the thickness of the moving object, implemented as free-standing layer, would converge to a certain limit. However, it appeared that not only it does not converge, while increasing the thickness of the moving object, it also crosses the numerical limits of the solvers. In addition, for the systems that does yield a solution (thicknesses $<$10 µm), the information is limited to N'_{eff} only, the leaky character of the mode, expressed by N''_{eff}, cannot be calculated.

A second option might be to apply beam propagation methods (BPM) using structures as given in Figure 2.5.

Start field is the modal field at $z_0 = \infty$. A a taper is applied in the structure of the moving object for obtaining an adiabatic transition to the real system and properties have to be derived from the propagation in the section with constant thickness of the 'MEMS' layer. However, these calculations suffer from reflections of the fields propagating in the MEMS at the edges of the calculation window. These reflected fields might couple back into the waveguide where they then can interfere with the guided beam. The reflections can be reduced or even eliminated by inserting so-called *Perfectly Matched Layers* (PMLs) at the boundaries of the calculation window that absorb, rather than reflect, the incident light. However, at the

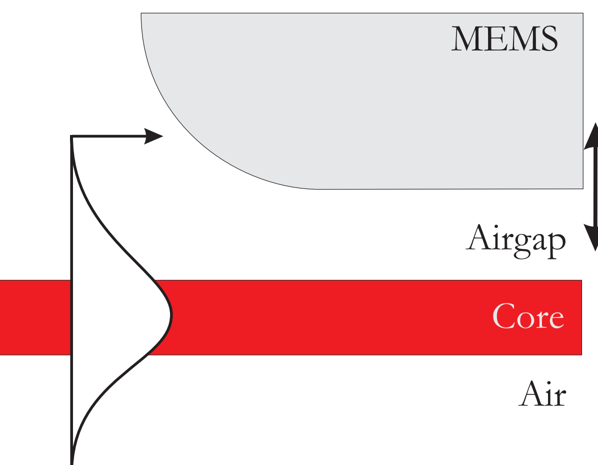

Figure 2.5: Structure as assumed for the BPM calculation.

time of the start of the project, the methods for implementing these PMLs were still under development making this approach less usable.

Finally, we applied an approximate approach based on the ray picture, using a perturbation method approach and delivering (approximate) analytical formulas from which direct conclusions can be drawn. Also here we apply the slabguide approximation. In the following section, this method is described in more detail.

Ray picture method description

We consider a layer stack, with parallel layers 1 to 4, of which layer 3 is a high index guiding layer with thickness t_3 and layer 2 is an air layer with a variable thickness t_2; the semi-infinite layer 1 represents the object which will move inside the evanescent field region of the propagating mode. It is assumed that the refractive indices of layers 2-4 are real. In the below we will derive expressions for modal index changes if the air gap thickness changes from infinity to a finite value. The derived expressions hold as well if layers 1 and 4 are replaced by a layer stack. In that case reflection coefficients like (reflection of an incoming wave in medium 2 from the interface between layers 1 and 2) have to be replaced by the coefficient corresponding to reflection from the layer stack concerned.

The transverse resonance condition for the system with infinite air gap can be derived from the function

$$\psi = 2k_0 t_3 k_x + \theta_{32} + \theta_{34} \tag{2.2}$$

and is given by:

$$\psi_0 = 0 \text{ modulo } 2\pi \tag{2.3}$$

In the above the parameters k_x, θ_{32} and θ_{34} are all functions of the effective index N; k_x is the transverse wavenumber and for example, θ_{32} is defined by $r_{32} = e^{j\theta_{32}}$. The effective index corresponding the system with infinite air gap will be denoted by N_0.

A similar function for the layer system 1 - 4 (that is, with finite air gap thickness) can be defined:

$$\xi = 2k_0 t_3 k_x + \theta_{31} + \theta_{34} \tag{2.4}$$

and the transverse resonance condition is given by

$$\xi_0 = 0 \text{ modulo } 2\pi \tag{2.5}$$

corresponding to modal index, say, $\tilde{N}_0 \equiv N_0 + \delta\tilde{N}$. We note that in the above the transverse wavenumber as well as the phase shifts may be complex quantities in case the modal indices become complex, corresponding to leaky wave solutions.

Combining Equations 2.3 and 2.5, it follows:

$$\xi = \psi + \theta_{31} - \theta_{32} \tag{2.6}$$

where we have used that the solutions corresponding to Equations 2.3 and 2.5 apply to the same mode order, implying that the terms modulo 2π cancel.

So, in the system with a finite air gap at resonance:

$$\xi(\tilde{N}_0) = \psi(\tilde{N}_0) + \theta_{31} - \theta_{32} = \psi(N_0) + \delta\psi + \theta_{31} - \theta_{32} = 0 \text{ modulo } 2\pi \tag{2.7}$$

With Equation 2.3 it now follows:

$$\delta\psi + \theta_{31} - \theta_{32} = 0 \tag{2.8}$$

Using a first-order Taylor approximation

$$\delta\psi = \frac{\partial\psi}{\partial N}\delta N = k_0 W \delta N \tag{2.9}$$

it follows, also using Equation 2.8,

$$\delta N = \frac{\jmath}{k_0 W} \ln\left(\frac{r_{31}}{r_{32}}\right)_{N_0+\delta N} \approx \delta N = \frac{\jmath}{k_0 W} \ln\left(\frac{r_{31}}{r_{32}}\right)_{N_0} \tag{2.10}$$

In Equation 2.9 we used that $\frac{\partial\psi}{\partial N} = k_0 W[\ldots]$ as has been derived in [HvSK93], where W is the length component of one zig-zag along the modal propagation direction of a beam zigzagging in the guiding layer 3. For layer system 2 - 4 Goos-Hänchen shifts have been taken into account. In Equation 2.10, the first equality is the most accurate; for its evaluation the value of δN can be improved iteratively starting from the second equality of Equation 2.10. For small perturbations (large air gaps) such an iteration is not required and one may use reflection coefficients corresponding to N_0. For small perturbations Equation 2.10 can be rewritten using the Fresnel formula:

$$r_{31} = \frac{r_{32} + r_{21}e^{-a}}{1 + r_{32}r_{21}e^{-a}} \text{ with } a \equiv 2k_0 t_2 \sqrt{N_0^2 - 1} \tag{2.11}$$

Assuming that $|r_{21}e^{-a}| \ll 1$ it follows:

$$\ln\left(\frac{r_{31}}{r_{32}}\right) = \ln\left(\frac{1 + r_{21}e^{-a}/r_{32}}{1 + r_{r2}r_{21}e^{-a}}\right) \approx r_{21}\left(\frac{1}{r_{32}} - r_{32}\right)e^{-a} = -2\jmath r_{21}\sin\theta_{32}e^{-a} \tag{2.12}$$

With Equations 2.10 and 2.12 it now follows:

$$\delta N \approx \frac{2r_{21}\sin\theta_{32}e^{-a}}{k_0 W} \tag{2.13}$$

Note that in the above in the layer stack as defined previously the reflection coefficient r_{21} describes the ratio of two evanescent fields, rather than the more common ratio of two running plane waves.

If all layers are assumed to have real indices it follows from

$$r_{21} = \frac{k_{x1} - k_{x2}}{k_{x1} + k_{x2}} \tag{2.14}$$

where k_{xi} is the component of the wave vector in medium i, perpendicular to the interface, that r_{21}, and so (from Equation 2.11), δN, is real (complex) if $N_0 > n_1$ ($N_0 < n_1$), corresponding to guided (leaky) modes for the system 1 - 4.

In case that layer 1 is replaced by a layer system, the above treatment is also applicable, but one should take care in the evaluation if this system supports a guided mode with an effective index, say, $N_1 \sim N_0$. Then, the following holds $|r_{21}| \to \infty$ for $N \to N_1$. So, Equations 2.12 and 2.13 can no longer be applied (according to the condition mentioned above Equation 2.12). But, as can be seen from Equation 2.11, r_{31} remains finite and the ratio r_{31}/r_{32} is not a rapidly varying function of N, so that the first equality of Equation 2.10 can be used to evaluate the change in modal index.

2.2 Implementation of the ray picture model

The above derived formulas have been implemented in a Matlab [Mat] program which is listed in Appendix C. For illustration, we present here the results obtained with this model for a systems consisting of a free-standing Si_3N_4 core layer with a thickness of 100 nm and a moving object consisting of silicon. Calculations have been done at $\lambda = 1550$ nm, for both TE and TM polarisation. Later on it will appear that this system is also of practical relevance. Figure 2.6(a) shows the changes of the real part of the effective index of the guided TE_0 and TM_0 mode as a function of the air gap z_0 where $\Delta N'_{\text{eff}} \equiv N'_{\text{eff}}(z_0) - N'_{\text{eff}}(\infty)$. The change in the imaginary part of the effective index is presented in Figure 2.6(b) as the attenuation (in dB/ mm) of the mode.

From these graphs and simulations obtained for other structures, we can conclude that in case a silicon object is driven into the evanescent field region:

- The TM_0 mode indeed is more sensitive to penetration of a Si object into the evanescent field region than the TE_0 mode. Starting from a $\Delta N'_{\text{eff}}$-resolution of 5×10^{-9} at 1 cm interaction length, we can state that for this structure, the N_{eff}-value of the TM_0 mode allows an upper z_0 limit of roughly 11 µm. Specific features of the MZI structure

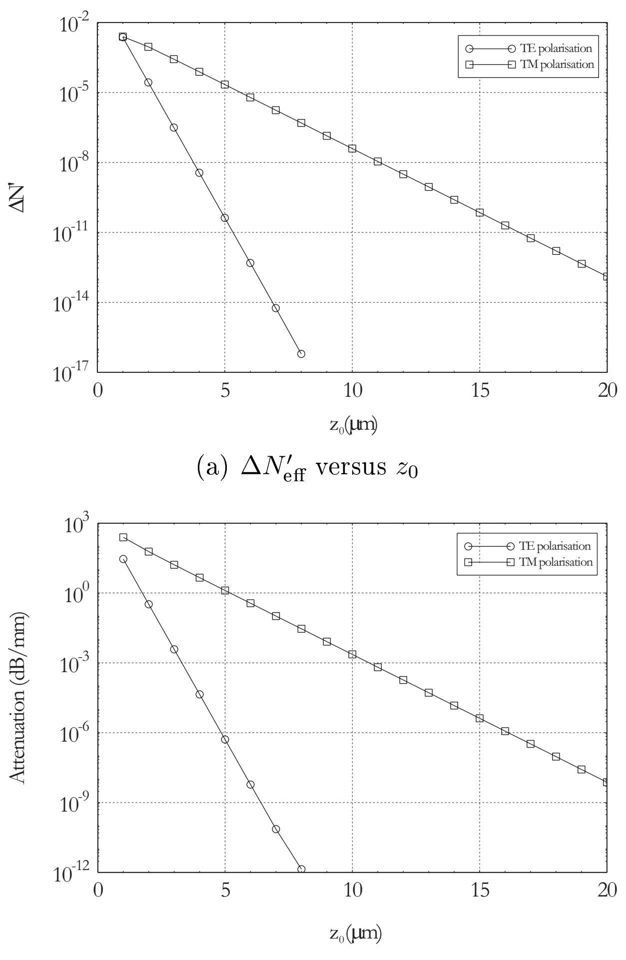

(a) $\Delta N'_{\text{eff}}$ versus z_0

(b) $\Delta N''_{\text{eff}}$ (given as attenuation in dB/ mm) versus z_0

Figure 2.6: Calculated values of the changes of the real part of the effective index (2.6(a))and calculated values the modal attenuation (2.6(b)) of the guided TE_0 and TM_0 mode as a function of the airgap z_0 for the system given in the text.

and the peripheral equipment will determine which attenuation values will be allowable and hence they will define the lower limit of z_0;

- Assuming that, at in interaction length of 1 cm, attenuations in the range 1 dB/ mm to 10^{-4} dB/ mm would be measurable, attenuation based measurements allow a z_0-range of roughly 1 µm to 10 µm;

- Usable z_0 ranges of the 'common' structure ($z_0 \simeq 1.5$ µm) and 'free-standing' structure $z_0 \simeq 11$ µm) differ an order of magnitude; the

requirements of a specific application will determine which type of structure will be most suitable.

It will be argumented in Chapter 4, that for the mirror-device the free-standing structure is most suited. The next chapter will treat the realisation of such free-standing structures.

Free-standing membrane waveguides

As shown in chapter 2, thin free-standing flat membrane waveguides in air will enable evanescent fields which extend much further than these fields in common waveguide types. The thinner the membrane, the wider the evanescent fields while for very thin membranes the fraction of the modal power propagating through the evanescent field regions will approach the value 1. However, such membranes are expected to be very vulnerable to damage due to, for example, mechanical shocks or they might be wrinkled or might break as a result of internal stresses. However, it is required that thin flat membrane waveguides can be manufactured with a high yield and they should be mechanically robust. In addition, as a boundary condition of this research, these membranes have to be produced by the SiON technology and the membrane structures and the used technology have to be as simple as possible. Also the technology has to be compatible with those generally used in the IO functions which will convert the change of modal properties into changes of the output power and with those which will afford for an efficient fiber to chip coupling. Therefore, a thorough investigation is needed to establish an optimal choice of materials, physical dimensions and process parameters.

3.1 Choice of the membrane material

From the point of view of technological simplicity it looks attractive to apply as membrane material one of the three materials which is also applied in buffer layer, core or cladding layer of the other IO circuitry and to deposit this material in all structures in the same technological step. This layer can be thinned and the other layers removed at the position of the membrane

using etching methods. So, we can distinguish the three types of basic structure for the membrane waveguide given in Figure 3.1.

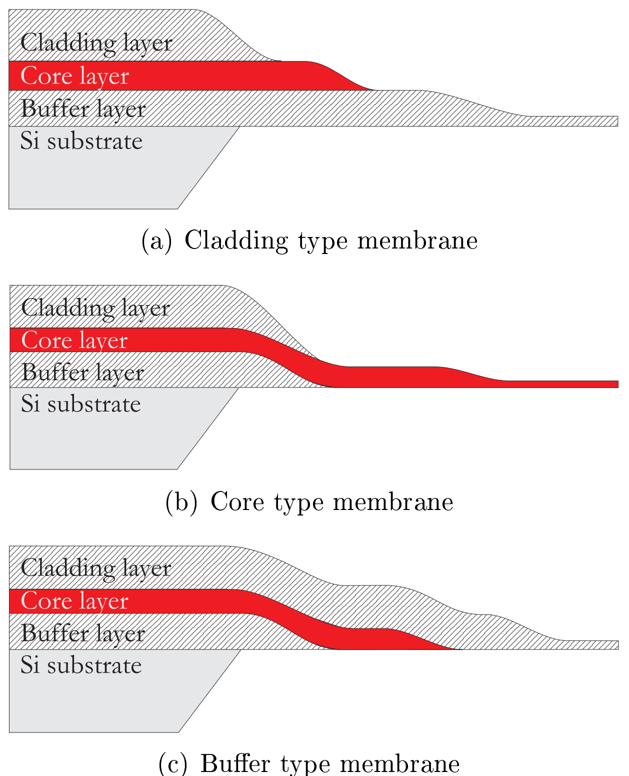

(a) Cladding type membrane

(b) Core type membrane

(c) Buffer type membrane

Figure 3.1: Three different membrane structures

In these structures, tapers have to be applied for adiabatic transitions (low modal losses) between different type of channel structures. Notice that some tapers indicated have to take care of an adiabatic transition of the mode from the original core layer to one of the other layers, while in other ones the thickness of the core layer is reduced only. Thinning layers locally, simultaneously producing these vertical tapering at the transitions to not thinned regions, can be realised by special modifications of wet etching processes [vLLH+05].

Generally, for technological reasons, the layer stacks in which the IO guides are implemented have to be as thin as possible. As one of the consequences, the buffer layer prohibiting extension of the mode into the silicon wafer has to have a low refractive index and also because of the simplicity of production, generally a SiO_2 layer produced by thermal oxidation of the Si wafer is applied. A similar reasoning holds for the protective cladding layer and therefore, in our laboratory, the PECVD produced SiON layer

with a refractive index as low as possible ($n \sim 1.47$) is generally applied as a cladding layer [WDL+99]. Of course, the core layer has to have a higher refractive index and thinnest layer stacks can be obtained by using a core material with high index, for example, LPCVD produced Si_3N_4 ($n \sim 2$). For having a monomodal layer stack as thin as possible, the thickness of the core layer should be close to the cut off thickness of the first order mode. Requirements concerning a specific performance of functions may lead to choosing a SiON core layer of lower index.

The SiO_2 obtained from thermal oxidation and the low index PECVD SiON cladding material both show large compressive stresses [BdRWA96, Pet90] and hence, it can be expected that free-standing layers of these materials will be wrinkled and indeed, preliminary experiments confirm this expectation. Hence, although from functional point of view (wide evanescent field) a low refractive index of the membrane material is preferred (see for example Figure 3.2), technological reasons force us to apply the higher index material, implying a choice for the structure given in Figure 3.1(b).

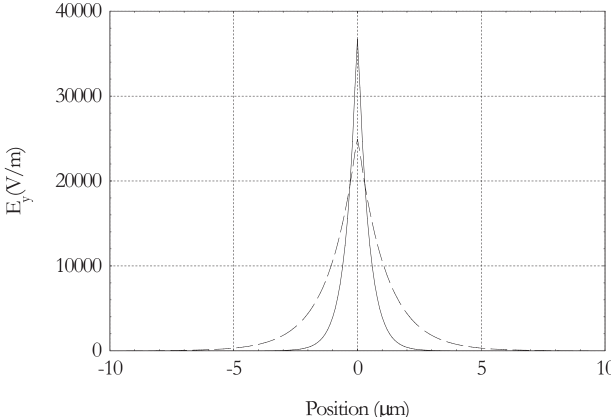

Figure 3.2: Field profiles of the fundamental mode ($\lambda = 1550\,\mathrm{nm}$) for a 100 nm thick free-standing waveguide for two different materials(SiO_2: dashed, Si_3N_4:solid)

From literature it appears that zero stress or tensile stresses in LPCVD SiON materials are obtained only in the higher refractive index region ($n > 1.5$) [Wör96, Pet90]. Appealing on the wish of thin layer stacks in the common structure and also for technological reasons, we have chosen to apply as core material LPCVD made silicon nitride, whether the stoichiometric compound which shows excellent optical properties [WLA+97] or the low-stress silicon-rich LPCVD SiN material ($n \sim 2.22$, we shall indicate this material as Si_RN), which is generally used in MEMS systems [GTV96]. It is

known that, when using 1550 nm light, a waveguide containing such a Si_RN core layer shows losses which are somewhat higher than those Si_3N_4 core layers, but which are nevertheless acceptable. For both materials, a well controlled technology has been developed in MESA+ clean room laboratory.

3.2 Preliminary experiments

Wet etching of the nitride layers

In the previous section it was given that, for the MZI circuitry for 1550 nm wavelength light, the Si_3N_4 waveguide should be as thick as possible. From technological experience it is known that Si_3N_4 can be grown using LPCVD up to a thickness of approximately 340 nm; above this thickness the layer shows cracking. Si_RN does not have this limitation.

So, when applying Si_3N_4 layers, we have chosen a maximum thickness of 300 nm, a value lower than the cut-off thickness of the 1550 nm wavelength TE_1 mode; when using a Si_RN layer this thickness would be somewhat lower. At the membrane much lower thicknesses are desired and hence the thickness has to be reduced strongly by the local etching process and possibly more than 200 nm has to be etched off. Good experience exists with etching of some nm's (for obtaining monomodal ridge type channel guides [HL99, vLLH+05]) or some tens of nm's (for obtaining efficient fibre to chip coupling [HL97]) but we had no experience with etching off some hundreds of nm's.

Buffered Hydro-Fluoric acid (BHF) is the standard etchant for glass-like (SiON) materials; it has a stable etchrate over a long period of time and the process shows a good selectivity with respect to other commonly used materials, for example, silicon (Si). Using this standard etchant, stoichiometric silicon-nitride etches at room temperature at a rate of approximately 0.6 nm/ min while the Si_RN etches at a rate of 0.2 nm/ min. As a consequence of these etch rates, etching off 200 nm will require very long etch times (over five hours). During etching the photo-lithographic resist will deteriorate due to absorption of water and eventually dissolve. To prevent this deterioration occurring at long etching times, at given times the etching has to be stopped and a rebake of the resist is needed, causing the entire thinning process to take much longer. For example, etching 200 nm of Si_RN may take several days.

Assuming that the dissolution of the SiON is process governed by the Arrhenius equation, the reaction rate would be proportional to $exp(-U/T)$ in which U is an energy and T the absolute temperature. So etch times

may be drastically shortened by etching at elevated temperatures. Hence we decided to do some preliminary experiments to determine the etch rate as a function of the temperature and to investigate whether the resist would withstand these etching conditions.

Wafers on which silicon-nitride layers with a thickness of 100 nm were deposited, were etched for 30 min in BHF solutions of different temperature. Before and after etching, the layer thicknesses were measured with an ellipsometer. Results are shown in Figure 3.3.

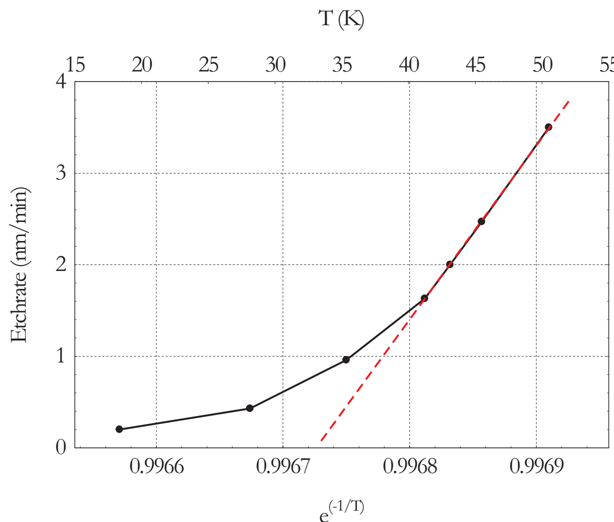

Figure 3.3: Etchrate of various silicon nitrides as a function of the temperature.

At the lower temperature range, the temperature dependance does not agree with the Arrhenius equation, but starting from 40 ℃ it agrees well. As the standard BHF solution solidifies at 12.5 ℃, we attribute disagreement with the equation to process rate limiting effects of diffusion whether of the etchants to or the reaction products from the surface due to the increased viscosity of the solution.

Surface roughness

At a temperature of 40 ℃ we have etched off larger thicknesses, starting from 300 nm thick layers. One objective was to investigate whether the resist should withstand the process, another objective was to investigate the expected increase of surface roughness at increased etching depth. This latter data on surface roughness are relevant, because the modal losses due to surface scattering increase strongly at increasing surface roughness.

This increase of roughness is usually of no great concern because for most applications the tapers in silicon-nitride have to bridge small differences in layer thickness only and then the roughness is not noticeably increased. However, etching over large depths (200 nm) is expected to create substantially more roughness. Additionally, when these tapers are applied in free-standing Si_3N_4 membranes the refractive index contrast at the membrane boundaries is high (Δn is about 1). As a result, the scattering losses will be much higher than in the common SiO_2-Si_3N_4-SiO_2 waveguides where the contrast is about 0.4 only, because the scatter losses scale with the index-difference [CG04].

Surface roughnesses have been determined from atomic force microscope (AFM) measurements. Results are presented in Table 3.1. For illustration we present some AFM pictures in Figure 3.4.

Table 3.1: Values of RMS roughness (in nm) after etching

Etched thickness (nm)	Si_RN(40 °C)	Si_3N_4 (40 °C)	Si_3N_4 (18 °C)
0	0.5	0.3	-
100	0.9	0.8	0.7
200	1.9	1.5	-

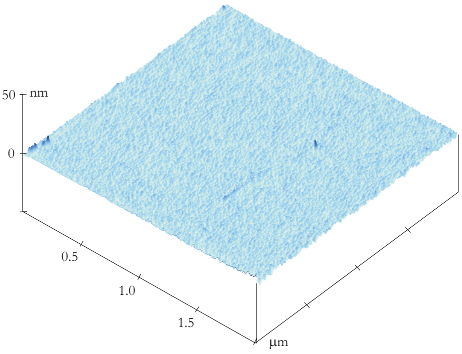

(a) Roughness of Si_3N_4, as deposited (0.3 nm RMS).

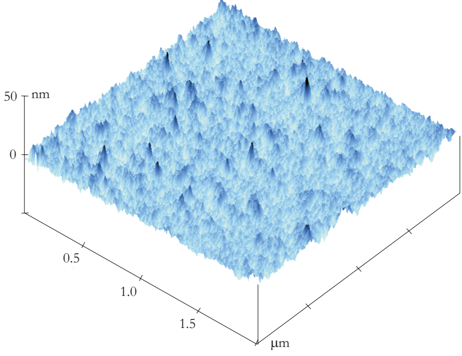

(b) Roughness plot of Si_3N_4, after etching (1.5 nm RMS).

Figure 3.4: AFM plots of a Si_3N_4 film (area $2 \times 2\,\mu m^2$), before and after etching 200 nm in hot BHF

From the results given in Table 3.1 it can be concluded that indeed an increase of etching depth results into an increase of the surface roughness. Also it can be seen that the surface roughness of the Si_RN films is larger than that of the Si_3N_4 layers, especially at the as deposited films. This would favour the application of the stoichiometric nitride material.

It is not possible to quantify effects of the surface roughness to the attenuation.

If, in practice, the effects of this surface roughness appears to be relevant, another method for making the membranes can be considered and worked out: Instead of a 300 nm thick Si_3N_4 film, a 200 nm thick film is deposited and locally (at the intended position of the membrane) completely etched off down to the silicon and next a second 100 nm thick Si_3N_4 layer is deposited on top of the first layer. However, this procedure requires an additional technological step.

Minimal thickness of the membranes

For getting some idea about the lowest thickness of Si_3N_4 or Si_RN membranes which do not crack during the removal of the silicon on top of which the layers had been applied, we decided to make a series of samples consisting of a thin SiN layer on top of a Si wafer and to etch away the Si locally from the wafer backside (see Figure 3.5).

Figure 3.5: Illustration of the SiN membrane structure

A series of free-standing SiN layers with thicknesses, ranging from 80 nm to 20 nm in 10 nm steps, has been obtained by wet etching a 300 nm thick SiN layer which was deposited directly on top of the Si wafer. Membrane areas were rectangular with a length of 10 mm and a width of whether 80 µm or 190 µm. Before and after etching, thicknesses were measured with an ellipsometer.

Results are shown in Tables 3.2 and 3.3 for Si_RN membranes and Si_3N_4 membranes respectively. Figure 3.6 shows two microscope photographs of realised membranes for both type of nitride.

From Tables 3.2 and 3.3 it can be concluded that flat free-standing membranes of Si_3N_4 and Si_RN with thicknesses down to about 40 nm can be made in this way with a 100% yield. However, membranes with thicknesses lower than 100nm appeared to be very vulnerable during further handling of the systems. So we decided to apply membranes with a thickness of 100nm. In addition, this value of the membrane thickness allows us to use the same etching process for etching down the core layer in the area

Table 3.2: Statistics for realised Si_RN membranes without a SiO_2 buffer layer

Membrane	Width 80 µm		Width 190 µm	
thickness	Yield	Wrinkling	Yield	Wrinkling
12 nm	0%	-	0%	-
32 nm	100%	yes	100%	yes
>45 nm	100%	no	100%	no

Table 3.3: Statistics for realised Si_3N_4 membranes without a SiO_2 buffer layer

Membrane	Width 80 µm		Width 190 µm	
thickness	Yield	Wrinkling	Yield	Wrinkling
24 nm	62%	no	27%	no
27 nm	87%	no	62%	no
>34 nm	100%	no	100%	no

of the fiber to chip coupling. An unexpected wrinkling of the membrane was observed (see Figure 3.6(a)) in the 32 nm thick Si_RN film. Unexpected because wrinkling is expected in films with compressive stresses only while this material should show zero stress or possibly some small tensile stress. For Si_RN membranes with a thickness over 45 nm, no more wrinkling is observed.

We attribute this wrinkling to a start-up effect of the deposition method where the initial layer that is deposited shows compressive stress, which, at layer thicknesses over 45 nm, is compensated by tensile stresses in remaining parts of the layer. As expected, the tensile nature of the stress in the Si_3N_4 layers produce perfectly smooth membranes, without any wrinkling. Furthermore, the width of the membranes does not appear to have any influence on the yield for membranes with thicknesses above 34 nm.

Considering the potential of both SiN materials for producing thin free-standing flat membranes with thicknesses down to 50 nm and the lower index of the Si_3N_4 (meaning wider evanescent field) and the lower optical losses (meaning higher resolutions in MZI measurements) we decide to apply the stoichiometric Si_3N_4 as core material and hence as membrane material.

Alternative method for removing locally the substrate layer

We have considered the possibility instead of etching away the thermal oxide layer locally at the intended site of the membrane before deposition of the

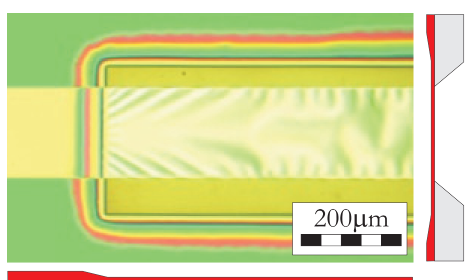

(a) Si_RN membrane, thickness: 32 nm

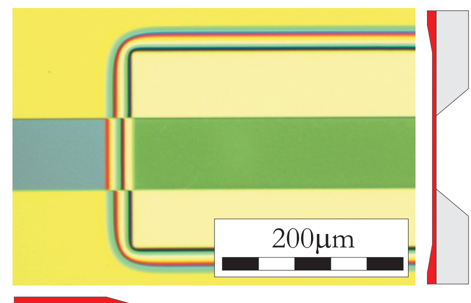

(b) Si_3N_4 membrane, thickness: 24 nm

Figure 3.6: Photographs of realised silicon nitride membranes, without an silicon-oxide buffer layer

nitride layer to leave the SiO_2 layer intact and to remove it afterwards by etching from the back side. This means that, after having removed locally all Silicon by wet etching using a KOH solution, we have continued the etching process, but now using a BHF solution for removing locally the SiO_2 layer. However, it appeared that after removal of the silicon the membrane was buckled (we attribute that to the large compressive tresses in the SiO_2) and that during etching away the SiO_2 the membrane cracked.

The taper fabrication process

Adiabatic vertically tapering is a common technique, applied, for example, to create efficient fibre-to-chip(FC) couplings [HL97]. However, when applied in FC's the etch-depth is usually limited to several 10's of nm. In case of the membrane however, the taper has to connect a 300 nm thick Si_3N_4 layer to a 100 nm thick one; hence the etch-depth is significantly larger, approximately 200 nm.

The usual way of making vertical tapers is by deliberately treating the photo-lithographic resist layer in such a way that the adhesion to the underlying layers is weak [Kos00]. This allows the etchant to move underneath the resist layer and the etch front moves in both the vertical and lateral direction. Because of the large difference between the lateral under-etch rate and the vertical etch rate a vertical taper is obtained. In addition, as-grown Si_3N_4 layers have a natural SiO_2 layer at its surface. As the etchrate of SiO_2 is approximately 100 times greater than the etchrate of Si_3N_4 the SiO_2 acts as a sacrificial layer causing a further increase of the lateral under-etch.

Etching the tapers in Si_3N_4 is done in one etching step. Because of previous experience, the tapers in SiO_2 are made by using a double masking

and etching procedure: in the first step the SiO_2 is etched to half of the desired depth, in the second step the remainder of the depth is etched where the mask-edge of the second step is shifted in the longitudinal direction. Taper angles obtained were 3 and 0.3 degrees for the SiO_2 and SiN layers respectively.

3.3 The final tapered membrane section

Structure

Based on all aforementioned experimental results and considerations we decided to realise various systems of the type given in Figure 3.1(b), mutually differing in the thickness of the membrane layer (in the 80 nm- 20 nm range) only. Membrane layers will consist whether of Si_3N_4 or of Si_RN. The objective is to verify whether such systems can be produced indeed and to determine its main relevant characteristics.

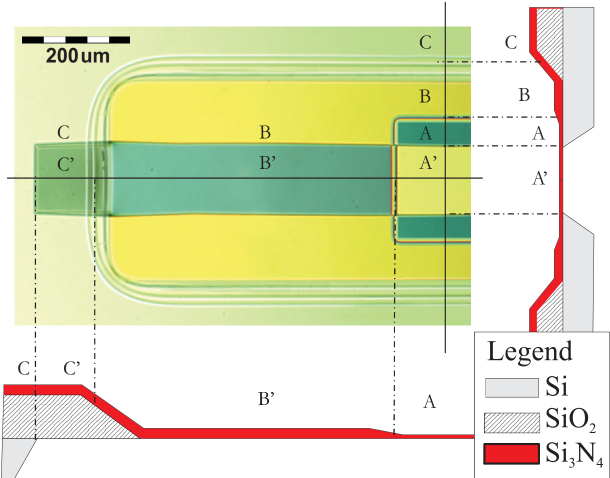

Figure 3.7: Photograph of a realised Si_3N_4 membrane with longitudinal and transverse cross-sections (bottom and right, respectively)

In the structure there is a small section consisting of a free-standing SiO_2-SiN double layer so it may happen that this will act as the source of some buckling or wrinkling or will cause cracking of the membrane even.

Technology

The membrane waveguides are fabricated mainly using the well controlled standard SiON technology, which has been developed during the last decade by the IOMS group. The wet etching processes for producing the tapered membranes in an acceptable time are the modified ones, which have been as described in former sections. The starting-point is a $\langle 100 \rangle$ oriented, silicon wafer. First, the crystal-orientation is determined and indicated with alignment marks. Next, a 3 µm thick SiO_2 buffer layer is grown using thermal oxidation. This layer is then wet-chemically etched in the membrane section using BHF. Next, a 300 nm thick nitride (either Si_3N_4 or Si_RN) layer is deposited using an LPCVD process. In the region of the membrane section, this layer is tapered down in two steps to the desired thickness using a heated (40 °C) BHF solution. Next, the membrane section is defined at the backside of the wafer by locally etching off over there the SiO_2-SiN layer stack using a combination of Reactive Ion Etching (RIE) (a dry-etch process) and wet etching by BHF solutions. Finally, the silicon substrate underneath the membranes is etched away in a KOH solution to make the membranes free-standing.

Characterisation

Microscopic observation

The realised membrane structures are observed by a microscope. Data concerning yield and flatness of the structures are presented in Tables 3.4 and 3.5 while Figure 3.8 shows microscope photographs of some realised membranes of both types of nitride.

Table 3.4: Statistics of realised Si_RN membranes with a SiO_2 buffer layer

Membrane thickness	Width 80 µm		Width 190 µm	
	Yield	Wrinkling	Yield	Wrinkling
23 nm	100%	yes	100%	yes
32 nm	100%	yes	100%	yes
>45 nm	100%	no	100%	no

From Tables 3.4 and 3.5 we conclude that also in the system in which the SiO_2 buffer layer is included membranes with thickness down to 30 nm can be produced with a 100% yield. The thinner Si_RN membranes are wrinkled while all Si_3N_4 membranes are flat. In both systems some buckling can be observed. at the small SiO_2-SiN double-layer section being less expressed in the Si_3N_4 system. The latter can be explained by the higher tensile stress

Table 3.5: Statistics of realised Si_3N_4 membranes with a SiO_2 buffer layer

Membrane thickness	Width 80 µm		Width 190 µm	
	Yield	Wrinkling	Yield	Wrinkling
20 nm	100%	no	0%	-
26 nm	100%	no	75%	no
>31 nm	100%	no	100%	no

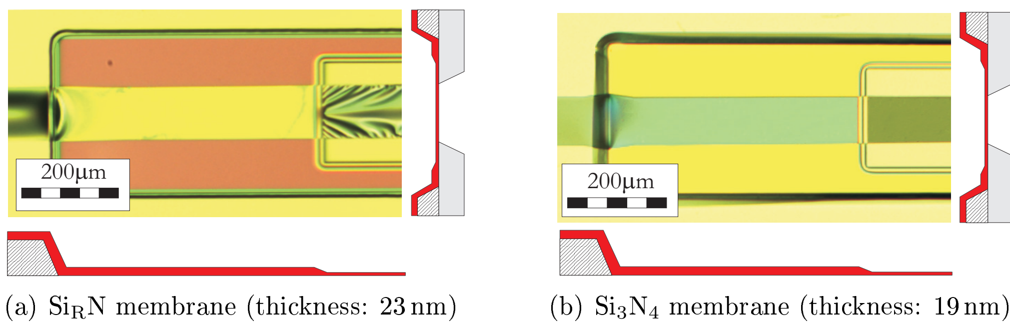

(a) Si_RN membrane (thickness: 23 nm) (b) Si_3N_4 membrane (thickness: 19 nm)

Figure 3.8: Photographs of realised silicon nitride membranes, with an silicon-oxide buffer layer

of the Si_3N_4 film which compensates the effects of the compressive stress in the double layer section stress partly. The microscope photos shown in Figure 3.9 (close-ups of Figure 3.8) indicate that the magnitude of this buckling depends on the thickness of the SiO_2 layer and the type of silicon nitride.

Comparison of Figure 3.9(a) and 3.9(b) indicates the less buckling when the SiO_2 layer is the thinner pointing to an increased compensation of the effects of the compressive stress by the tensile stress of the Si_RN.

Figure 3.9(c) shows a significantly lower buckling in the case of a double-layer stack consisting of a 3200 nm thick SiO_2 layer and a 300 nm thick Si_3N_4 layer. The highly tensile Si_3N_4 layer can better reduce the effect of the compressive stress of an even thicker SiO_2 layer.

Comparison of Tables 3.2 and 3.3 with Tables 3.4 and 3.5 indicates that presence of the SiO_2 buffer layer does not significantly alter the yield and flatness of the membranes.

Figure 3.10 shows a system in which a Si_RN layer is deposited directly on the silicon wafer and where, as a result of a technological error, locally over a large distance the Si underneath the thicker Si_RN layer has been etched away. As a result the tensile stress of the (now free-standing) thicker part of the membrane will be dominant and some wrinkling in the thinner part will be partly compensated. Starting from the beginning of the defect (indicated

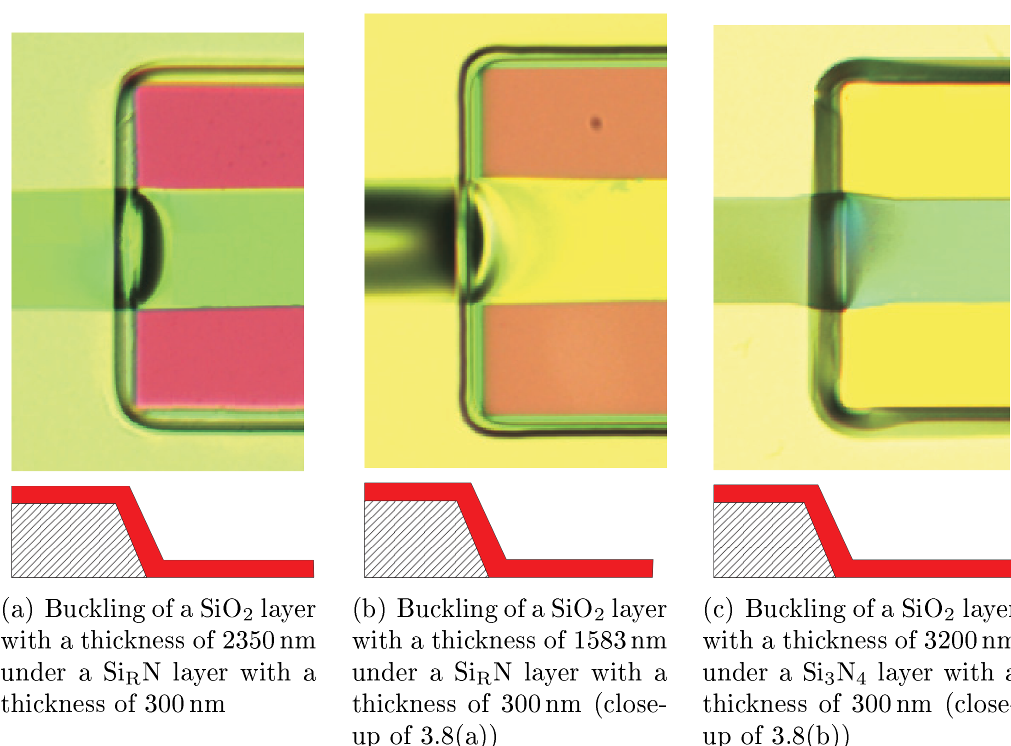

(a) Buckling of a SiO_2 layer with a thickness of 2350 nm under a Si_RN layer with a thickness of 300 nm

(b) Buckling of a SiO_2 layer with a thickness of 1583 nm under a Si_RN layer with a thickness of 300 nm (close-up of 3.8(a))

(c) Buckling of a SiO_2 layer with a thickness of 3200 nm under a Si_3N_4 layer with a thickness of 300 nm (close-up of 3.8(b))

Figure 3.9: Photographs of deformations in double-layer sections of free-standing SiO_2/SiN

by point 'P' in the figure), the wrinkling diminishes, quite rapidly in the along the x-direction and more gradually in the y-direction. This indicates that the tensile stress in the thicker membrane is smoothing the wrinkles in the thin membrane.

Functional losses of the membrane structures

Insertion loss measurements were carried out on straight ridge-type channel waveguides. For determining the losses related to the membrane implementation, insertion losses of the membrane containing channels have been compared with those of similar channels but now without a membrane.

After thermal oxidation of the wafer (thickness of the SiO_2 layer 3.2 µm), a 300 nm thick Si_3N_4 layer has been deposited by LPCVD. In this layer monomodal (at 1550 nm wavelength) waveguiding channels with a channel width of 4 µm and a ridge height of 6 nm have been implemented using standard photolithography and wet-chemical etching processes. A SiON cladding (n = 1.47, thickness 3 µm) has been applied by PECVD. Using

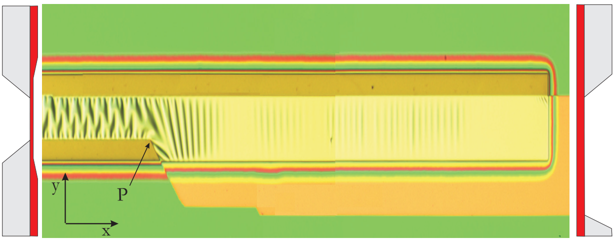

Figure 3.10: Photograph showing an etch defect that creates both 'thin' nitride membranes (thickness 32 nm), showing compressive stress, and 'thick' nitride membranes (thickness 300 nm), showing tensile stress. The tensile stressed part of the layer compensates in one direction the wrinkling effects of the compressively stressed part of the layer.

photolithography and wet etching processes a membrane structure of the type given in Figure 3.7 has been implemented. The free-standing 100 nm thick Si_3N_4 membrane is 5 mm long and 3 mm wide. Light has been coupled into and out of the channels by fiber to chip coupling. Membrane induced losses are given in Table 3.6.

The data in the table refer to the average over eight channels. The fairly high values of the standard deviation are mainly attributed to differences in fiber to chip coupling efficiencies of the individual channels. The table shows that the membrane induced losses are much smaller for the TE mode (2.6 dB) than for the TM mode (7.8 dB). We mainly attribute this to the surface roughness of the thinned Si_3N_4 waveguiding section, which generally has much larger effects on TM modes than on TE modes.

Table 3.6: Insertion loss (and standard deviation σ) of chips containing 3 cm long straight waveguides of various type, $\lambda = 1550$ nm.

Polarisation	Membrane induced loss (dB)	σ (dB)
TE	2.6	0.3
TM	7.8	1.1

Despite the higher membrane induced losses for TM polarisation, we have decided to use the single-step deposition of the Si_3N_4 as this allows for easy integration in the fabrication process of the FC-coupling section (see Chapter 4 and Appendix B).

3.4 Summary

It has been shown that free-standing nitride membranes can be made with 100% yield at thicknesses down to 35 nm. It has been concluded that it has to be preferred that the membrane consists of the same material as the core layer of the adjacent 'common' IO structures on the chip. For this, silicon nitrides are preferred. Stoichiometric silicon nitride, Si_3N_4 membranes show to be superior over silicon-rich silicon nitride membranes for the following reasons:

- The Si_3N_4 membrane itself is always flat, due to its tensile stress, while sometimes the Si_RN membrane shows some wrinkles.
- The tensile stress of the Si_3N_4 membrane reduces the buckling caused by the compressive stress in the small section of a free-standing SiO_2-SiN double layer.
- The etched down Si_3N_4 layer shows less surface roughness and hence less optical scatter losses of the propagating mode
- The refractive index of the Si_3N_4 layer is lower enabling to measure displacements over larger ranges.

To enable damage free handling of the membrane systems a membrane thickness of 100 nm has been chosen. If however it should appear that the detection range would be too small, systems with a thickness down to about 50 nm can be taken in consideration. A technology for making the structures is given and has been successfully applied. To reduce the effect of roughness induced loss, one may fabricate the membrane in two Si_3N_4 deposition steps, ensuring a membrane surface of lower surface roughness.

The micro-mirror demonstrator

4.1 Introduction

Two out of the three MEMS devices, on which the demonstrators are based, the micro-mirror and the vibrating membrane, show deflections that exceed the usable evanescent field range of a common waveguiding structure. Therefore, the demonstrators containing these MEMS devices have to utilise the free-standing membrane waveguiding structures. In both demonstrators deflections will be read out by MZI based optical circuits. However, the level of complexity will be different for each system, as will be discussed later on.

As for the micro-mirror demonstrator, opposite to both other demonstrators, at the start of the project most properties of the MEMS device were well defined and clear requirements had been formulated, it was decided to initially focus on this demonstrator; experience gained here should later be applied in the development of the second demonstrator, the piezoelectrically actuated vibrating membrane.

This chapter deals with the *rotatable micro-mirror* demonstrator: the mirror system is described and its characteristics are listed as well as the requirements to the readout of the movements. Next, the consequences of the requirements are analysed, taking into account the required geometrical and technological compatibility of the IO and the MEMS systems. Based on simulations of the mechano-optical interaction and considerations of technological feasibility, the final design of the demonstrator system will be presented and discussed. The detailed technological process for realising the demonstrator (starting from a given MEMS device as is realised by TUC) will be presented. Microscopic pictures of the realised demonstrator and some data on the optical effects of the rotation of the mirror will be presented and discussed.

Relevant properties of the mirror system

The Technical University of Chemnitz (TUC) has designed, produced and characterised a large variety of rotatable micro-mirrors, mutually differing in the geometry of the mirror plate and the mirror hinges. The available types of mirrors are listed in Table 4.1. A schematic drawing and a microscopic picture of such a device are given in Figure 4.1.

Table 4.1: TUC mirror properties

Mirror type (width × length in mm)	Resonance frequency (Hz)
1.2 × 1.2	9000
1.5 × 1.5	4600
2 × 2	1950
3 × 4	820
4 × 4	505

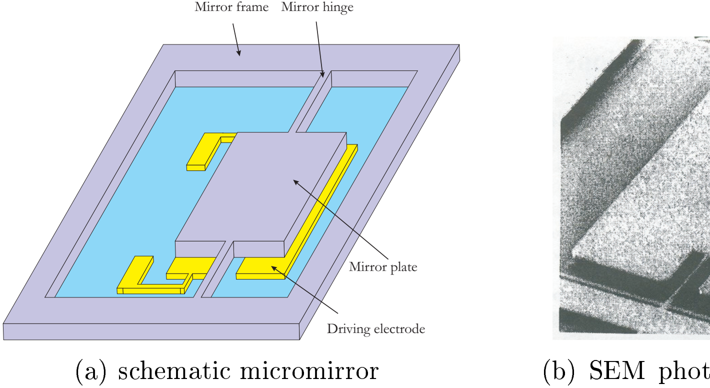

(a) schematic micromirror

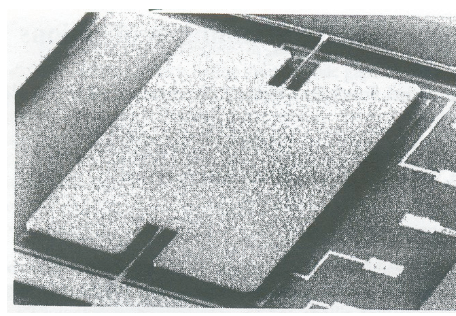

(b) SEM photograph of realised micro-mirror

Figure 4.1: schematic drawing and a microscopic picture or micro-mirror

Most of their systems are realised starting from a bare silicon wafer. Metal electrodes (a choice out of gold or aluminum, chromium or platinum) are applied, not only on the front side of the mirror plate, but also on the back side in order to compensate stresses and so to maintain the flatness of the plate. The pair of metal electrodes is activated in anti-phase resulting in a push-pull character of the electrostatic forces which drive the rotation of the mirror. During functioning of the mirror, a light beam is send to the upper side of the mirror and the direction of the reflected light can be controlled by varying the rotation angle of the mirror.

After discussion with LOPMD and TUC, it was decided that both LOPMD and MESA+ should focus on an identical mirror system in order

to enable an efficient comparison of the different readout methods which will be implemented by these groups. A schematic top view of this system is given in Figure 1.7(a). Arguments for this choice will be given in section 4.2.

The structure to be driven into the evanescent field is a 30 µm thick silicon plate coated on both sides with a metal electrode. In the standard TUC mirror, the metal being either aluminum or gold. Metal thickness, generally applied by TUC, is in the range 10 nm- 200 nm. Rotation angle as a function of the applied voltage, both for static actuation and for dynamic actuation, is given in Figure 4.2.

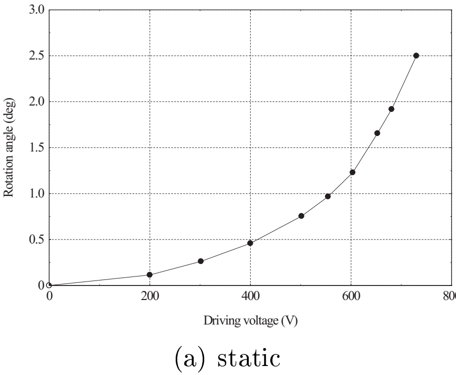

(a) static

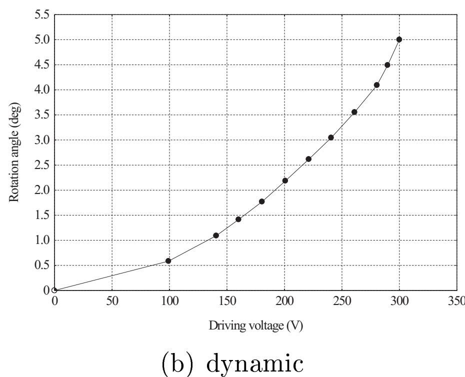

(b) dynamic

Figure 4.2: Characteristics of the $4 \times 4\,\text{mm}^2$ micro-mirror, static and dynamic (at resonance) drive.

No data were available on a potential transverse or lateral movement of the rotation axis or on any deformation of the mirror during rotation. In our analysis we have assumed perfect behaviour during rotation: a rigid plate and a constant position of the mirror rotation axis.

Requirements to the readout of the mirror system

For applications intended by TUC, the IO readout-system for the mirror-demonstrator must have the following capabilities:

- no effects of the readout-system on the properties and performance of the MEMS system;
- ability to read out resonance frequencies with an accuracy of 5 Hz;
- ability to read out rotation angles (and hence displacements) with an accuracy in the range 1% - 0.1%.

4.2 Qualitative Analysis

In principle, there are two options for the main structure of the demonstrator: applying the IOMS wafer whether on the front or at the back side of the mirror plate. The first option has the drawback that, if using the front plane as reflector, the IO system will block (part of) the incident beam causing optical losses and spurious reflections. An alternative is to use the back plane of the mirror as reflector but this has, as might be expected, the drawback that the roughness of this plane may be somewhat higher than that of the front plane, causing more diffuse reflection. The relevance of this drawback will depend on the one hand on the magnitude of this roughness and at the other hand on the specific application aimed at. The second option requires large local variations of the thickness of the optical wafer (more technological steps required) and in addition, these variations will prevent an accurate definition of the channel waveguides. We have decided to use the first option utilising the back side of the mirror as a reflector. In fact, the envisaged MOEMS system can be considered as being formed from the original MEMS structure by substituting the IO wafer for the distance wafer and by interchanging the electrode plate and the cover plate.

At first sight, this option might appear to be very impractical, because now the optical wafer will block the electrode action. However, this blocking can be prevented by applying locally holes in the optical wafer and, as will be shown later (Section 4.3), these holes are also necessary to facilitate the required free rotation of the mirror. So we arrive at a basic structure as given in Figure 4.3.

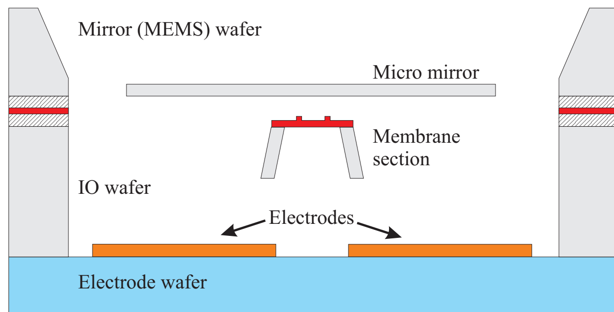

Figure 4.3: Basic structure of the optical wafer for the mirror demonstrator

A second problem connected to this *front-to-front* structure arises from the need to realise the necessary connections of the IO circuit to the outside world: optical ones (the fiber to chip couplings) and electrical ones (for connecting the electrodes of the modulator), which normally are applied

on the front side of the IO wafer. An option is to shift these coupling functions to the back side of the optical wafer: optical coupling by gratings and electrical connections by implementing so-called Electrical Through Wafer Interconnects (ETWI) [CCP+02]. This all will require a much more complicated technology. However, in the demonstrator devices, room for these connections at the front side can be created by deliberately breaking out some mirrors, then however limiting the read out to a column of mirrors (see Figure 4.4). We decided to adopt this last option especially because the $4 \times 4\,\text{mm}^2$ mirror system, offering $7.6 \times 6.8\,\text{mm}^2$ holes, is expected to facilitate the application of the fibers and electrical connections and, in fact, this was one of the reasons to opt for this specific mirror system.

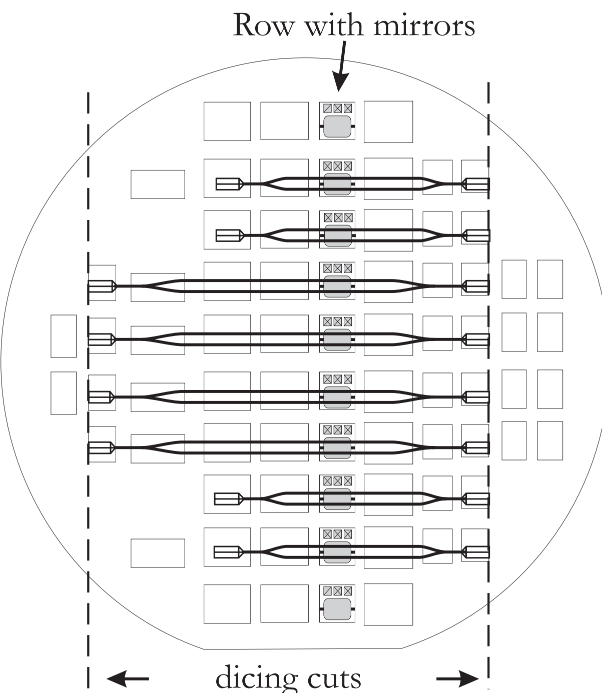

Figure 4.4: Illustration of measuring a column of mirrors and the removal of other mirrors to create openings for fibers and electrical connections

Aside of this geometrical compatibility also a technological compatibility is required: both wafers have to be bonded together. Fortunately, the outer layer of the MEMS wafer offered for the binding consists of silicon and the outer layer of the IO structure of SiO_2. Principally, bonding may be possible; the bonding problem will be considered in more detail in Section 4.7.

The question arises whether in this configuration the performance of the mirror would not be influenced by the presence of the IO circuitry. This cannot be guaranteed in advance. It is not excluded that by bonding these wafers, a stress distribution in the MEMS wafer will be created or an existing one will be varied, which will influence the mechanical performance. In dynamic measurements squeezing may occur, and its effects will depend on the rotation frequency and amplitude and, in addition, on the distance between mirror and waveguiding layer and on the lateral dimension of the free-standing waveguiding structure. For reducing the squeezing, the MZI branches supporting bridge should be narrow and the distance between mirror and waveguides should be large. Also, the presence of the waveguiding structure may influence the mirror driving electrical field generated by applying a voltage between the metal electrodes and the mirror. The latter problem will be treated in section 4.4.

In principle, the free-standing channel structure containing both MZI branches can be part of a laterally completely free-standing membrane or of a membrane that, at its lateral sides, is supported by leaving some silicon there; a principle cross section of the second structure is given in Figure 4.5.

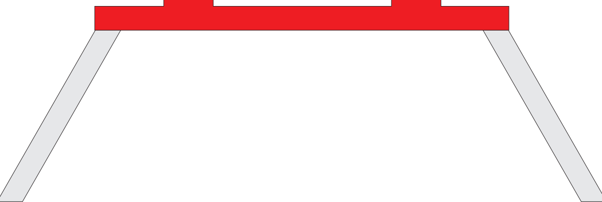

Figure 4.5: Waveguiding membrane supported by silicon at its lateral sides.

Because the first structure was considered to be too vulnerable we decided to concentrate on the second one.

Two options can be formulated for the MZI readout of the rotation. In the first one, both the centre line of the MZI and the rotation axis of the mirror are in the same plane perpendicular to the wafers enabling that the modes propagating through both branches interact with the mirror in a *push-pull* mode (see Figure 4.6(a)). In the second option only one of the branches of the MZI interacts with the mirror (see Figure 4.6(b)).

The second option requires that both branches are about 2 mm separated from each other to be compared with the required 100 µm distance in the first option. As a consequence of this larger distance, temperature differences between both branches would be larger too which would result into a degradation of the resolution [HL99] while also a longer MZI structure would be required. However, as an advantage, the free-standing area

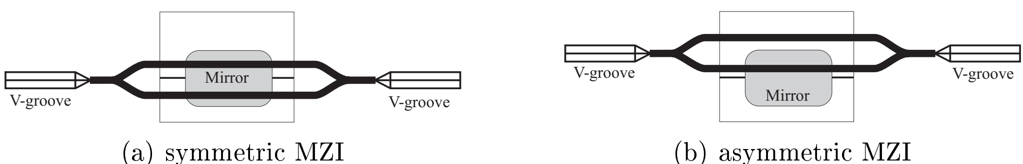

(a) symmetric MZI (b) asymmetric MZI

Figure 4.6: Top-view of two MZI-mirror configurations with different positions of the branches with respect to the mirror

can be narrower leading to, for example, less squeezing. We have preferred the first option.

Originally, these demonstrators were intended to be provided with zinc-oxide (ZnO) electro-optical modulator sections to apply a *serrodyne* detection scheme (as outlined in Chapter1). However, characterisation and optimisation of the ZnO layers for operation at a wavelength of 1550 nm was introduced in the total project later on only as a special task to be executed by LioniX and the results were expected to be not yet available when needed for a good progress of the mirror demonstrator sub-project. Because developing this demonstrator could not wait on these results it was decided to apply here a MZI without modulators. The PZT membrane demonstrator only should be fitted with ZnO modulators.

4.3 Quantitative analysis

For maximisation of the desired mechano-optical effects and minimisation of the disturbing ones, both the geometry of the mirror-waveguide region and the nature of the material driven into the evanescent field are relevant.

MEMS material influence

In the mirror demonstrator, the object which is driven into the evanescent field region, consists of a silicon plate coated with a metal layer. At TUC, the following metals are available as coating for the micro-mirrors: aluminium (Al), gold (Au), chromium (Cr) and platinum (Pt). Aiming at maximal mechano-optical effects we have to determine the best values of the offered variables, the electrode material and the electrode thickness. For this we need to know the values of the real and imaginary components of the refractive index values of all these materials at the applied wavelength of 1550 nm. These are listed in Table 4.2.

Table 4.2: Refractive indices of used metals

Material	n	k
Al	1.44	15.955
Au	0.18	10.21
Cr	4.18	4.96
Pt	5.31	7.04

As the ray picture model can cope with a layer stack penetrating the evanescent field, we apply Equation 2.13 for calculating the mechano-optical effects. In the calculations we have (anticipating here on results presented later on) assumed that the ridge type channel waveguides forming the branches of the MZI are implemented into a 100 nm thick free-standing silicon nitride membrane ($n = 2.00$) and we have defined the distance between the waveguide and the mirror plate to be 4 µm. Figure 4.7 shows the calculated changes of the real and imaginary part of the effective index of the guided mode as a function of the thickness of the metal layer coated on the (assumed infinitely thick silicon plate. The change of the real part is presented as $\Delta N'_{\mathrm{eff}}$, the reference state ($\Delta N'_{\mathrm{eff}}= 0$) being the one in which the mirror plate is absent, while the imaginary part has been transformed already in the attenuation at 4 mm interaction length. Similar curves are obtained by taking other values of the plate to waveguide distance.

Generally, one wishes to maximise the effect aimed at (here the $\Delta N'_{\mathrm{eff}}$-effect) and to minimise disturbing effects (here the attenuation). Because the desired effect is proportional to the interaction length we have chosen to work with one of the largest mirrors out of the series offered by TUC, the $4 \times 4\,\mathrm{mm}^2$ mirror. From Figure 3.6 it appears that in the case of Au and Al the largest the $\Delta N'_{\mathrm{eff}}$-effect (in the thickness range 10 nm- 20 nm)is accompanied by a relatively strong attenuation. In the figure it can also be seen that for metal thicknesses over 0.10 µm- 0.15 µm all optical effects are independent on the actual metal layer thickness, which also appears to hold for other plate-waveguide distances. In this thickness range the attenuation is one order of magnitude and the $\Delta N'_{\mathrm{eff}}$ values less than 20% lower than the maximum ones. Also it is seen that for all plate to mirror distances application of gold results into the highest $\Delta N'_{\mathrm{eff}}$-value and the smallest attenuation. Considering this all, we decided to apply gold electrodes thicker than 0.1 µm. After consultation of TUC the final electrode thickness has been defined as 200 nm.

The local maxima in the curves shown in Figure 4.7 are due to the excitation of surface plasmons propagating along the metal-silicon interface. Calculated values for $N'_{\mathrm{eff}}$and $N''_{\mathrm{eff}}$for these plasmons in a gold (Au) layer

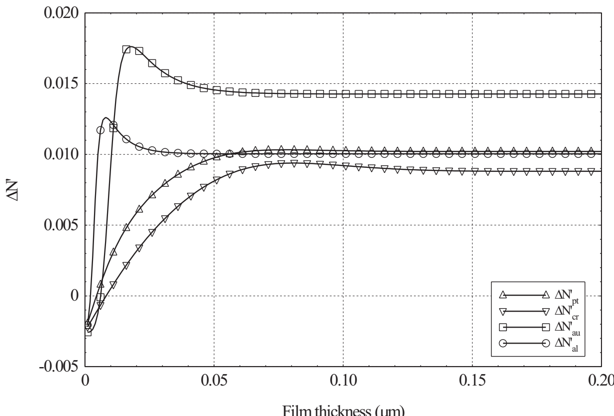

(a) Effect of the thickness of a metal coating on a Si MEMS part on $\Delta N'_{\mathrm{eff}}$

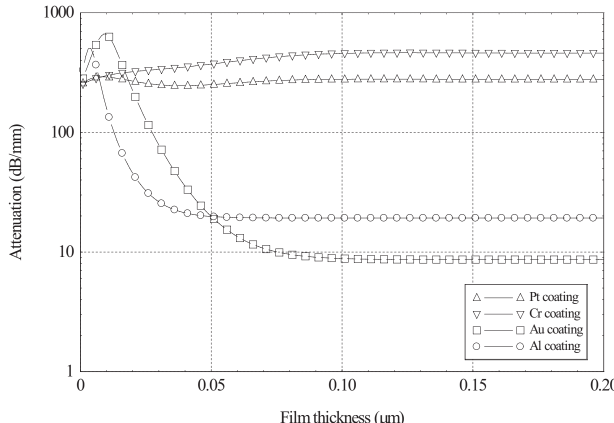

(b) Effect of the thickness of a metal coating on a Si MEMS part on the attenuation

Figure 4.7: Effect of metal coating on modal properties

are shown in Figure 4.8 and it is clear that qualitatively the values in this figure are in good agreement with those presented in Figure 4.7.

Geometry influence

Considering the geometry of the mechano-optical structure, an indispensable requirement is that the mirror can freely rotate up to the maximum rotation angle, θ_{max}. In this specific mirror system we have defined θ_{max} as the maximum angle in the static θ versus V_{act} curve (see figure 4.9), that is, 2.5°, considering that the frequency dependence of the rotation can also be

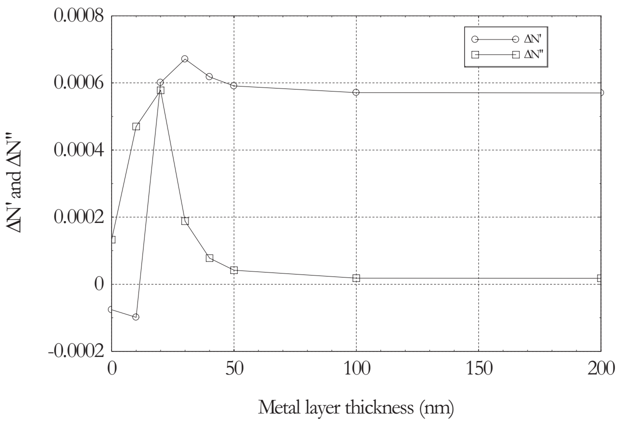

Figure 4.8: Calculated $\Delta N'_{\text{eff}}$and $\Delta N''_{\text{eff}}$values for a surface plasmon in a gold layer on a Si substrate

determined at V_{act} -values, at which the rotation angle will not exceed this value.

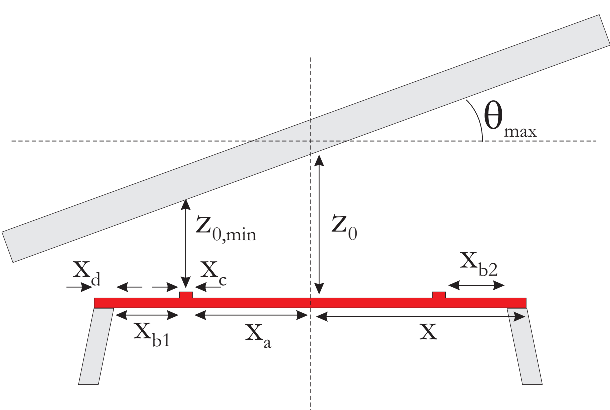

Figure 4.9: Relevant dimensions of the IO-mirror system in the sensing area

Referring to Figure 4.9, it is this θ_{max} which defines the minimum value of the ratio z_0/x. It is clear that the smaller the half-width x of the optical bridge, the smaller z_0-value can be chosen and the larger the sensitivity $\partial N'/\partial z_0$. However, there is a minimum of the value of x as a consequence of the following requirements:

- x_a has to be that large that the modes between both channels do not effectively see each other (modal overlap negligible);

- x_c has to be as small as possible, however under condition that the channel is monomodal and that this width has to be realisable with the facilities in our clean room laboratory (that is, minimal width about 4 µm);
- x_b has to be that large that the modal properties are effectively not influenced by the presence of either air or a membrane supporting structure at $x > (x_a + x_b + x_c)$ in that way eliminating any influence of technology related differences between x_{b1} and x_{b2} on the modal propagation.

All three requirements point to maximum modal confinement in lateral direction implying the minimal channel width x_c and the maximum channel ridge height h_r which corresponds to a monomodal channel. Leaving some room for technological inaccuracies best values are $x_c = 4$ µm and $h_r = 6$ nm for the wavelength 1550 nm. For these channels the minimum values of x_a and x_b have been calculated to be 28 µm and 25 µm respectively. The yet missing definition of x_d depends on other factors and will be discussed later on in Section 4.5 on page 58.

However, the minimal bridge width and the maximal rotation angle $\theta_{\max}$ are not the only parameters which determine the minimal value of z_0. There is a further limitation which originates from the requirement of a proper functioning of the MZI. Because the modal attenuation increases, the smaller the distance z between moving object and the surface of the waveguide, a minimum has to be set to this distance: at high attenuation the powers exiting both MZI-branches will be very different and as a result the modulation depth of the MZI will be small, just as the amplitude of the resulting output signal. As a final consequence the signal to noise ratio might be reduced to unacceptably low values.

Although the maximum allowable attenuation depends on many factors such as the incident power, the insertion losses of the MZI at $z_0 = \infty$ and the properties of the opto-electronic system, we have chosen that the attenuation caused by the moving object has to be smaller than 8 dB, leaving some freedom to the value of the incident optical power. Note that in the asymmetric MZI (Figure 4.6(b)), the difference in output power of both branches can be reduced by adapting the splitting ratio of the first Y-junction.

To determine the corresponding minimal value of z_0, $z_{0,\min}$, we have calculated the z_0-dependence of the attenuation, taking the Si_3N_4 membrane thickness to be 100 nm and the gold electrode thickness 200 nm (see Figure 4.10). The aforementioned limitation of the attenuation appears to imply that for this mirror system, that z_0 should be larger than 3.2 µm.

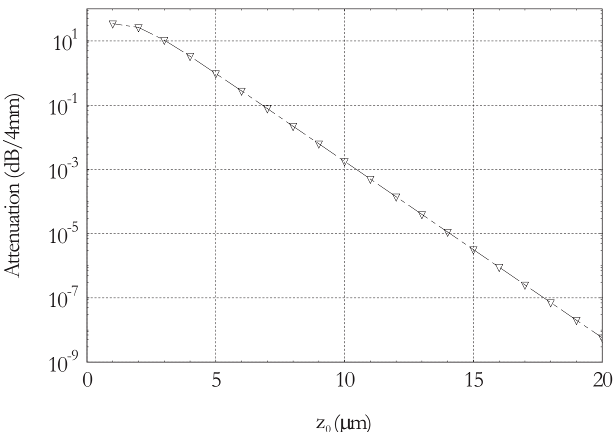

Figure 4.10: Attenuation versus airgap z_0 at 1550 nm wavelength when the fundamental TM mode propagates through a 100 nm thick free-standing slab waveguide for a 4 mm long gold coated silicon MEMS part penetrating the evanescent field region

The z_0 value is not only limited at the lower side, but also on the higher one. The latter is the result of the required accuracy of the distance determination, 1% - 0.1% of the full z_0-range. This requirement can be worked out to the (approximate) relation:

$$\eta(z_0 - z_{0,\text{min}}) = \delta z_{\text{mzi}}(z_0) \tag{4.1}$$

With

$\delta z_{\text{mzi}}(z_0)$ the smallest z_0-resolution, which is obtained by the MZI at value z_0 (corresponding to $\theta = 0$). For calculating this value we have taken the N'_{eff}-resolution of a MZI without modulators to be 5×10^{-7};

$\eta = 0.01 - 0.001$ for an accuracy 1% - 0.1%;

$z_{0,\text{min}}$ is the minimal distance between mirror and waveguide and it has been calculated already, that $h_{\text{min}} \geq 3.2\,\mu\text{m}$. In further calculations we have taken $h_{\text{min}} = 3.2\,\mu\text{m}$.

For getting some feeling of the N'_{eff}-effect we have calculated the z_0-dependence of $\Delta N'_{\text{eff}}$ for the same mirror system (see Figure 4.11).

For determining $z0, \max$ both the left-hand side and the right-hand side of the equation have been plotted (Figure 4.12) as a function of z_0; the straight line corresponds to $\delta z_{\text{mzi}}(z_0)$. The z_0-section in between the

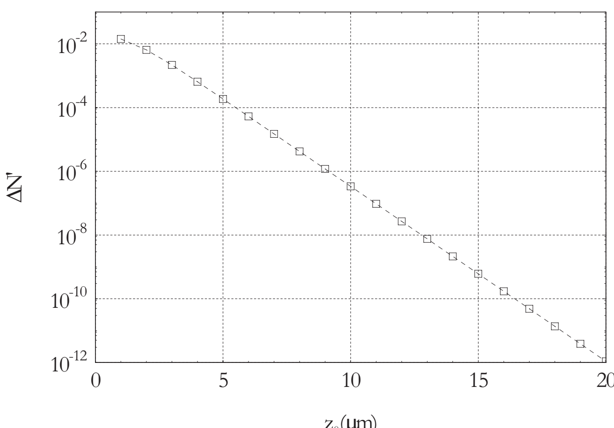

Figure 4.11: $\Delta N'_{\rm eff}$ versus airgap z_0 at 1550 nm wavelength when the fundamental TM mode propagates through a 100 nm thick free-standing slab waveguide and where a gold coated silicon MEMS part penetrates the evanescent field region

line crossings represents the range of z_0-values fulfilling the accuracy requirement. Following the 1% accuracy requirement the maximum value of $z_0 = 9.75\,\mu\mathrm{m}$, but to be more safe as to the technological tolerances $z_{0,\max} = 9.5\,\mu\mathrm{m}$ has been chosen. At this z_0-value, a free rotation of 2.5° requires $x < 217\,\mu\mathrm{m}$ while in order that $z_{0,\min} = 3.2\,\mu\mathrm{m}$, $x_a = 145\,\mu\mathrm{m}$.

Combining all results we end up with the design of the sensing region where the mirror interacts with the optical mode shown in Figure 4.13 and Table 4.3.

4.4 Influence of IO wafer on the electrical field

Anticipating on data of the structures to be designed and produced we state here that the field disturbance due to introduction of the optical wafer is negligible, a result obtained in grace of UT colleagues which had software available for calculating electrical field distributions in such 3D-structures and who were willing to perform the necessary calculations.

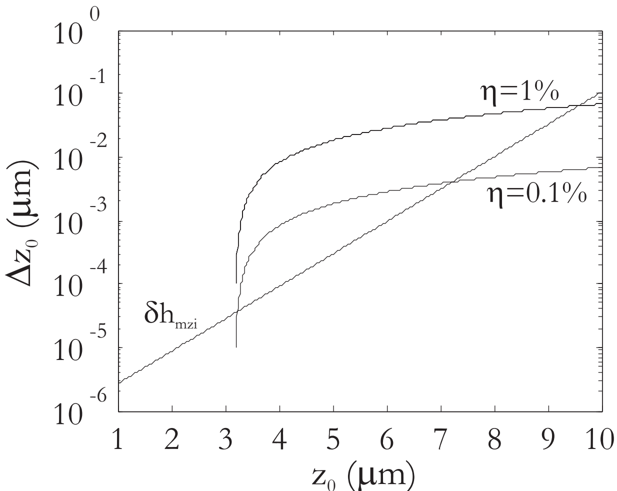

Figure 4.12: Graphical solution of Equation 4.1. The straight line shows the calculated resolution of the MZI. The curved lines indicate the values of 1% and 0.1% resolution. The section between crossings of a curved line and the straight line represent the range of z_0-values fulfilling the accuracy requirement

4.5 New technological challenges

Some parts of the foreseen MOEMS structure are not known from literature and they have to be analysed and designed in close interaction with the technology to realise them. This concerns the IO membrane-bridge structure and the process of making the MOEMS systems from the individual IO-, and MEMS- wafers and some glass slides.

The bridge waveguide structure

As argumented before, the sensing section of the IO readout system, where the mirror interacts with the optical mode in the membrane waveguide, must be implemented as a bridge-type structure in which the membrane is locally provided with silicon supports. As derived in previous section the performance requirements give us some room for the width of the Si supported section of the bridge: in between 25 and 43 μm.

For realising such a Si supported Si_3N_4 membrane structure, two fabrication methods have been considered:

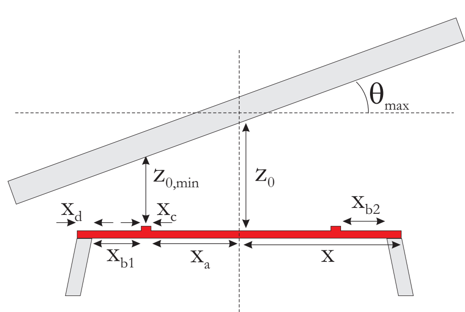

Figure 4.13: Relevant geometrical parameters of the IO-mirror system,

Parameter	Value
x_a	145 µm
x_b	25 µm
x_c	4 µm
x_d	25 - 43 µm
x	199 µm- 217 µm
h_r	6 nm
z_0	9.5 µm
$z_{0,\mathrm{min}}$	3.2 µm

Table 4.3: Values of the relevant geometrical parameters shown in Figure 4.13

The 'underetch' method

The Si_3N_4 layer is locally made free-standing using a local 'underetch' by KOH etching starting from trenches or holes (see Figure 4.14(a)) applied by DRIE at the topside of the ⟨100⟩-wafer, as shown in Figure 4.14.

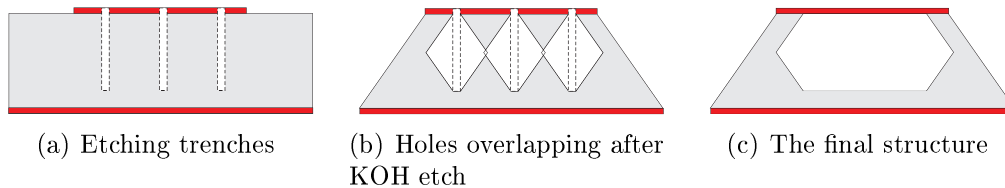

(a) Etching trenches (b) Holes overlapping after KOH etch (c) The final structure

Figure 4.14: Illustration of the underetch method, showing the state just before the wet etching, the state where the etched holes overlap and the final structure

Because the ⟨111⟩ planes starting from two bottom of two adjacent trenches have to cross each other at an height just below 1/2 $d_{\mathrm{trench,Si}}$, the trench depth $d_{\mathrm{trench,Si}}$ can be given as a function of the distance between the trenches at opposite sides of the MZI structure, d_{dist}.

$$d_{\mathrm{trench,Si}} = d_{\mathrm{dist}} \tan(54.7) \tag{4.2}$$

In reverse, a given trench depth defines the maximum distance between two adjacent trenches, which affords etching away all material in between.

The 'backside-etch' method

The Si_3N_4 layer is locally made free-standing using a 'back-side etch' locally removing the silicon over whole the wafer thickness en ending up with a structure as given in Figure 4.15.

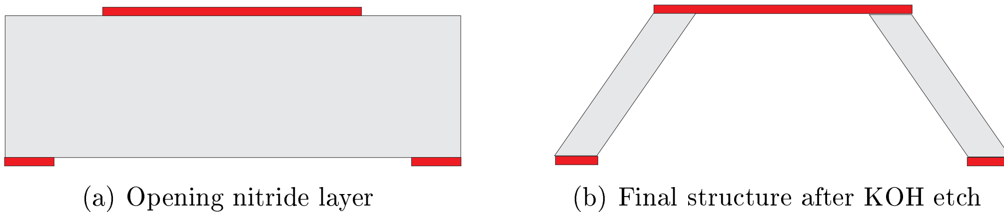

(a) Opening nitride layer

(b) Final structure after KOH etch

Figure 4.15: Illustration of the backside-etch method

Analysis and preliminary experiments on both fabrication methods

Principally, the 'underetch' method is expected to result into a stronger more rigid structure due to the large silicon backbone. However some precaution has to be taken in order to avoid that the holes (or trenches) which have to be applied alongside the waveguide channel should not interfere with the guided mode.

For the channel structure, as defined in Section 4.3, at 1550 nm wavelength the minimum distance between the ridge edge and a disturbation like a trench has to be 26 µm (as derived in Section 4.5) to have a negligible effect of the trench on the mode propagation. Hence, the minimal distance between both trenches edges on opposite sides of the waveguiding channel, d_{dist}, has to be 56 µm. Then, applying Equation 4.2, a minimal trench depth of 80 µm is required for obtaining a free-standing membrane. Not only this minimal distance, but also the required width of the trench determines whether such a trench can be fitted spatially inside the Si bridge structure as given in Table 4.3. Trenches or holes can be applied in the MESA+ clean room by a DRIE process, in which the aspect ratio (that is, the ratio trench depth over trench width) is about 20. So, the minimum lateral size of a trench (hole) should be 4 µm. However, the larger the trench width the faster the etching process and the smaller the chance that the etching process would be blocked by gas bubbles sticking inside the trench.

For getting some idea of the limitations of the DRIE etching process we have performed some preliminary experiments. In the SiO_2/Si_3N_4 layer stack, two rows of $4 \times 4\,\mu m^2$ square holes have been etched. The distance

between the centres of the rows was 34 µm and the distance between the centres of two adjacent holes in one row was 14 µm. The standard Si-DRIE process was performed during 14 minutes resulting into an etch depth of 20 µm.

In Figure 4.16(a) a cross sectional view (microscope photograph) is given of a partially underetched membrane. In Figure 4.16(b) and 4.16(c) top views (microscope photographes) of the structures are presented: Figure 4.16(b) shows an intermediate stage of the etching process in which the Si in between two holes in the same row have been disappeared already, while Figure 4.16(c) presents the final stage.

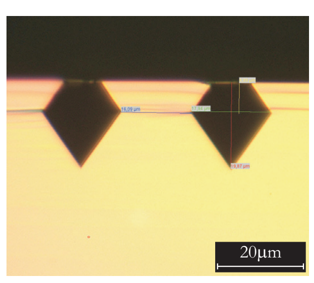

(a) cross section of a partially underetched membrane

(b) top view of a partially underetched membrane

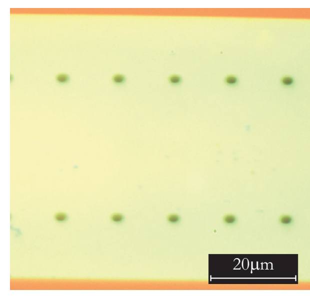

(c) top view with a completely underetched membrane

Figure 4.16: Microscope photographs of underetch method

However, the preliminary experiments also showed some lateral underetch of the Si underneath the Si_3N_4 layer. Finally, this underetch results in a triangular cross section of the hole as is also obtained in common V-groove etching.

We have measured the etch rates indicated in Figure 4.17: $R = 0.35\,\mu\mathrm{m}/\min$ and $r = 0.13\,\mu\mathrm{m}/\min$, while in wide trenches the etch rate R is about 1 µm/ min. Apparently, the slower transport of the etchants and reaction products through the narrow hole is lowering the etch rate remarkably. Assuming that this lateral underetch is reproducible, the additional widening of the hole at the Si-Si_3N_4 interface can be given as

$$w_l = \frac{r}{R}\frac{d_{\text{trench}}}{\tan(54.7)} \tag{4.3}$$

Assuming Equation 4.3 to be independent of the hole depth and taking the latter 80 µm an additional widening of 21 µm can be calculated. From

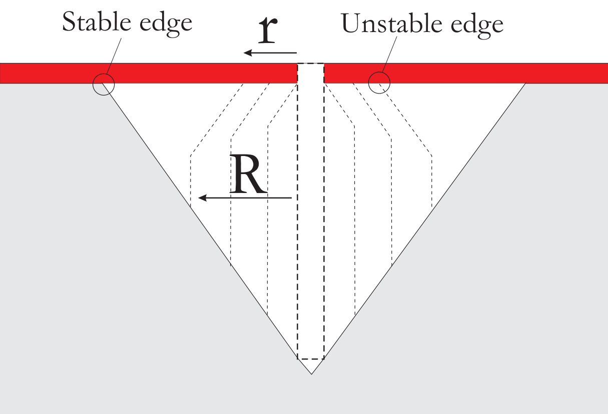

Figure 4.17: Different stages when underetching Si in KOH through trenches

the data given in Table 4.3. it can be calculated that in that case the maximum width of the Si bridge would be 18 µm only. Taking into account the uncertainty in etch rates we considered this structure as being too risky and too fragile for applying trenches. The structure would be more rigid when applying holes. Also, holes application gives some freedom in diminishing the minimal distance from a hole to the waveguiding channel: a segmented structure as described in [vL05] will be formed and taking some criterion for the maximally tolerable hole induced modal losses (for example 1 dB) a second and lower minimal hole-channel distance can be calculated: 21 µm, being 4 µm lower only than the originally chosen value of 25 µm. We considered also this structure as too fragile and hence the process as very risky. Notice also, that now alignment inaccuracy will disturb the balance of the MZI.

The alternative is KOH etching from the backside with the objective to create 46 µm wide Si supports. Preliminary experiments showed, that using one KOH etch step only gives to much spread in Si-support thickness and hence we decided to apply a two step KOH etching process, adapting the duration of the second etch step to the (measured) size of the structure after the first etching step. Based on these preliminary experiments, we have chose to apply the *back-side etch* method for the fabrication of the bridge structures.

Realised bridge structures

Using the chosen fabrication process, bridged membrane waveguides were fabricated with 90% yield. A microscopic photograph of a realised bridge-

structure is shown in Figure 4.18.

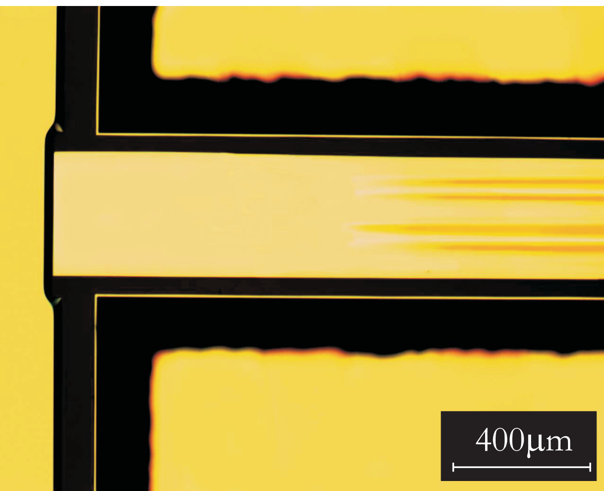

Figure 4.18: Microscope image of a realised bridge-structure showing the Si_3N_4 membrane and the Si support beams

Remarkable in the figure are the dark lines parallel to the length axis of the bridge. The dark lines point to some position dependent interference phenomena and hence to some deformation of the membrane. This idea is supported by the observation that the width of the bridge in the middle of the membrane is about 3% smaller than at the ends, where the membrane is clamped. This deformation cannot be caused by stresses in the Si_3N_4 membrane because these are tensile and we tend to attribute them to stresses inside the irregularly shaped thin silicon supports. The regular shape of the deformation makes random thickness variations as origin of the deformation improbable.

In principle, the way the membrane has been deformed and the magnitude of the deformation can be measured using some special types of interference microscopy. Unfortunately, such equipment was not available. Because of lack of time we were unable to pay more attention to this phenomenon and we felt to be forced to go on with this type of bridges.

Electrical influence of the bridge structure

Having defined the nature of the silicon supported membrane structure and having an idea of its dimensions we can return to the question whether the presence of this partly conducting structure, positioned between the mirror and the electrodes would appreciably disturb the electrostatic forces

at a given actuation voltage which drive the mirror. Here we acknowledge the help of our UT colleague Dr.Ir. Toon Kuijpers who had FEMLAB [Com] software available for calculating electrical field distributions in 3D structures and who was so kind as to perform the necessary calculations. From these calculations it is concluded, that the bridge structure causes a minor and well acceptable change of the electrical field distribution only. Hence the influence of the presence of the bridge structure on the relation between actuation voltage and deflection is not seriously influenced by the bridge structure.

The wafer bonding

The complete demonstrator is developed as a stack of three separate wafers that are mutually connected by wafer bonding. Because in the original MEMS structure the thickness of the distance wafer is 320 µm we had to apply for the IO part Si wafers of similar thickness (340 µm) in order to have a similar $\theta - V_{\text{act}}$ relation. For bonding wafers together various factors have to be considered: on the one hand the bonding principle and conditions, on the other hand the material combination, the flatness of the wafers and the surface roughness of the materials which will be bonded together. For the bonding of the IO wafer and MEMS wafer outer faces consisting of low index SiON and silicon respectively are offered and it is known that under certain conditions concerning the flatness (preferably a curvature resulting in a height difference of centre and edges of the wafer smaller than 90 µm) and surface roughness (preferably less than 1 nm), these materials can be well bounded together using fusion bonding [GAG+97].

First we consider the flatness aspect. The MEMS wafer is essentially a structured Si wafer and will show an excellent flatness. Because of stresses in the optical layer stack the flatness of an IO wafer with the optical layer stack at one side of the wafer only would be poor. To avoid the very complicated and uncertain research on obtaining stress free layer stacks we decided to compensate for these stresses by applying similar layer stacks at the bottom site of the IO wafer.

The outer face of the MEMS wafer is the original surface of the polished Si wafer and this will show a surface roughness that does not exceed several Å. It is well known that the roughness of a some micrometre thick PECVD SiON layer is relatively high [GAG+96, GVK+98] (in the order of magnitude of 2 nm RMS) preventing to get a stable bond. This roughness can be reduced to 0.2 nm RMS by applying CMP [GAG+96, GVK+98], but this polishing has to be done before the fragile membrane structure has been made. The long time lasting KOH etching process, which is applied for

removing locally the silicon under the Si_3N_4 core layer would result into an increase of the surface roughness of the SiON out layer. For protection of this surface a thin Si_3N_4 layer will be applied on top of this CMPed SiON layer. A process has been developed at TUC to bond the Silicon to the Si_3N_4 layer and preliminary experiments have proven the feasibility of this method (see Appendix A)

For avoiding sticking of the mirror to the IO bridge 200 nm high bumps are applied on top of the IO-wafer (see Appendix B). In a bare MEMS device, the Pyrex electrode containing slide can be bonded to the Si of the MEMS wafer by anodic bonding. Because the outer layers of the IO wafer are electrically isolating this method cannot be applied here. For bonding the Pyrex wafer to the IO wafer, at TUC a process has been developed in which SU8 polymer is applied as an intermediate layer on top of the Pyrex slide enabling a stable bond with the IO wafer after pressing both wafers together while heating them to 200°C.

After bonding the MEMS wafer to the IO Wafer and the Pyrex wafer to the MEMS-IO wafer stack, the complete structure will look like the illustration shown in Figure 4.19.

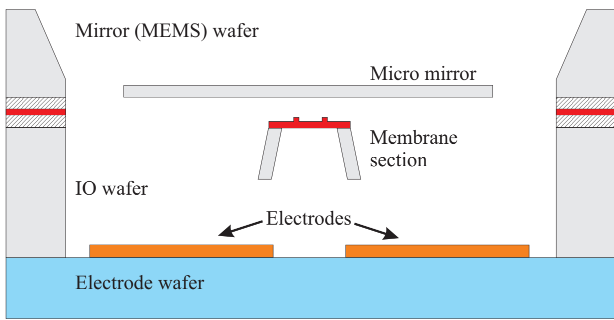

Figure 4.19: Illustration of the complete micro-mirror demonstrator after bonding of the three wafer.

4.6 The final design and the realisation of the structures.

Based on all aforementioned considerations and on knowledge of factors influencing the resolution of a MZI structure given in [HL99], we have decided to realise the IO system as shown in Figure 4.20.

The final IO circuitry

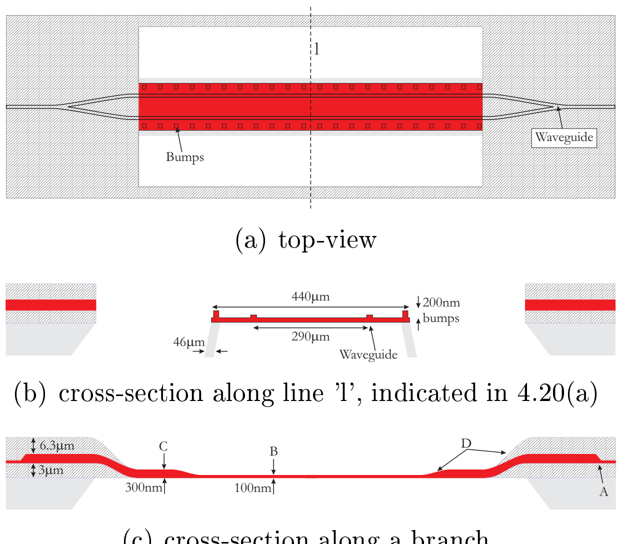

(a) top-view

(b) cross-section along line 'l', indicated in 4.20(a)

(c) cross-section along a branch

Figure 4.20: Schematic structure of the IO circuitry consisting of a MZI with free-standing membrane waveguides. 4.20(a): topview, indicating the position of the MZI WG, 4.20(b): cross-section of the sensing area showing the bridge-section, and 4.20(c): a cross-section along one of the branches of the MZI, showing the FC-coupling section, the adiabatic taper sections and the membrane at the sensing area

Some more information:

- light of the required polarisation state is launched at the input of the IO circuit from a single-mode fiber; output light is collected by a multi-mode fiber;
- four different sections (A,B,C,and D, see Figure 4.20(c)) show different values of the thickness of the core layer:

A an efficient fiber to chip coupling requires a core layer thickness of 70 nm (length of this section is 0.5 mm);

B the sensing region itself shows a core layer thickness of 100 nm as discussed earlier (length of this section is 5 mm);

C a Si_3N_4 core layer showing thickness of about 300 nm, which enables a complete confinement of the modal field within the waveguiding layer stack without the need for excessive thick cladding layers;

D taper sections of gradually varying core layer thickness, which enable adiabatic propagation of the mode in that way reducing transition losses (taper angles are 3 and 0.3 degrees for the SiO_2 and Si_3N_4 layers respectively).

- the waveguides have been designed for supporting one TM mode only, at a wavelength of 1550 nm in all four section ($h_{\text{ridge}} = 6\,\text{nm}$, $w_{\text{ridge}} = 4\mu m$);
- the thickness of the SiO_2 cladding layer (6.3 µm) is adjusted to the desired gap width (9.5 µm);
- the thickness of the SiO_2 buffer layer is 3 µm;
- The lateral lay out is adapted to the structure on the MEMS wafer.

A detailed technological process has been developed and applied for realising the IO system and the subsequent building up of the complete MOEMS structure provided with fiber pigtails. This process is given in Appendix B.

Mechanical characterisation of the micro-mirrors

During execution of the total project TUC performed a detailed characterisation of the mirror structure in rest and during movement using microscopic interferometry. Both features appeared to be far from the idealised picture, which had been the starting point of our design. Main conclusions were:

- in the undriven situation, the centre of the mirror is 0.72 µm below the bond surface which is caused by bowing of both hinges of the mirror (0.48 µm) and the mirror itself (0.24 µm);
- in the static drive mode, the mirror experiences a parasitic vertical translation which depends on the actuation voltage, see Figure 4.21.

To cope with the bowing of mirror and hinges in the undriven situation, TUC applied a backetching of the mirror surface, effectively moving the mirror plate and hinges below the bonding surface.

An IO system consisting of a ψ-junction, as shown ing Figure 4.22, where the two outer branches are defining an MZI and the middle branch, positioned below the rotation axis of the mirror, is used for attenuation based measurements, may cope with this parasitic vertical translation. Unfortunately, no time was available to implement this structure.

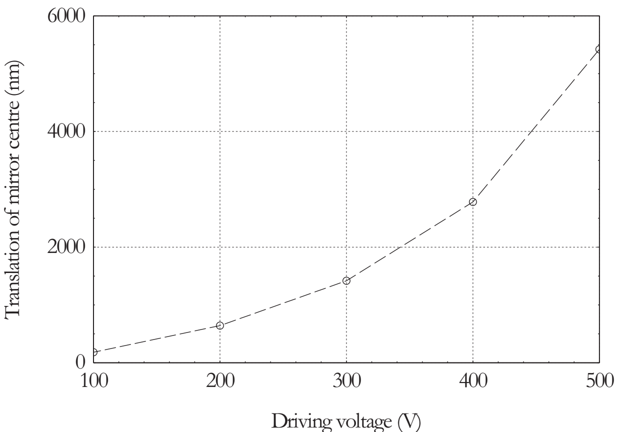

Figure 4.21: Parasitic translation of the micro-mirror as function of the static driving voltage

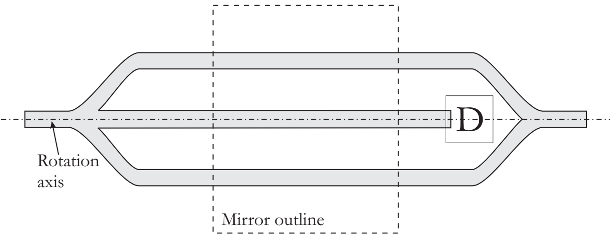

Figure 4.22: Schematic topview of a ψ-junction containing read-out configuration. Shown are the branches of the IO system, a photo detector applied in the middle branch and the outline of the micro-mirror (dashed lines).

4.7 Characterisation of the mirror demonstrator

After realisation of the complete demonstrator, several characterisations were performed on the demonstrator.

Visual observations

A first wafer containing the complete MOEMS structures has been realised. Bonding had been performed by TUC. Microscopical observation showed that the mirrors were well aligned to the bridge structures, without any sticking. Unfortunately, during dicing, the bond between the Pyrex wafer and the IO wafer (SU-8) loosened and as a consequence all bridge structures had been broken.

A second IO-MEMS containing wafer set has been prepared of which the bonding processes were performed at MESA+. For finalising this wafer set, a different approach was taken to prevent failure of the Pyrex wafer-bond: after bonding the IO and MEMS wafer, this set was diced; then, the individual Pyrex electrode wafers ware diced and bonded to the IO-MEMS wafer set using a UV-curing glue. Next, the individual MOEMS structures have been fitted with single-mode fibers for incoupling of the light and multi-mode fibers for outcoupling. However, after bonding of the IO and MEMS wafers, in all not damaged MOEMS structures the mirror appeared to touch the bridge structure unfortunately.

Yield was about 60%; main failure appeared to be the fracture of the bridge. Photographs of the realised demonstrator are shown in Figure 4.23

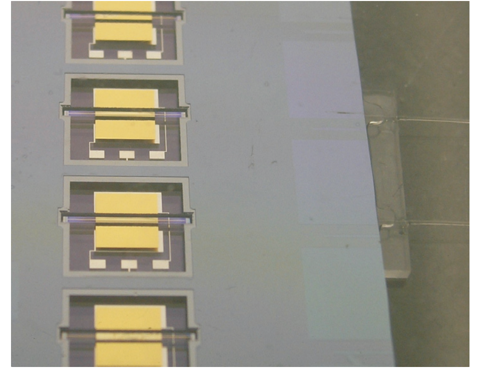

(a) Frontside, showing the bridge waveguide, mirror and fibres

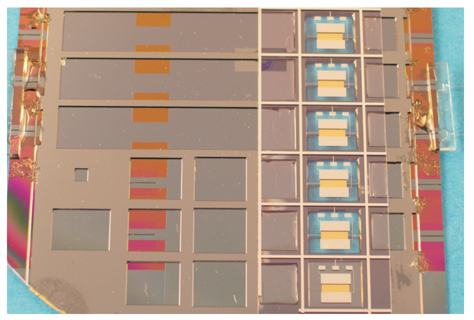

(b) Backside, showing the driver electrodes

Figure 4.23: Photographs of the realised micro-mirror demonstrator

By carefully applying some pressure on the mirror (by pressing a tweezer against the mirror surface), the contact between the mirror and the waveguiding membrane could be removed, but immediately after lifting the pressure the touching reappeared. It has been tried to separate mirror and bridge by repelling electrostatic forces originating from applying a high voltage on both parts. For observing a possible mirror movement we send a collimated light beam generated by a HeNe laser to the mirror and monitored the shift of the spatial position of the reflected beam by a position-sensitive quadrant detector (PSD) (see Figure 4.24). Due to spatial limitations, the plane of incidence of the beam was parallel to the rotation axis of the mirror.

However, this repelling DC voltage did not result into any change of the output signals of the PSD, neither any change of the optical insertion loss of the MOEMS had been observed. Most likely, the Si bridge supports are

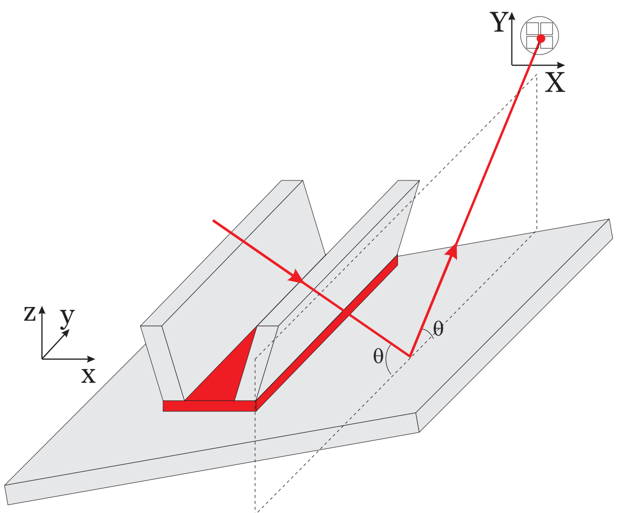

Figure 4.24: Mirror movement detection using quadrant detector

too small to accumulate sufficient electrical charge to achieve the mirror to be pushed off. Also, anticipating on the touching of mirrors and waveguide in another MOEMS, the electrode plate has been applied on the backside of the MEMS wafer to allow application of a DC voltage between electrodes and mirror to achieve the separation. Limitations of the wirebonder made it impossible to make conducting connection to the driving electrodes by applying wirebonds. Therefore, mechanical probes were used to supply the required driving voltage to the electrodes. Unfortunately, the attracting DC voltage did not result in any observable separation of waveguide and mirror.

4.8 Measurement of the relation between actuation voltage and optical transmission losses

In spite of this contact between mirror and bridge we decided to perform some measurements to determine the relation between actuation voltage and optical attenuation of such a MOEMS system. The specific system was fitted with the driving electrodes at the backside of the MEMS wafer, as described above.

Application of the actuation voltage

To drive the micromirror, the mirror plate itself is shorted to ground while a sinusoidal voltage is supplied to the driving electrodes. The driving voltages on the electrodes are in anti-phase in order to obtain the desired push-pull action. A DC-component can be added to the driving voltage in order or see whether this will achieve a less hampered rotation of the mirror.

The electrical setup for the driving of the mirror is shown in Figure 4.25.

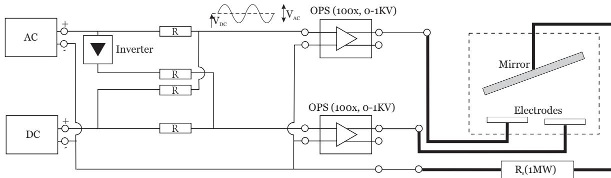

Figure 4.25: Electrical configuration for driving the mirror demonstrator

The output voltage of the AC-source is fed to into two circuits; in one circuit the AC voltage is added directly to the voltage generated by a DC-source, while in the the second one AC signal is fed to an inverter, creating a 180 degree phase shift, before being combined with the DC-signal. Each of the obtained voltages, being a superposition of a DC and a AC voltage are fed to separate amplifiers (operational power amplifiers, OPS) to enhance the voltages to the values aimed at, and next the latter are supplied to the driving electrodes through the mechanical probes.

Experimental results

Visual observation of the scattered light of the MOEMS configuration using 632.8 nm wavelength light from a HeNe laser showed that the transmission losses of the ridge type waveguiding channels were not excessively high in spite of the touching of the mirror to the IO bridge. The output of the quadrant-detector showed, that at applying a sinusoidal voltage to the electrodes the mirror did rotate indeed, in spite of the contact of mirror and bridge.

Figure 4.26 shows the simultaneous recording of the optical output and the signal obtained from the quadrant detector.

The touching of the mirror and waveguide hampers comparison of experimental results and theoretical predictions. It is unknown where exactly the touching occurs and no knowledge is available of the distance between the waveguide and the mirror surface at the position of the ridge waveguide.

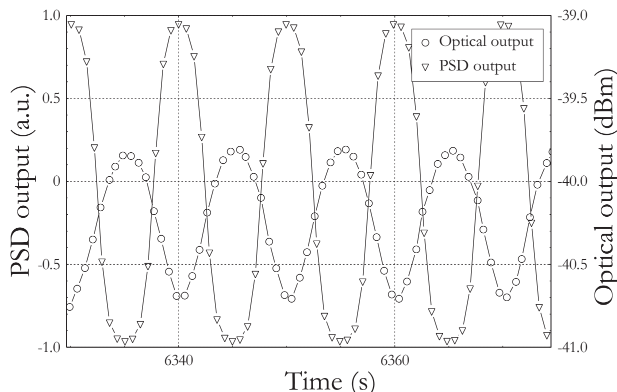

Figure 4.26: Optical output and quadrant detector signal (X-shift) as function of time for mirror-demonstrator

Also the rotation itself can be strongly influenced by the mirror-bridge contact, for example, by inducing additional deformation of the mirror plate.

Considering the problems arising from deformation of the membrane in the second bridge structure where the bridge is realised by etching from the back side of the wafer, the preference of this structure above the other one has to be reconsidered. Additional optical losses due to the segmentation in the first bridge structure may be compensated by using a light source of higher optical power. If it would appear that this bridge structure would not be liable to deformation, a well defined MOEMS structure would be obtained, which would enable indeed a clear interrogation of its mechano-optical properties.

4.9 Summary

For the micro-mirror demonstrator, the IO structures comprising fibre-to-chip couplings, adiabatic tapers and the free-standing membrane sensing section have been designed and fabricated. Two methods for creating a bridge-type waveguide have been developed and tested. The complete demonstrator has been made using waferbonding. It appeared that the micro-mirror and the membrane waveguide were touching each other. This unexpectedly touching hampered a proper characterisation of the MOEMS and hence a proper evaluation of the read-out method.

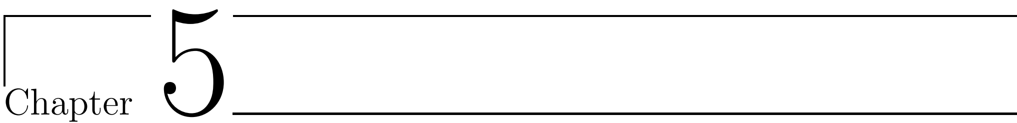

Chapter 5

The PZT Membrane demonstrator

5.1 MEMS characteristics

PZT actuated membrane devices, to be produced by Thales RT will function as the MEMS devices in this demonstrator. The structure of such a membrane device is given in Figure 5.1. The devices are produced from SOI wafers. The membranes themselves consist of a thin Si layer (A) on top of which a PZT layer (B), sandwiched between two platinum electrodes (C and D) has been applied locally for driving the membrane. The PZT layer has been poled to make it piezo-electric.

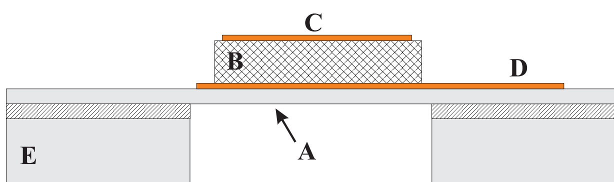

Figure 5.1: Illustration of the PZT membrane MEMS device (side-view)

5.2 Relevant properties of the membrane devices

- Thales RT can realise various modifications of these devices differing in shape and dimensions of the membrane. After discussions with Thales-RT and LOPMD it was decided to focus on a device of which the lateral membrane dimensions are $4 \times 4\,\mathrm{mm}^2$;

- Under static conditions the maximum deflection of the centre of the membrane is about 0.3 µm (at the maximum value of the actuation voltage, 10 V). At the resonance frequency of the fundamental mechanical mode (30 kHz) at a 10 V AC voltage this deflection increases to about 15 µm. (shown in Figure 5.2).

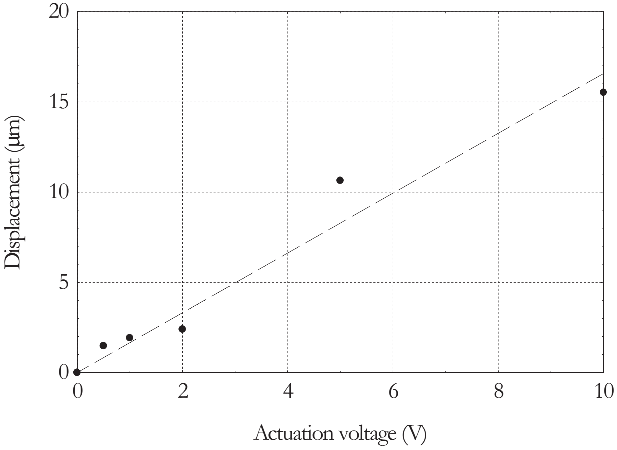

Figure 5.2: Deflection of the centre of a membrane as a function of the applied voltage (at resonance)

5.3 Requirements to the read out of the membrane system

From discussions with Thales-RT, it appeared that the IO readout-system for the membrane demonstrator should have the following capabilities:

- Accuracy of the (average) deflection and resonance frequency about 1%.
- No effects of the read-out system on the properties of the MEMS system.

5.4 The design of the PZT-membrane demonstrator

Just as in the mirror demonstrator in the membrane demonstrator the optical read out will be performed by a MZI structure. The design consider-

ations show many similarities to those given for the mirror demonstrator. Most remarkable difference is, that opposite to the mirror structure the moving MEMS part has not to traverse locally the waveguiding layer stack and hence there is no necessity to apply holes in this layer stack. Here, the membranes can be all sided clamped to the Si main frame and no bridge structures are needed. So the simpler membrane structures as described in Chapter 3 can be applied. A second difference is, that unlike the mirror-demonstrator, the PZT-driven membrane-demonstrator cannot be operated in a push-pull configuration as the movement of the membrane is unidirectional across the entire membrane. Therefore, an unbalanced interferometer configuration has to be used, where one branch of the MZI interacts with the membrane while the other branch, the reference branch, is positioned outside the membrane section. Also the material to be driven into the evanescent field region of the read out system is different, in this demonstrator being the platinum forming the 200 nm thick upper electrode of the PZT layer.

Additionally, it was decided that the MZI in this demonstrator should encompass also the ZnO electro-optical modulators and the ETWI in order to demonstrate the feasibility of these functions too. Essentials of the structures are depicted in Figure 5.3.

Using identical structures of the optical channel guides as in the mirror demonstrator, for defining the cross sectional structure of the interaction region one essential parameter has to be defined yet: the distance between the membrane in rest and the Si_3N_4 surface, z_0.

The relevant effects of driving Pt into the evanescent field region, on the optical transmission have been presented in Figure 5.4.

Just as in the mirror demonstrator the main aim here is to determine the static deflections ($\Delta z_0 = 0.3\,\mu\text{m}$ at $V_{\text{act}} = 10\,\text{V}$) with highest accuracy and to adapt the actuation voltage at measuring the frequency dependence of the deflection to the limitations of this specific structure. Following the same lines of discussion as given in Section 4.3 for the mirror demonstrator, we arrive at a value of $z_{0,\text{min}}$ of 5.3 µm; a lower value would result in unacceptable losses. The value of z_{min} plus the maximum static deflection (5.3 µm + 0.3 µm = 5.6 µm) is a little below the minimum thickness of the optical layer stack. Therefore, for this demonstrator, $z_{0,\text{min}}$ has been chosen to be 6.2 µm).

The design freedom of the lateral lay out of the MOEMS structures was seriously limited by the Thales condition, that the membranes had to be produced on the same wafers as the membrane structures to be applied by LOPMD. In these wafers the LOPMD membranes should occupy the middle region of the wafer leaving for the MESA+ membranes the side regions only

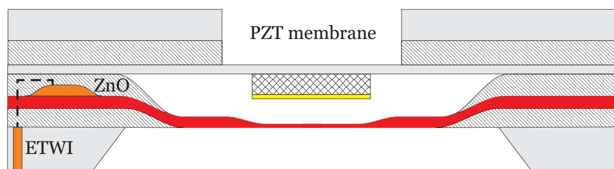

(a) Longitudinal cross section along the one branch of the MZI

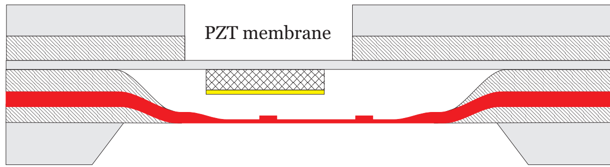

(b) Cross section perpendicular to the waveguides across the sensing area

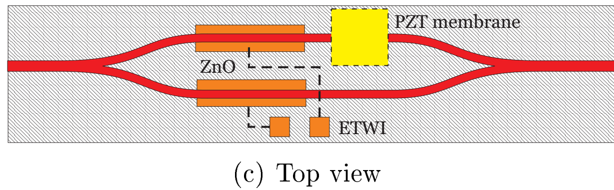

(c) Top view

Figure 5.3: Different views of the PZT-membrane demonstrator

(see Figure 5.5(a)). Here the space for the MZI's is very limited. To utilise this space optimally and to simplify the fiber to chip connection process we decided to apply bended MZI's and a schematic top view of the optical structures is given in Figure 5.5(b) as a close-up of Figure 5.5(a) with the IO structures superimposed on it. Note that here also the length of the ZnO containing sections has been varied in the range 31 mm- 38 mm, amongst others to cope with the uncertainties concerning the electro-optical properties of the ZnO at 1550 nm wavelength. Even if the wavelength dependence of the electro-optical coefficients would be small, application of 1550 nm wavelength in stead of the normally used 632 nm or 850 nm wavelengths would require a longer interaction length because the electro-optically obtained phase difference is proportional to the reciprocal of the wavelength.

For these structures the bending radius has to be defined. For functional bending losses to be lower than 1 dB/ cm, the bending radius of the given channel structures has to be larger than 6 mm. For safety reasons we have adopted to maximise the bending radius being limited by the usable area on the wafer: this resulted in a bending radius of 10 mm.

The technological process for realising this type of MOEMS structures

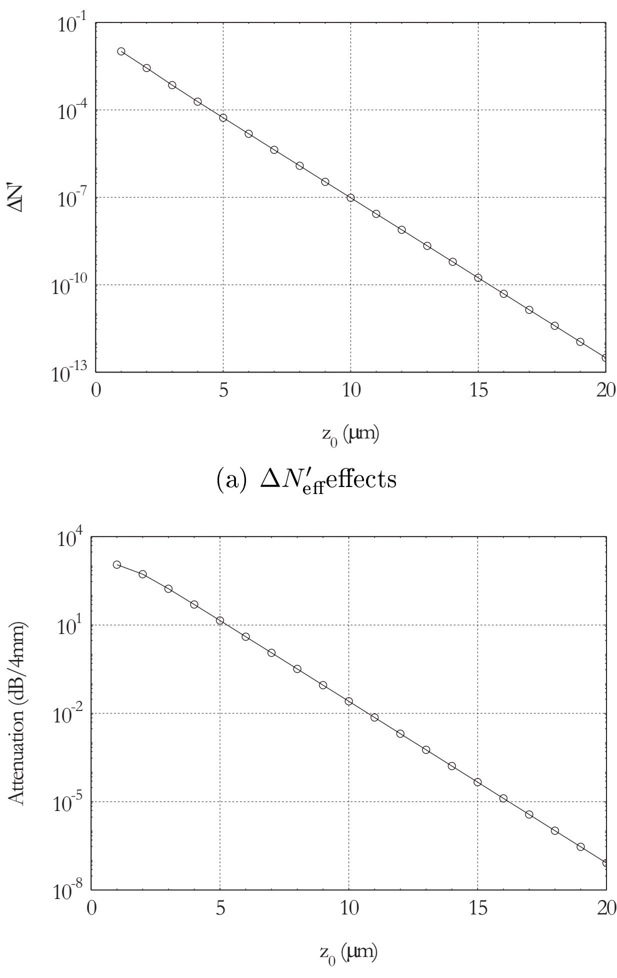

(a) $\Delta N'_{\mathrm{eff}}$effects

(b) $\Delta N''_{\mathrm{eff}}$effects (as attenuation in dB/4 mm)

Figure 5.4: Calculated changes of the real and imaginary part of the effective index of the guided TM_0 mode as a function of the air gap z for a free-standing membrane waveguide with PZT with a Pt coating as penetrating material

contains many steps which have been discussed and described already in Chapter 4.

Three technological sub-processes have to be investigated however: making ETWI's, depositing ZnO with optimal (electro-) optical properties at 1550 nm wavelength and depositing tapered ZnO structures for bended waveguiding channels.

Development of the first two sub-processes was the task of Lionix. In the development of the ETWI, MESA+ has been involved too and for that

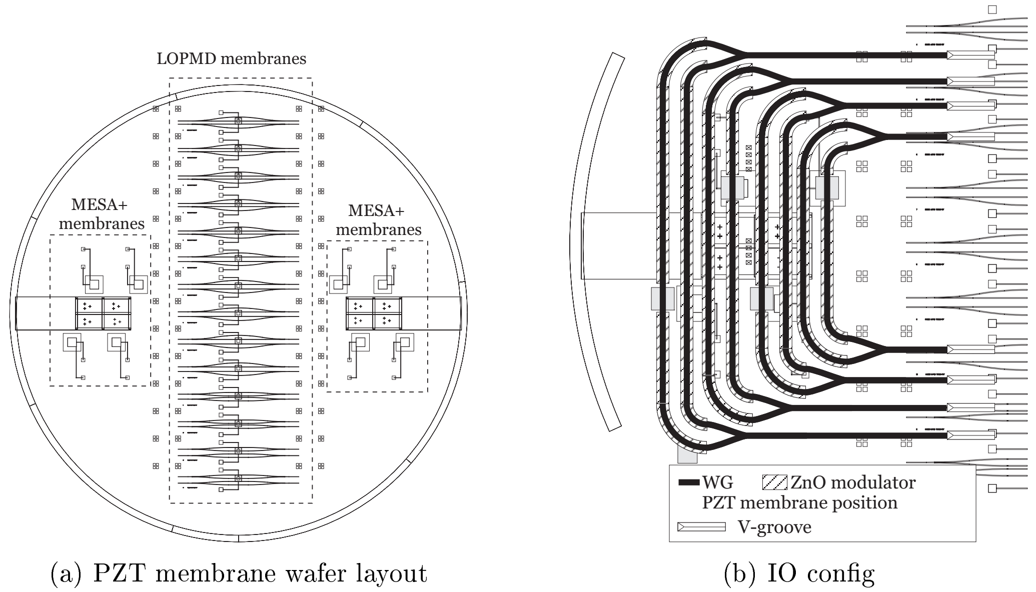

(a) PZT membrane wafer layout (b) IO config

Figure 5.5: Top-views of the MZI-PZT membrane configurations. 5.5(a): a top-view of the MEMS wafer indicating the positions of the different types of PZT membranes 5.5(b): a top-view of the IO configuration with respect to the PZT membranes on the MEMS wafer

reason we will describe it in more detail in Appendix D. For depositing the required bended tapered ZnO regions we shall use shadow masks with a structure given in Figure 5.6(b), (which can be realised by stepwise DRIE etching of a Si wafer) instead of the common KOH- etched masks (see Figure 5.6(a)) which can be applied for straight channel sections only.

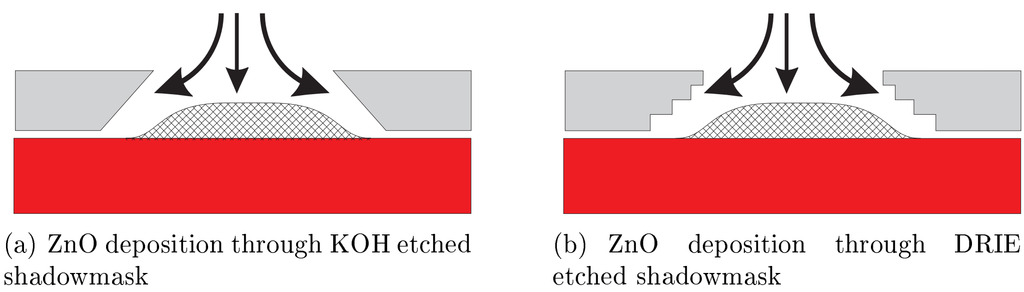

(a) ZnO deposition through KOH etched shadowmask

(b) ZnO deposition through DRIE etched shadowmask

Figure 5.6: Two different shadowmasks for ZnO deposition

Unfortunately, Thales RT delivered membrane wafers which, as microscopic observation showed, contained structures, apparently meant for the demonstrators of LOPMD, in the electrode layers. These structures cause

height differences in the top layer of the wafer which was meant as *bonding surface* for the MESA demonstrator. Bonding of these membrane wafers to an optical wafers was deemed very unlikely. Due to the fragile nature of the PZT membranes, performing a CMP polishing step on the mechanical wafers was impossible. In addition, many of the membranes on the wafer appeared to be broken, resulting in a yield of about 30%. Due to time and financial restrictions, Thales RT was unable to supply MESA+ with other MEMS wafers for completion of the demonstrator.

Therefore, unable to continue work on this demonstrator, it was decided to stop further research on this demonstrator.

5.5 Summary

Directed to fulfilling the requirements the structure of the vibrating membrane demonstrator has been designed. Because it was decided to implement in the IO wafer Electrical Through Wafer Interconnects and to apply a serrodyne modulated MZI for read-out, the technological process for realising the optical circuitry for the mirror demonstrator had to be modified somewhat. The ETWI development has been discussed in more detail in Appendix D. Also, an new type of shadow mask for ZnO deposition, allowing deposition in arbitrary shapes, has been developed and tested.

Unfortunately, the complete demonstrator could not be realised due to irregularities in the bonding surface of the mechanical wafer, which had been produced by Thales RT, as a result of the presence of structures meant for the LOPMD demonstrator.

The MEMS gyroscope demonstrator

6.1 Introduction

This chapter deals with the third demonstrator of the OCMMM project: a MOEMS demonstrating the optical read out of a micromachined MEMS gyroscope as is being developed by Thales-Av. The aim of this demonstrator is to show the potential of an evanescent field sensing based measurement method for read out of the movements of some micro-mechanical parts of the gyro. The latter reflects the change of orientation of the gyroscope.

The origin of the interest of Thales-Av in these investigations is twofold. Firstly, Thales-Av. desires to know whether the optical read-out method might be competitive to the electrical capacitive read-out method, which they are applying nowadays. Hence, the limits of this demonstrator device have to be investigated.

Secondly, Thales-Av. aims at determining resonance frequencies of moving parts during MEMS production (requiring a non permanently bonded MOEMS system) in order to enable their adjustment to the required values during production.

The structure of this chapter is as follows:

In Section 6.2 we present a short introduction into vibratory MEMS gyroscopes, followed by a description of the MEMS gyro as will be produced by Thales-Av and a list of requirements/desires to the MOEMS system.

In Section 6.3 we present a theoretical analysis of three different read our systems: in the first one the read out is based on the attenuation effect, in both other ones the read out will be accomplished by a MZI, forming whether a symmetrical or an asymmetrical read-out system. The analysis is directed on obtaining an expression for the sensitivity and on calculating that airgap value which will deliver the highest sensitivity. The

obtained relationships are evaluated and finally the decision is made to focus in this demonstrator on read-out based on deflection caused changes of the attenuation of the probing guided mode. Based on the afore mentioned evaluation the structural parameters of the IO read out system are defined in Section 6.4. Finally the main results of this section are summarised.

In Section 6.5 potential structures of the MOEMS gyro demonstrator device are discussed and one of them is selected for realisation and finally defined.

Next, in Section 6.6, the fabrication process of the optical read-out system is presented and the produced structures are characterised as to their geometrical and optical properties. The bonding process is described. Unfortunately as a result of irremovable contamination on the external bond surface of the gyro system containing MEMS wafer, it appeared impossible to bond the MEMS and IO wafer together. It was decided to continue the research on the attenuation based read out method now mimicking the gyro wafer by other MEMS structures: by a wafer containing an electrostatically driven two-sided clamped membrane or by driving, in a controlled way, a silicon plate into the evanescent field region of the probing mode.

Section 6.7 describes the design, fabrication and some aspects of the characterisation of the membrane containing MEMS wafer. After bonding the MEMS and IO wafer together two series of experiments have been performed on the obtained MOEMS. In these series the optical response (change of transmission of the probing guided mode) has been measured as a function of the value of the voltage which has been applied between the membrane and an electrode on the IO wafer. This voltage delivers the electrostatically obtained deflection of the membrane. Simultaneous measurement of changes of the reflection angle of a laser beam incident on the centre of the membrane gave additional information about the deformation of the membrane. The experimental results are discussed and conclusions are drawn about.

In Section 6.8 similar experiments are described now using the system in which a silicon plate attached to a piezo-electric actuator is driven into the evanescent field of the probing mode. The experimental results are discussed and several conclusions are drawn.

In the final Section 6.10, the obtained results are summarised and some conclusions about the potential of the attenuation based readout method are presented.

6.2 MEMS gyroscopes

The big majority of the MEMS gyroscopes are vibratory gyroscopes. Their operation is based on a rotation induced transfer of energy between two vibration modes of a structure due to Coriolis acceleration: an apparent acceleration that arises in a rotating reference frame and is proportional to the rate of rotation.

The basic structure of the micromachined gyroscope, is schematically given in Figure 6.1.

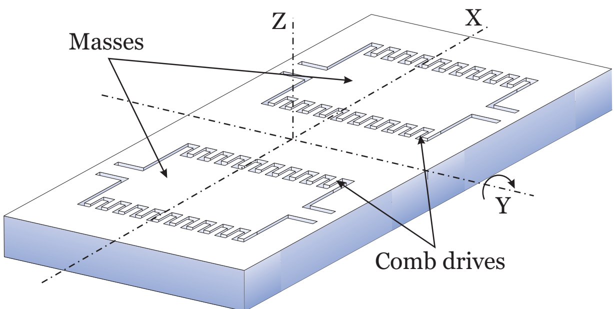

Figure 6.1: Schematic representation of a vibratory MEMS gyroscope

Two identical free-standing silicon masses attached to a Si-wafer frame by hinges are vibrating in anti-phase along the x-direction of a rotating reference frame, that is, the x-axis is defined with respect to the rotating MEMS. The vibration is generated electrostatically using comb drives. The rotation axis of the MEMS is the twofold symmetry axis in between the vibrating masses and is defined as the y-axis. So the system is of the type generally used in textbooks [Kro54] for introducing the concept of Coriolis forces: a body moving on a rotating disc along a line perpendicular to and through the rotation axis. In such a system a Coriolis force is generated, which in the corresponding polar coordinate system can be given as $F_\varphi = -2m(dr/dt)(d\varphi/dt)$. Starting from this formula, it can be shown that at an electrostatically generated vibration along the x-direction, a rotation around the y-axis generates a vibration along the z-direction, where the amplitude of the latter vibration is proportional to the rotation speed. The amplitude is at maximum if the resonance frequencies of the vibrations along the x- and z-direction are identical [GBKN92]. This explains the second desire of Thales-Av: as a consequence of imperfectness of the applied technology, identical resonance frequencies, giving the largest sensitivity, can be obtained only by a subsequent trimming of the obtained plate systems during the production process.

Because the comb drives let both masses vibrate in anti-phase along the x-direction, the rotation forces them to vibrate also in anti-phase along the z-direction. So at a first look the read out problem seems to be very similar to that of the moving mirror. However, the order of magnitude of the deflections to be measured is completely different in both MEMS systems: micrometres in the mirror system and nanometres in the gyro system. This means that, in contrast to the mirror demonstrator, no special measures have to be taken to maintain a free movement of the masses in the MOEMS and that all optical effects of the movements can be approximated as being linear to the displacement. Also, the required spatial resolution will be of a different order of magnitude. While in good approximation in the rotating mirror system, in most angular positions the effect of the deflection of the part removing from the IO system on the properties of the probing mode could be neglected, here the deflections of both parts have to be taken into account thoroughly. In this chapter the focus will be on maximising the sensitivity often also called the scale factor.

The Thales MEMS gyro

The Thales-Av gyroscope is manufactured starting from a SOI (silicon-on-insulator) wafer using sacrificial layer etching. To afford efficient electrostatic driving by comb-drives, the top-layer consists of doped silicon for enlarging its conductivity.

The following data, as have been given by Thales-Av, are considered to be relevant for the design:

- The object which is driven into the evanescent field is a silicon plate with a thickness not given to us;
- The lateral dimensions of each of the vibrating (approximately rectangular) silicon masses are 3800 µm (parallel to the y-axis) and 1300 µm perpendicular to that axis;
- the resonance frequency under vacuum conditions is in the range of 8-15kHz;
- Under operation conditions, as foreseen by Thales-Av, the amplitude of the vibration along the z-direction is in the order of magnitude of 1 nm;
- Without rotation of the complete device, the oscillating masses are rigid and do not show any displacement along the z-direction, the direction which is perpendicular to the plane of the masses.

- For affording a short duration of the sacrificial etching process, before executing this process step, a square pattern of square $14 \times 14\,\mu m^2$ holes has been applied in the Si layer at the location of the vibrating masses with a $42\,\mu m$ distance between the centres of two adjacent holes.

- Details regarding the precise shape of the plate and the hinges, and their exact way of vibration are confidential and cannot be presented here.

Requirements to the readout of the gyro system

For comparison with capacitive read-out measurements the optical readout should meet the following performance requirements:

- the demonstrator operates under vacuum conditions, the required pressure was not given to us;

- the required accuracy in measuring the resonance frequency should be better than 1 Hz;

- as a future desire to the complete system Thales-Av stated that the displacement equivalent noise of this system should be better than $10^{-3}\,\text{Å}/\sqrt{\text{Hz}}$. Because this noise depends on details of MEMS system itself, the optical read-out system and the electronics it was decided to focus in this stage of the research on maximising the scale factor, expressed in the unit $\text{V}/(°/\text{s})$, assuming that the final output signal would be given as an electrical voltage.

- for the same reason in this stage of the research no requirements have been given with respect to other performance aspects [YAN98] such as the resolution (or alternatively the 'angle random walk'), the zero-rate output, full scale range, bias drift etc.

The fulfilling of the requirement to the resolution also depends on properties of the electronic detection system. Hence we intended to limit ourselves to determining the resolution of the z-movement starting from an electronic system with a given resolution of the input signal.

6.3 Analysis

General

As the maximum deflections of the Si masses are about 1 nm, that is, three orders of magnitude smaller than those in both other demonstrators we expect no problems in affording such a small measurement range, and contrary to that for the other demonstrators the analysis will focus on obtaining maximum sensitivity only. Three different sensing configurations (see Figure 6.2) are considered:

- a single straight waveguide (Figure 6.2(a)) in which the attenuation effects are exploited;
- a symmetrical MZI where both branches are monitoring a mass movement (Figure 6.2(b)), in which the refractive effects are utilised;
- an a-symmetrical MZI where only one branch is monitoring a mass movement (Figure 6.2(c)), also exploiting the refractive effects.

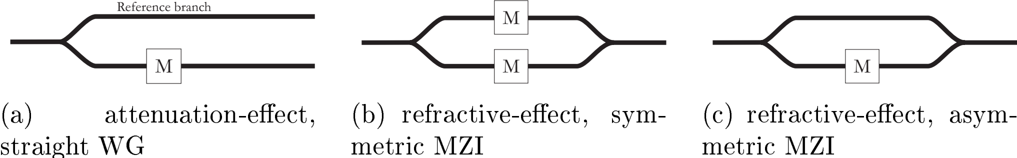

(a) attenuation-effect, straight WG (b) refractive-effect, symmetric MZI (c) refractive-effect, asymmetric MZI

Figure 6.2: Three considered sensing configurations ('M' indicates the lateral position of the vibrating plate)

For reasons of the relatively short time available for making the devices it had been decided that the MZI structures would not be provided with electro-optical modulators. All IO circuitry will be built up by using SiON technology, the layer stack containing Si_3N_4 as the core material and SiON ($n = 1.47$) or air as the cladding material in the passive and sensitive sections respectively. Two types of IO layer stacks will be considered: the 'common' ones having thermally oxidised SiO_2 as substrate layer and free-standing structures in which both the substrate and cladding layer consist of air.

For all configurations the sensitivity S is defined as

$$S = \frac{\partial(P_{\text{out}}/P_{\text{in}})}{\partial z}\Big|_{z=z_0} \tag{6.1}$$

with

$P_{\mathbf{out}}$ and $P_{\mathbf{in}}$ the output power and input power of the interaction section with interaction length L;

z_0 the distance between the masses and the upper face of the Si_3N_4 waveguides in absence of any rotation.

For maximising the sensitivity the following approach is used:

1. An expression for the transmission $T \equiv P_{\text{out}}/P_{\text{in}}$ of the system is derived, as a function of the distance between the silicon masses and the upper face of the Si_3N_4 waveguides, the 'airgap', z. This airgap will be expressed as $z = z_0 + \Delta z$ where Δz is the deflection of the plate with respect to z_0. The expression is derived for slab guides but is also a good approximation for ridge type waveguiding channels provided that their ridge height is small compared to the core layer thickness;
2. The sensitivity, $S = \partial T/\partial z\Big|_{z=z_0}$, is calculated;
3. The values of the free parameters are calculated for which maximum sensitivity is obtained. Taking into account that all materials have been defined already the only free parameters which influence the sensitivity are the airgap in absence of rotation, z_0, the thickness of the core layer, t ,the interaction length L (limited by the lateral dimensions of the plate) and the wavelength λ.

Attenuation based systems

For attenuation-based sensing configurations, the transmission can be expressed in terms of the imaginary part of the change of in the effective index as:

$$T = \frac{P_{\text{out}}}{P_{\text{in}}} = \exp\left[2N''_{\text{eff}} k_0 L\right] \tag{6.2}$$

Although the object which will be driven into the evanescent field is a plate with a finite thickness, we can approximate the object very well by a silicon plate having a semi-infinite thickness as has been shown in Section 4.3.

Hence for this MOEMS, the equation for the imaginary part of the effective index can be presented as, using Equation 2.13, as

$$N''_{\text{eff}} = \frac{r'' \sin(\varphi)}{k_0 W} \exp\left(-2k_0 z_0 \sqrt{N'^2_{\text{eff}} - 1}\right) \tag{6.3}$$

Where

$\varphi(t, \lambda)$ is the phase jump at reflection at the waveguide-air interface;

$r''(\theta, \lambda)$ is the imaginary part of the field reflection coefficient at the air-Si interface. From the Frenel reflection relations is follows that r'' is always smaller than 0. Here, $\theta(t, \lambda)$ is the angle of incidence of the rays at the plane of the air-Si interface, related to the unperturbed propagation of the zero-th order mode in the waveguide (that is, in absence of the silicon plate);

$k_0(\lambda)$ is the vacuum wavenumber, defined as $2\pi/\lambda$;

$W(\theta, \lambda, z_0, n_i)$ is the length of one zig-zag along the propagation direction including the Goose-Hänschen shift (GHS);

$N'_{\text{eff}}(\lambda, t, n_i)$ is the effective index of the unperturbed guided mode.

To simplify the notation, we introduce the following parameters:

$$c_1 = 2k_0(\lambda)\sqrt{N'_{\text{eff}}(\lambda, t, n_i)^2 - 1} \tag{6.4}$$

$$c_2 = 2\frac{r''(\theta, \lambda)\sin(\varphi(t, \lambda))L}{k_0(\lambda)W(\theta, \lambda, z_0, n_i)} \tag{6.5}$$

$$c_3 = c_2 e^{-c_1 z_0} \tag{6.6}$$

Parameter c_1 is always real and positive, n_{cl} is 1 (air-cladding). c_2 and c_3 are complex numbers and can be written as $c_i = c'_i + ic''_i$ for $i = 2, 3$.

From a large series of c''_2 calculations it appears, that within the range of the considered parameter window c''_2 is always negative. Using these parameters, and substituting Equation 6.3 into Equation 6.2, we can rewrite T as

$$T = \exp(2c''_3 \cdot e^{-c_1 z_0}) \tag{6.7}$$

The sensitivity S, expressed in terms of the c_i parameters is given by

$$S = \frac{\partial T}{\partial z}\bigg|_{z=z_0} = -2c_3'' \cdot c_1 \cdot e^{-2c_3''} \tag{6.8}$$

Maximum sensitivity is obtained by taking c_1 as large as possible, implying a small wavelength and a high t-value (being limited by the requirement that the waveguiding channel has to be monomodal), while c_3'' has to be equal to -0.5. The latter condition can be met by taking the proper value of z_0.

$$z_{0,\text{opt}} = \frac{-1}{c_1} \ln\left(\frac{-0.5}{c_2''}\right) \tag{6.9}$$

To elucidate the dependencies, S and the optimal value of z_0, $z_{0,\text{opt}}$, have been calculated for both waveguiding configurations as a function of t at the given wavelength of 1550 nm (see Figures 6.3 and 6.4). These results will be discussed later on in Section 6.3.

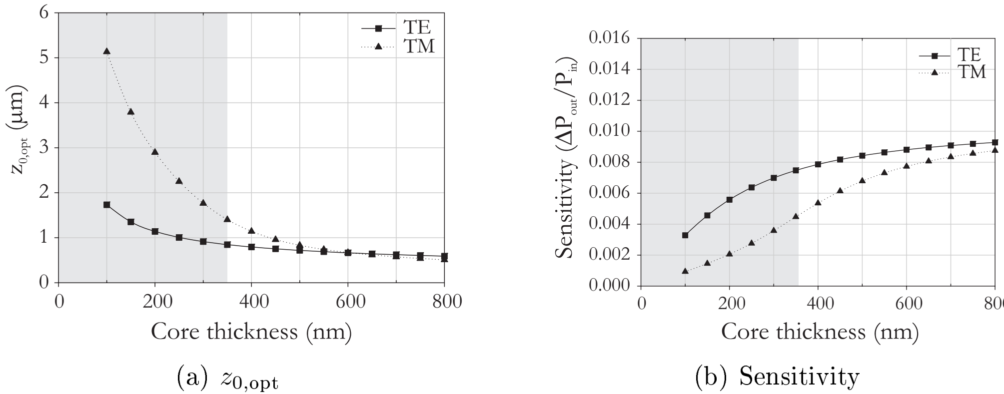

(a) $z_{0,\text{opt}}$ (b) Sensitivity

Figure 6.3: Sensitivity and optimised airgap using a free-standing waveguide for the attenuation based systems.

The symmetric MZI configuration

For the MZI sensing configuration, the changes of both the real and imaginary part of the effective index have to be taken into account. The general expression for the transmission T can be written as

$$T = \frac{1}{4}a_1^2 + \frac{1}{4}a_2^2 + \frac{1}{2}a_1 a_2 \cos(\varphi_1 - \varphi_2 + \theta) \tag{6.10}$$

Where

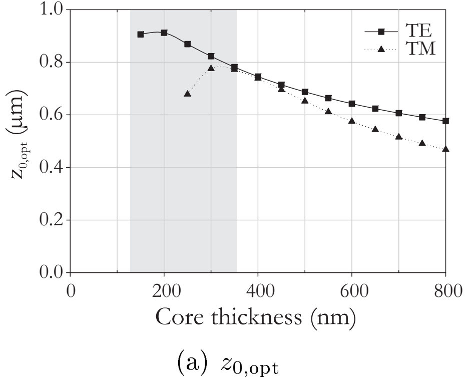

(a) $z_{0,\mathrm{opt}}$

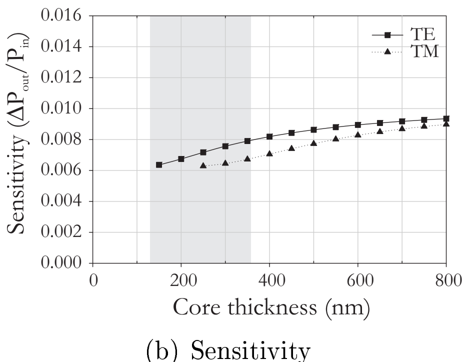

(b) Sensitivity

Figure 6.4: Sensitivity and optimised airgap using a 'common' type waveguide for the attenuation based systems.

a_i represents the ratio of the relevant electrical field components of the mode at the end and at the beginning of branch i;

φ_i is phase shift in branch i with respect to the state $z = \infty$;

θ is the additional (constant) phase difference at the outputs of the two branches, in the state $z = \infty$.

Note, that all remaining three free parameters determine the values of both the a_i and φ_i. Both gyro masses move in opposite direction with identical values of $|\Delta z|$.

Using the previously introduced variables c_1, c_2, and c_3 we can write a_i and φ_i as

$$a_1 = \exp(c_3'' e^{c_1 \Delta z}) \tag{6.11}$$

$$a_2 = \exp(c_3'' e^{-c_1 \Delta z}) \tag{6.12}$$

$$\varphi_1 = c_3' e^{-c_1 \Delta z} \tag{6.13}$$

$$\varphi_2 = c_3' e^{c_1 \Delta z} \tag{6.14}$$

The expression for T then becomes

$$\begin{aligned} T = &\frac{1}{4}\exp(2c_2'' \cdot e^{-c_1 \Delta z}) + \frac{1}{4}\exp(2c_2'' \cdot e^{c_1 \Delta z}) \\ &+ \frac{1}{2}\exp[c_3'' \cdot (e^{c_1 \Delta z} + e^{-c_1 \Delta z})] \cos(c_3'' \cdot e^{-c_1 \Delta z} - c_3'' \cdot e^{c_1 \Delta z} + \theta) \end{aligned} \tag{6.15}$$

Differentiation with respect to z yields S:

$$S = \frac{\partial T}{\partial z}\bigg|_{z=z_0} = c_1 \cdot c_3' \cdot e^{2c_3''} \sin(\theta) \tag{6.16}$$

As the only complex number in c_3 is $r_{cl,gm}$, the c_3' and c_3'' relate to each other as

$$c_3' = c_3'' \frac{r'_{cl,gm}}{r''_{cl,gm}} \tag{6.17}$$

Substituting Equation 6.17 in Equation 6.16 yields

$$S = \frac{\partial T}{\partial t}\bigg|_{t=0} = c_1 \cdot c_3'' \frac{r'_{cl,gm}}{r''_{cl,gm}} e^{2c_3''} \sin(\theta) \tag{6.18}$$

Then, maximising S requires $\theta = \pi/2$ and, for the appropriate airgap

$$z_{0,\text{opt}} = \frac{1}{c_1} \ln\left(\frac{0.5}{c_2''}\right) \tag{6.19}$$

S and the optimal value of z_0, $z_{0,\text{opt}}$, have been calculated for both waveguiding configurations as a function of t (the thickness of the core layer) at the given wavelength of 1550 nm (see Figures 6.5 and 6.6). These results will be discussed later on in Section 6.3.

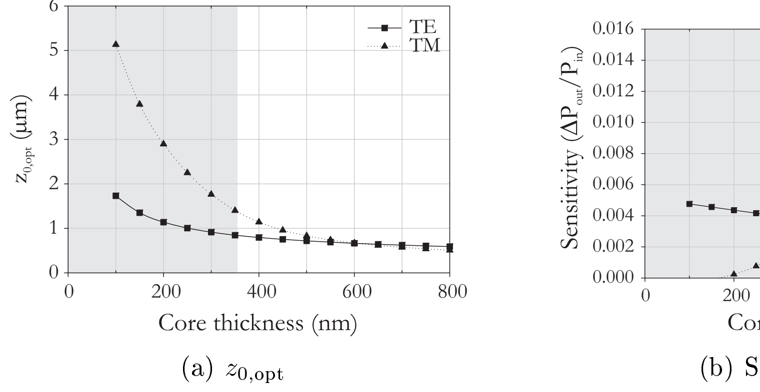

(a) $z_{0,\text{opt}}$ (b) Sensitivity

Figure 6.5: Sensitivity and optimised airgap using a free-standing waveguide for the symmetrical MZI based systems.

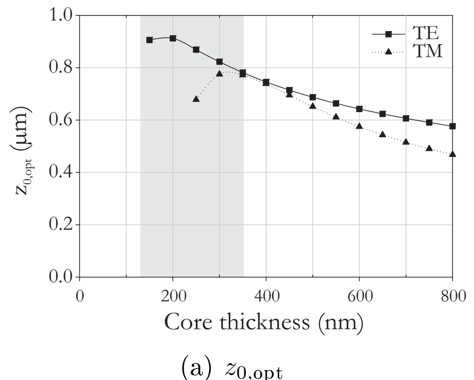

(a) $z_{0,\mathrm{opt}}$

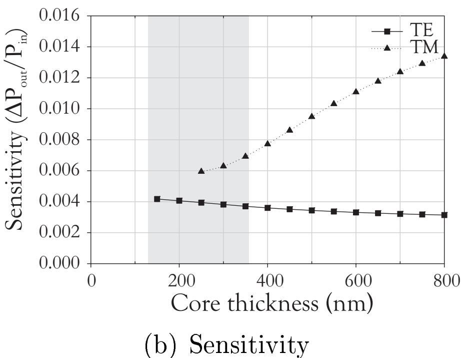

(b) Sensitivity

Figure 6.6: Sensitivity and optimised airgap using a 'common' type waveguide for the symmetrical MZI based systems.

The a-symmetric MZI configuration

Optimising the a-symmetric MZI sensing configuration proceeds in a way which is analogous to the optimisation procedure used for the symmetric one. Note however that in the asymmetric MZI configuration, the attenuation in one of the branches is independent of the MEMS system and assuming loss less waveguides, the corresponding a-value will be equal to 1. This will appear to be advantageous for obtaining high sensitivity. On the other hand in the a-symmetric configuration the value of $(\varphi_1 - \varphi_2)$ is about half of that value in the symmetric configuration. Detailed calculations have to be made for comparing the sensitivities of both MZI configurations. First, we present again the general transmission expression:

$$T = \frac{1}{4}a_1^2 + \frac{1}{4}a_2^2 + \frac{1}{2}a_1 a_2 \cos(\varphi_1 - \varphi_2 + \theta) \tag{6.20}$$

The only branch whose properties are modulated by the moving gyro plate is numbered as branch 2; so in the framework of our assumptions it is the a_1-coefficient which is equal to 1. It will appear useful to introduce an additional degree of freedom by assuming that φ_1 would be adjustable. This can be realised by introducing for example an electro-optical modulator on branch 1, which will be driven by a DC voltage. Expressing the attenuation and phase shifts in terms of the parameters c_1, c_2, and c_3 yields:

$$a_2 = \exp(c_3'' \cdot e^{-c_1 t}) \tag{6.21}$$
$$\varphi_2 = c_3' \cdot e^{-c_1 t} \tag{6.22}$$
$$a_1 = 1 \tag{6.23}$$
$$0 < \varphi_1 < 2\pi \tag{6.24}$$

Substituting Equations 6.21 through 6.24 in Equation 6.20 yields

$$T = \frac{1}{4}\exp(2c_3'' \cdot e^{-c_1 z}) + \frac{1}{4}a_1^2 + \frac{1}{2}\exp(c_3'' \cdot e^{-c_1 z})a_1 \cos(\theta - c_3' \cdot e^{-c_1 z}) \tag{6.25}$$

where φ_1 has been incorporated in θ. The sensitivity can be written as

$$S = -\frac{1}{2}c_1 c_3'' \left\{ e^{2c_3''} + a_1 e^{c_3''} \left[\frac{r'_{cl,gm}}{r''_{cl,gm}} \sin(\theta - c_3') + \cos(\theta - c_3') \right] \right\} \tag{6.26}$$

To maximise S, a_1 and c_1 should be chosen as large as possible ,hence the $a_1 = 1$ state naturally obtained in this configuration is the most favourable indeed. θ should be adjusted such that the sum of the sine and cosine terms are maximised. This latter condition yields for θ:

$$\theta = \arctan\left(\frac{r'_{cl,gm}}{r''_{cl,gm}}\right) + c_3' \tag{6.27}$$

Then S can be written as

$$S = -\frac{1}{2}c_1 c_3'' \left[e^{2c_3''} + e^{c_3''} \sqrt{1 + \left(\frac{r'_{cl,gm}}{r''_{cl,gm}}\right)^2} \right] \tag{6.28}$$
$$= -\frac{1}{2}c_1 c_3'' \left(e^{2c_3''} + e^{c_3''} R_r \right) \tag{6.29}$$

where the quantity R_r has been introduced:

$$R_r \equiv \sqrt{1 + \left(\frac{r'_{cl,gm}}{r''_{cl,gm}}\right)^2} \tag{6.30}$$

It follows that c_3'' should be chosen such that

$$(2c_3''+1)e^{2c_3''}+(R_r+R_r c_3'')e^{c_3''}=0 \tag{6.31}$$

From a series of calculations it appears that in the considered N_{eff} range 1.5 - 1.6 for TE modes, the ratio of the real and imaginary part of the reflection coefficient is in between 0.95 and 1.05. Approximating this ratio as being 1, for TE modes the sensitivity can be written as:

$$S \approx -\frac{1}{2}c_1 c_3''\left(e^{2c_3''}+e^{c_3''}\sqrt{2}\right) \tag{6.32}$$

To maximise S, c_3'' should be chosen to be approximately -0.76 giving $S_{\max}=0.33c_1$.

Again, S and the optimal value of z_0, $z_{0,\text{opt}}$, have been calculated for both waveguiding configurations as a function of t at the given wavelength of 1550 nm (see Figures 6.7 and 6.8). These results will be discussed later on in Section 6.3.

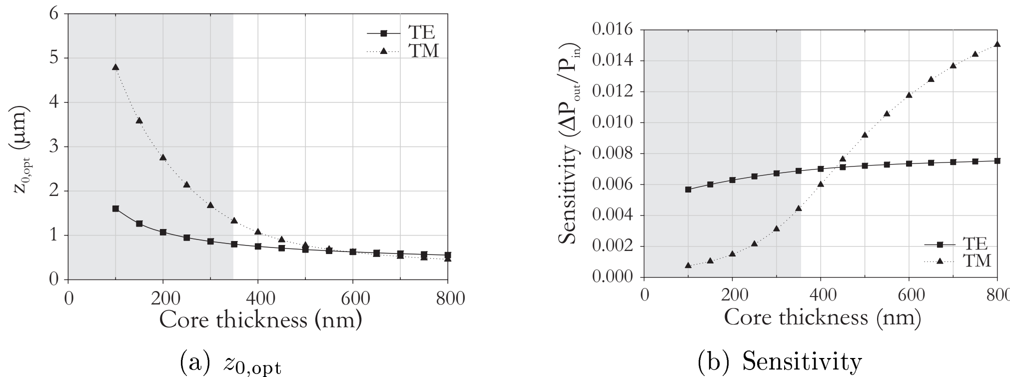

(a) $z_{0,\text{opt}}$

(b) Sensitivity

Figure 6.7: Sensitivity and optimised airgap using a free-standing waveguide for the a-symmetrical MZI based systems.

Discussion of the afore derived relations

The equations derived before are not very transparent. So we have decided to calculate for both types of waveguide configuration (the 'common' one and the free-standing one) for the wavelength of 1550 nm both the maximum sensitivity and the optimal value of z_0 as a function of the only remaining free parameter t, the thickness of the Si_3N_4 core layer both for the lowest

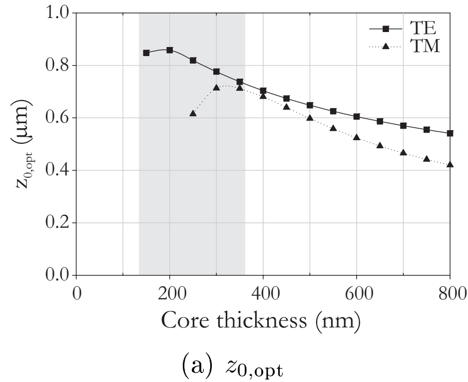

(a) $z_{0,\mathrm{opt}}$

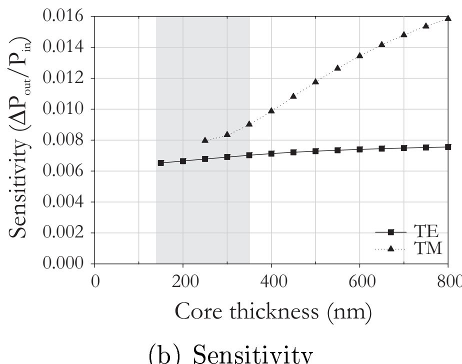

(b) Sensitivity

Figure 6.8: Sensitivity and optimised airgap using a 'common' type waveguide for the a-symmetrical MZI based systems.

order TE and TM mode. Here we have taken the interaction length L to be 3.8 mm, implying that the waveguide will be parallel to the rotation axis. The thickness t is limited however to a certain range, with a highest t-value given by the requirement that the waveguiding structure should be monomodal and (in case of the 'common' structure only) with a lowest value, the cut-off thickness.

Furthermore, for the a-symmetric MZI sensing configurations, the phase θ was set to the value that results in a maximum sensitivity (see Equation 6.27).

Before discussing these figures some boundary conditions originating from technological restrictions have to be introduced :

- Sticking of the silicon masses to the waveguiding structure has to be avoided. The chance on sticking is the smaller, the wider the airgap. Sticking may be prevented by providing the waveguiding structure with bumps, as has been described already in Section 4.5, of course with a bump height smaller than the desired z_0-value.

- the thickness of the LPCVD Si_3N_4 core layer should not exceed the technologically feasible thickness ($\sim$ 350 nm, above which the layer is likely to show cracking). In all graphs the applicable area is indicated by a grey window.

From the figures it can be concluded, that in the applicable thickness-ranges, the sensitivities are in between 0.002 nm^{-1} and 0.008 nm^{-1}. This implies, that the corresponding maximum changes of the output power are less than 1%. Taking into account the expected (about 1%) fluctuations

of the input power, it is clear that a reference channel is indispensable. This reference channel can be a passive one but alternatively, at attenuation based read-out systems, also a channel probing the other plate can be applied. The complete IO circuitry has to be constructed in such a way, that the output powers of sensing and reference channel are very close to each other in order to enable their efficient comparison using a matched photodiode pair and a high quality difference amplifier.

At first we compare the sensitivities of both types of waveguiding structures, the common one and the free-standing one.

The common type of waveguiding structures generally show similar sensitivities as the free-standing ones; largest sensitivity is obtained in the structure (TE mode, $t = 200\,\text{nm}$).

For all t-values the z_0 values are always larger in the free-standing waveguiding structures than in the common ones, but all of them are technologically acceptable. Hence considering the sensitivities and optimal air gap values there is no clear advantage of the free-standing waveguiding structures over the 'common' structures.

The technological complications related to making the free-standing waveguides are well known (see Chapter 3). However, application of the common structures is not straightforward either. In the passive sections of the IO circuitry the mode is not allowed to experience the presence of the MEMS and this can be realised by applying a SiON ($n = 1.47$) cladding layer with a thickness over 3 µm. In a flat layer stack this should imply that the value of z_0 should be equal to the cladding layer thickness, and this 3 µm is a value much larger than the optimal value of z_0. So whether one has to accept worse performance or, if the optimal z_0 value is aimed at, one has to introduce additional technological steps, for example, locally etching down the thickness of the Si wafer or of the SiO_2 buffer layer. We have decided to chose the last option resulting into a layer structure as given in Figure 6.9.

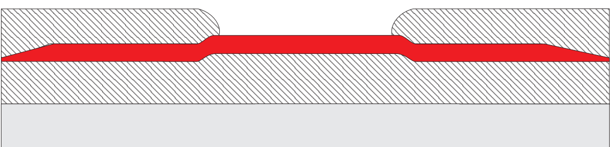

Figure 6.9: Illustration of the chosen layer structure showing the locally etched buffer layer which results in a locally (in the sensing region) elevated core layer.

Considering the sensitivities of the various read-out structures of the

'common' waveguide structure, we can conclude, that for the TE mode the attenuation based read-out is most advantageous, showing sensitivities about 0.008. If utilising a TM mode, the asymmetrical MZI enables a somewhat larger sensitivity. Nevertheless, we decided to focus on the attenuation read-out using a TE mode. And this for two reasons. First one: small TM power can be removed efficiently, while the TE mode is nearly not attenuated, by adjusting the thickness of the buffer layer guaranteeing TE_{00} propagation of the light. Second one: we were very interested to investigate also the potential of attenuation based readout methods.

We have also calculated the performance of all these systems for another wavelength, 632.8 nm. Results (not shown here) were similar to the 1550 nm results and taking into account the boundary conditions they lead to the same decision: TE mode, attenuation-based readout and the 'common' waveguiding structure. Because at a lower wavelength the z_0-values are much smaller and the performance would be more vulnerable to sticking and to technological inaccuracies we have decided to apply 1550 nm wavelength light.

6.4 The structural parameters of the IO structure

Discussion of the structural parameters

the core layer thickness Figure 6.4(b) shows that the sensitivity of the structure does not depend very strongly on the core thickness. We have adopted a core layer thickness of 200 nm, for which structure maximum sensitivity is obtained at an air gap $z_0 = 0.9\,\mu m$. For investigating which deviations of the optimal z_0 value are allowed, (using as a criterion that the sensitivity is lowered 10% at maximum) we have calculated the sensitivity of the aimed system ('common' layer stack, $t = 200$ nm, wavelength 1550 nm) as a function of z_0 utilising Equations 6.8, see Figure 6.10).

From this figure it can be concluded, that the sensitivity is strongly dependent on the z_0-value and that for obeying our criterion the z_0-value is allowed to vary in between 850 nm and 980 nm only. The value of the air gap is controlled by the thickness difference of the SiO_2 buffer layer at both the thinned and non-thinned sections as well as by the thickness of the SiON cladding layer. Hence all these thicknesses have to be controlled well during the realisation.

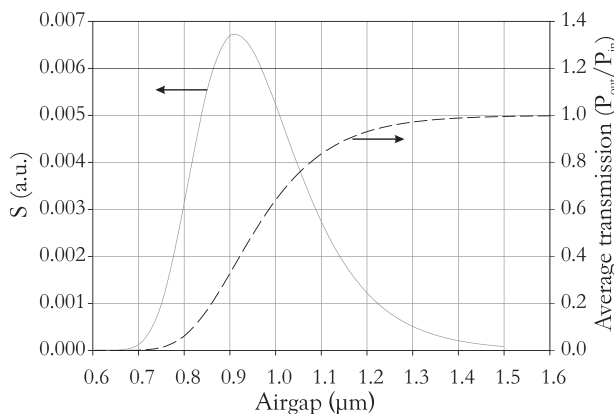

Figure 6.10: Dependence of the sensitivity and average transmission (transmission at z_0) on the airgap

The cladding layer thickness For reducing leakage of the light from the passive waveguide sections to the gyro chip, a SiON ($n = 1.47$) cladding layer has to be applied at those sections in which the MEMS and the IO wafer are bonded together. A TE_0 mode leakage loss of 0.01 dB/ cm, is calculated to exist if the thickness of the SiON cladding layer would be equal to 3 μm.

The buffer layer thicknesses For attenuating TM light by leakage to the IO Si wafer while keeping the attenuation of the TE mode lower than 0.01 dB/ cm the thickness of the SiO_2 buffer layer at the thinned sections has to be 3.0 μm. To have $z_0 = 0.9$ μm, the thickness of the SiO_2 buffer layer at the sensing region has to be 2.1 μm larger than at the thinned sections, hence the thickness of the SiO_2 on the thermally oxidised wafer has to be at least 5.1 μm. We have chosen to start from commercially available thermally oxidised wafers with a 8 μm thick SiO_2 layer (a standard thickness)

The taper sections A loss free modal propagation in a section in which the SiO_2 layer thickness is reduced over 2.1 μm can be obtained by implementing this reduction section as an adiabatic taper in the SiO_2 layer. In our technology the smallest taper angle that can be obtained in a SiO_2 layer is about 3°. This implies a taper length of 40 μm. A question to be answered is at which position the cladding layer has to stop. In the one extreme, in which the cladding stops at the passive thinned section, the modal field in the tapered section should extend into the Si of the gyro and interpretation of the attenuation

data would become dependent on the precise shape of the taper. If the cladding layer should stop somewhere in the sensing region this dependence is ruled out, but now the SiON cladding layer is locally elevated which would prevent a wafer bonding over large areas. Although these elevations might make the CMP process which is needed for lowering the surface roughness of the SiON cladding (as required for bonding) less controlled, preliminary experiments showed, that in between the elevations a smooth surface is obtained being well parallel to the other boundary planes of the layer stack. The problems related to both options can be avoided by applying additional holes in the MEMS wafer. Finally we have chosen for the second option in which these additional holes are positioned above the elevated sections. A longitudinal cross section of the waveguiding structure is presented in Figure 6.13(a).

Waveguide cross-section As a consequence of the fabrication process, the vibrating masses of the MEMS gyro contain a square network of holes (dimensions $14 \times 14\,\mu m^2$, separation $28\,\mu m$) across the entire surface. If the modal field of the guided optical mode would not be negligible at the position of these holes, the lateral plate vibration itself would influence the modal attenuation. For minimising this influence the centre of the waveguiding channel has to be positioned just below the centre line in between two rows of holes at the rest position of the plate. For further minimising the influence of the holes the lateral confinement of the modal field has to be maximised while maintaining the single mode character of the waveguide channel. Taking the common ridge type channels we have to be aware of two technological limitations.

Ridge width The ridge width has to be larger than $3\,\mu m$ because of available mask writing tools

Ridge height The ridge height has to be smaller than approximately 10 nm for avoiding underetching during the wet-chemical BHF etching process which will be used for applying the ridges.

Using the effective index method (EIM) it can be easily derived, that such a ridge waveguide can support one TE mode only for width smaller than $w_{\max}$, which quantity is related to the ridge height r_h by

$$w_{\max} = \frac{\pi}{k_0\sqrt{N_{\text{eff}}(t)^2 - N_{\text{eff}}(t-r_h)^2}} \tag{6.33}$$

This relation is graphically represented in Figure 6.11 for $t = 200\,\mathrm{nm}$.

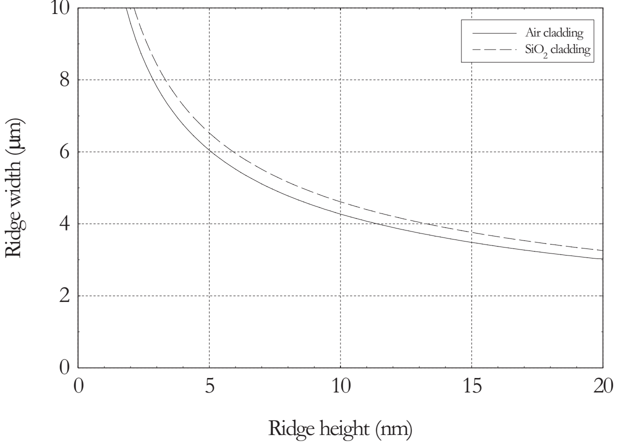

Figure 6.11: Plot showing the usable range of ridge dimensions

To obtain an estimate for the effect of a hole in the gyro mass on the optical mode, the power confined by such a hole has been calculated as a function of the difference, x, of the lateral positions of the centre of the hole and the centre line of the waveguiding channel ($z_0 = 0.9\,\mu\mathrm{m}$). The x-dependence of a normalised power (normalised with respect to the power at $x = 0$) has been presented in Figure 6.12 for several monomodal ridge-type channel structures.

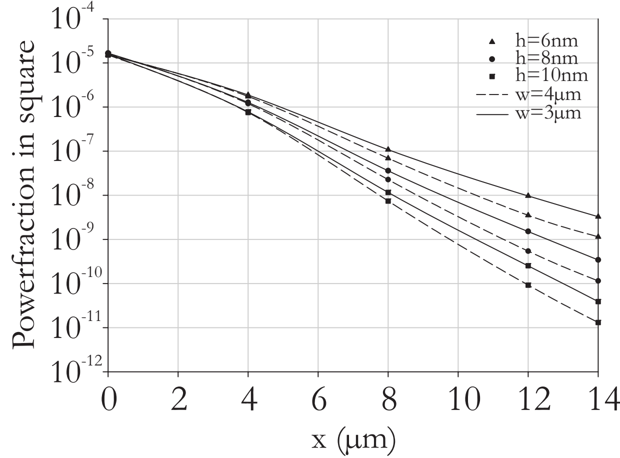

Figure 6.12: Normalised power confined within a gyro hole as a function of the distance x for several sets of waveguide parameters(h: ridge height, w: ridge width

For a waveguide with $w = 4\,\mu\text{m}$ and $r_h = 10\,\text{nm}$, this normalised power is equal to 10^{-6} only, at a distance $x = 14\,\mu\text{m}$. Therefore it is estimated that it is not necessary to apply ridge heights over 10 nm.

Bends will be applied in the ridge waveguide in order to eliminate slab light at the output. Apart from the sensing structure also several test structures such as straight channels optically isolated from the MEMS will be implemented in the IO wafer. V-grooves and saw cuts will be applied for enabling an effective fibre to chip coupling.

Summary

In summary, the following choices have been made and the following parameter values will be taken:

- the attenuation based read out method will be applied;
- the waveguiding channel is monomodal and the probing mode is the TE_{00} mode;
- the centre line of waveguiding channel will be positioned just below the centre line (along the direction parallel to the rotation axis) of one of the vibrating masses of the MEMS;
- monochromatic light with a wavelength of 1550 nm will used;
- s common layer stack consisting of a SiO_2 buffer layer,(n=1.45) a Si_3N_4 core layer ($n = 1.98$) and a SiON ($n = 1.47$) cladding layer will be the starting point for the IO system;
- standard, commercially available Si wafers with a 100 mm diameter which have been provided with a $8\,\mu\text{m}$ thick thermally grown SiO_2 layer, will be used as substrate;
- The values of the geometrical parameters of the IO structure are given in Figures 6.13(a) 6.13(c)(transverse cross section) on page 104;
- the optimum distance between the upper plane of the afore defined waveguide and gyro masses giving the largest sensitivity, is equal to 900 nm.

6.5 The structure of the demonstrator device

Electrodes and bumps

As mentioned already in Section 6.2, in common MEMS gyroscopes the detection mode of the vibrating masses is excited by energy transfer from an excitation mode as a result of a rotation of the MEMS system. Driving these masses by Coriolis forces should require a very complicated experimental set up. The principal aim however is at showing the feasibility of the optical methods for read out of very small deflections of the Si masses along the z-direction. It was decided to generate these small displacements on another way: the driving forces should be electrostatic. These forces should be generated by applying a voltage between the masses and electrodes which should be applied on top of the IO waveguiding structure. In order to prevent sticking of the gyro masses to the optical chip bumps will be implemented on the surface of the optical chip, on both sides of the ridge waveguide. Two actuation electrodes will be applied, each at one side of the channel guide delivering a symmetrical structure in order to avoid warping of the masses. A top-view is presented in Figure 6.13(b).

These electrodes will be built as a bi-layer of metals; 50 nm of chromium (Cr) (for having a good adhesion) and 200 nm of gold (Au), bringing the total thickness of the electrode to 250 nm. To connect the electrodes to peripheral equipment electrical leads have to be supplied to the edge of the wafer for easy connection using wire bonds. These leads will be placed in trenches that will be etched in the cladding layer for electrical isolation of the electrodes from the MEMS wafer. Also, if they were placed on top of the cladding layer, they would hamper the bonding process. Bumps have to be applied to reduce the effective contact surface between plate and IO wafer in that way preventing sticking. These bumps have to be positioned underneath the entire surface of the gyro masses. As such, they will overlap with the actuation electrodes. As to the bumps the following can be said:

- the dimensions of the bumps are in the same order as those used in previous projects [Vel98]: that is, bump height 350 nm and bump area $10 \times 10\,\mu m^2$.
- the bumps are positioned in such a way that at large displacements (as can be caused by mechanical shocks) they would support both the gyro masses and the plate hinges.
- to prevent fitting of the bumps into the holes, the spacing of the bumps has to be unequal to a multiple of the spacing of the holes in

the gyro masses.

Electrical and optical connections

Since the wafers need to be bonded face-to-face, extra measures had to be taken in order to access the electrical contacts and the optical channels that are located on the front side of the optical wafer. The decision was made to saw the MEMS wafers into strips before bonding such a strip to the optical wafer; each strip contains a row of nine gyro's all having their rotation axis perpendicular to the sawing planes. In this way the necessary fiber-to chip connections can be made easily, and there is no need to etch large holes in the MEMS wafer as had to be done in the mirror demonstrator. The electrical contacting of the MEMS masses will be realised from the backside of the MEMS wafer. As a result of discussions with Thales-Av, it has been decided to use direct wafer bonding to bond the MEMS wafer (Si surface) to the IO wafer (SiO_2 surface) although for direct bonding the requirements to the surface roughness and the contamination level of the wafers are quite severe [GAG+97]).

Required modifications of the MEMS

Although we intended to maintain the integrity of the MEMS as much as possible, various changes had to be applied in the MEMS for enabling the integration with the IO chip:

- instead of a complete wafer, only a single strip, containing nine gyros will be bonded to the optical chip;
- electrical contacts will be made between the frame (the silicon wafer) of the gyro chip and the masses;
- some trenches will be etched in the SOI wafer for enabling the evacuation of the cavity formed by the gyro and optical chips. Low pressure inside this cavity is needed to avoid squeezing, which would result into a degradation of the quality factor and a shift of the resonance frequencies;
- alignment marks will be placed on the MEMS chip for enabling the correct relative positioning of the wafer and the strip.

The complete MOEMS

An impression of the complete MOEMS structure is given in Figure 6.13.

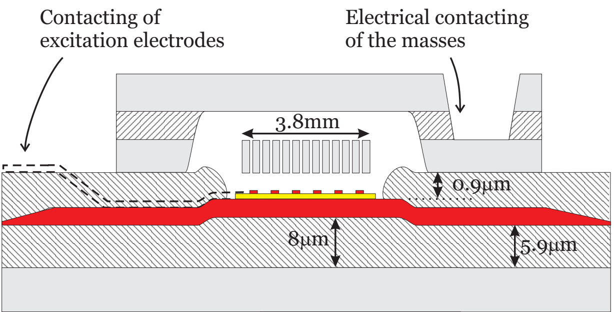

(a) Cross-section parallel to the waveguide

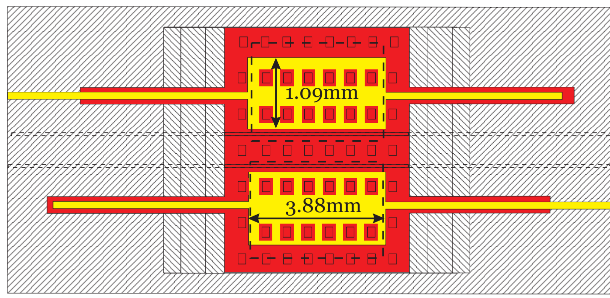

(b) top view

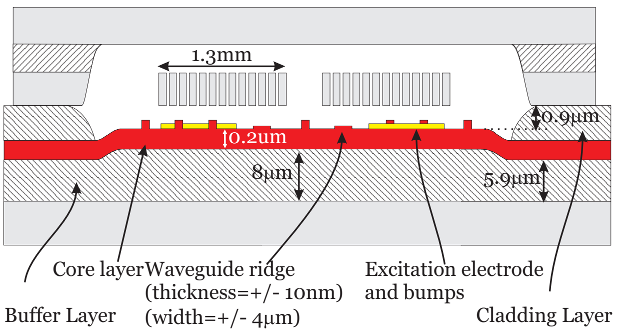

(c) Cross-section in the sensing area, perpendicular to the waveguide

Figure 6.13: Schematic structure of the complete demonstrator

6.6 Fabrication process

The optical wafer

The fabrication process of the optical chip for the gyro demonstrator is briefly described below; a more thorough process list is given in Appendix E. Starting point is a 100 mm diameter ⟨100⟩ silicon wafer which is provided with an 8 µm thick thermally grown SiO_2 buffer layer.

1. The precise crystal orientation is determined using a combination of BHF and KOH etch steps.
2. The alignment marks are etched in the buffer layer using a BHF process.
3. The SiO_2 layer is locally etched down by two subsequent BHF etch steps using a double-masking technique while etched and unetched regions are connected by adiabatic tapering.
4. Bumps are applied in the buffer layer.
5. Subsequently, the Si_3N_4 core layer is grown in a LPCVD process
6. The fibre-to-chip coupling tapers are etched by a BHF process.
7. The ridge waveguides and the openings, which will define the V-grooves are etched in theSi_3N_4
8. Using a PECVD process, the SiO_2 cladding layer is deposited;
9. The openings for the V-grooves are etched in the cladding and buffer layer;
10. The V-grooves are etched in the Si using a KOH etch process;
11. The wafer is polished using a CMP process in order to create a smooth bonding plane;
12. The sensing windows are opened and the trenches for the electrical leads are made by etching a taper in the cladding layer using two subsequent BHF etch steps in a double-masking technique;
13. The electrodes are applied by the sputtering of a Cr and Au layer followed by a lift-off process;
14. Finally, the in-couple plane is sawed in, at the position of the end of the V-grooves.

During processing an additional problem was met: if plain electrodes were applied the metal layer should also be present on top of the bumps, leading to irregularities in the electric field. Hence the bumps had to be freed from metals as was expected to be realisable in the same lift-off process used for defining the contours of the electrodes. However not all bumps appeared to be freed from metals. This problem was solved by applying an extra lithography step directed to etching off the metals around the bumps in an additional etching step.

Characterisation of the IO-device geometry

Prior to bonding several relevant dimensions of the IO structure have been measured; results are given in Table 6.1

Table 6.1: Comparison of the realised geometry of the IO device with the designed values

	Design		Realised	
	Optimum	Margin allowed	Average	Variation[a]
Ridge height	10 nm	±1 nm	10.5 nm	±0.5 nm
core layer thickness (incl. ridge)	210 nm	±3 nm	211 nm	±2 nm
Core thickness after nitride taper (incl. ridge)	50 nm	±5 nm	49 nm	±2 nm
Electrode thickness	250 nm	-0 nm, +50 nm	270 nm	±10 nm
Bump height	350 nm	-0 nm, +50 nm	390 nm	±5 nm
Wafer curvature	<10 µm	-	±6 µm	-
Buffer taper	2.1 µm	-0.1 µm, +0.2 µm	2.2 µm	±50 nm
Airgap	900 nm	±100 nm	850 nm	±50 nm

[a] Wafer-to-wafer and intra wafer variations

The thickness of the core layer and the ridge height have been determined by ellipsometry (Plasmos SD 2002 ellipsometer), the other dimensions by using a stylus profiler (Veeco Dektak 8). The most relevant parameter, the airgap shows both a wafer to wafer and an intra wafer non-uniformity, the first one being larger than the second one. The airgap values as have been measured for three different wafers are indicated in Figure 6.14 in that way simultaneously showing the influence of this spread on the sensitivity.

Stylus scans show, that the stress induced curvatures of the IO wafers are very small: about 5 µm height difference between the centre and the edges of the wafer. Such a wafer curvature is expected not to hamper wafer bonding [GAG+97]. The result of such a stylus scan is shown in Figure 6.15 where the path of the scan is indicated in the microscope picture of the sensing region (Figure 6.16).

The wafer bonding

Bonding wafers together usually refers to complete circular wafers of a given diameter, for example, 100 mm. As such, wafer aligners and bonding tools are suitable only for those complete wafers. Therefore, bonding of a wafer

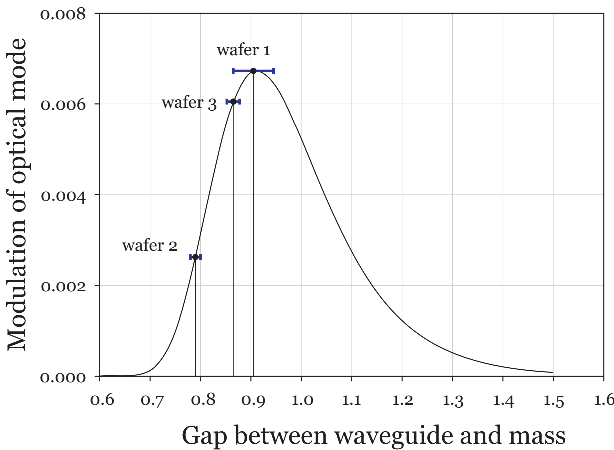

Figure 6.14: Spread of the realised airgap values and their influence on the sensitivity

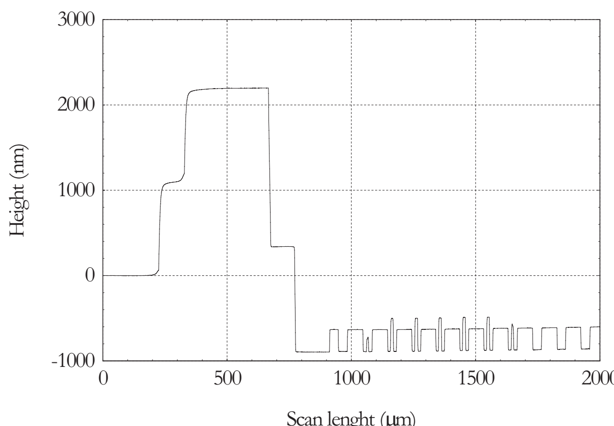

Figure 6.15: Stylus profiler scan showing the sensing window, electrodes and bumps.

strip, as has to be done here, is usually not possible. This problem has been solved by attaching the strip to a 100 mm carrier wafer by using an adhesive intermediate layer, for example, wax or photoresist, which by solving that material allows for easy removal of the carrier wafer after the bonding. This technique illustrated in Figure 6.17 and tests have shown its feasibility.

Several wafers containing gyros have been delivered by Thales-Av to MESA+. Bonding planes of all wafers appeared to be strongly contaminated: a first batch showed a bonding plane on which whisker- type Si particles were present, which are expected to be generated by an imperfect dry etching process. In a second batch these whiskers were absent but

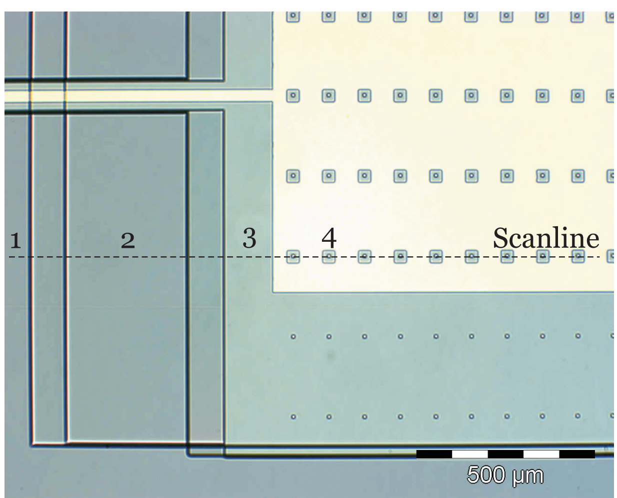

Figure 6.16: Microscope picture of the sensing region where the stylus scan path is indicated by the dashed line.

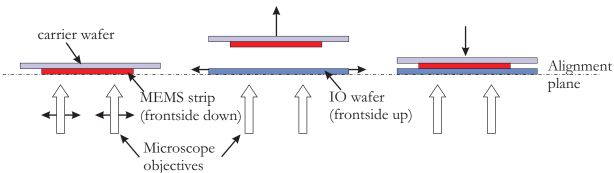

Figure 6.17: Illustration of the strip-bonding using a carrier wafer

microscopic observation showed contamination with (clusters of) small particles. Thales-Av had no notion of their nature and origin. It appeared that these wafers could not be bonded to the IO wafers. We ascribe this to the presence of these contaminations. Microscope photographs of the contamination is shown in Figure 6.18.

In any case, the origin of the non-bondablity is not the IO wafer, because the latter appeared to be well bondable to bare Si wafers. None of the standard cleaning methods available in the clean room lab of MESA+ appeared to be capable to remove these contaminations.

It has been considered to align both wafers in the mask aligner, to press them together in this aligner and to fix this state by providing the side walls of the wafers with some droplets of glue. However because in such systems the distance between the vibrating masses of the gyro and the upper plane of the sensing section of the IO wafer would be undefined as a consequence of the unknown thickness of the contamination, this approach has been abandoned. Because Thales-Av was not able to deliver non contaminated

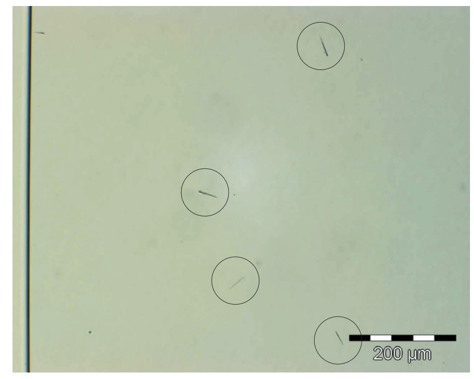

(a) 'grass' contamination (indicated by circles) of gyro wafers

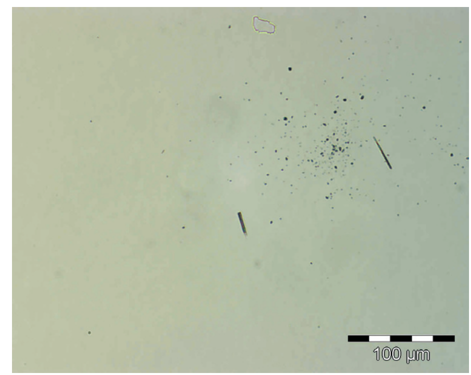

(b) Particle contamination of gyro wafers

Figure 6.18: Microscope photographs of the different types of contamination present on the Thales-Av gyro wafers

gyro-wafers, because the contaminations could not be removed and because these contaminations prevented the wafer to wafer bonding we had to conclude that we had to end the investigations on the gyro-demonstrator itself.

However, testing of the functionality of the IO device can be done in other ways. First way , we have adopted, is to replace the gyro-wafer by another simpler MEMS which is able to mimic the movements of the gyro wafer. We decided to substitute the gyro devices by MEMS containing thin Si membranes, which could be moved over small distances by electrostatic forces. In addition we decided to apply various free-standing waveguide channels for investigation of the potential of the attenuation method for measuring displacements over longer distances. Here Si masses which are connected to a piezo-electric actuator, should be driven into the evanescent field of the propagating modes. The latter method offers some more freedom in defining the air gap in between the IO wafer and the moving object.

6.7 MOEMS in which the MEMS is a Si wafer containing Si membranes

Schematic structure of the MOEMS

A schematic picture of the intended MOEMS is shown in Figure 6.19.

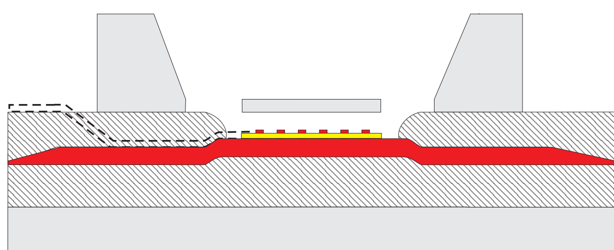

(a) Cross-section parallel to the waveguide

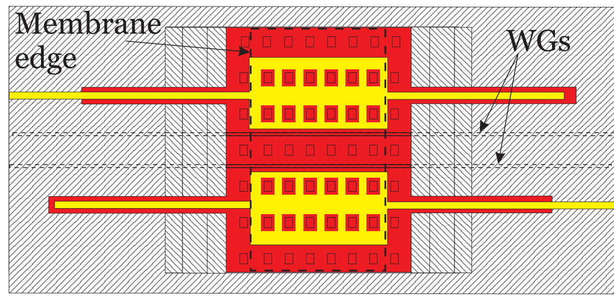

(b) top view

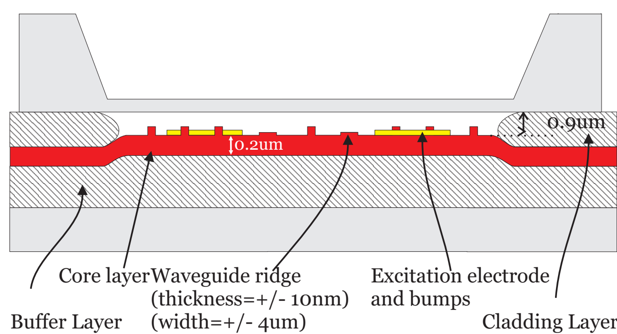

(c) Cross-section in the sensing area, perpendicular to the waveguide

Figure 6.19: Illustration of the MOEMS where the gyro chip is replaced by a wafer containing Si membranes

The design of the Si membranes

In order to have a homogeneous displacement of the membrane in the region just above the sensing waveguide, the membrane will be clamped on two sides only, resulting into a configuration as given in Figure 6.19.

In a perfect system this configuration avoids any position dependence of the distance between the centre line of the waveguide and the membrane. The openings at two sides of the membrane also reduce squeezing effects

which might occur during the movement of the membrane.

The effects of applying a (DC) voltage between the membrane and the driving electrodes depend on the geometry of the membrane and the position and area of the electrodes. Relevant for our objectives are the response on a DC voltage, V_{DC} and the fundamental resonance frequency, f_1. Hence we present here some formulas concerning these quantities and on base of these formulas we will decide about the geometrical parameters of the membrane.

As a result of the applied voltage an electrostatic force is created which is inversely proportional to the square of the spacing between the membrane and the electrodes. As a consequence the static deflection profile of the membrane has to be derived from a non-linear differential equation [TL94b, TL94a]. This non- linearity results from a positive feed back mechanism[1] and as a result the system becomes instable above a certain system dependent voltage (the pull-in voltage) and at a higher voltage the membrane will be pulled against the electrode.

For a homogenous, rectangular Si membrane that is clamped on two sides (clamped-clamped), driven by a rectangular electrode, while the overlap of the electrode surface and the membrane surface is larger than approximately 60%, the pull-in voltage $V_{\text{pull-in}}$ can be approximated by [Vel98, TL94b].

$$V_{\text{pull-in}} = \frac{1.22\pi^2}{L^2}\sqrt{\frac{E}{1-\nu^2}\frac{t^3d^3}{12\epsilon_0} + 0.0253\frac{NL^2d^3}{w_m\epsilon_0}} \tag{6.34}$$

where ϵ_0 is the dielectric constant in vacuum, $\nu = 0.271$ is Poisson's ratio, $E = 160\,\mathrm{GPa}$ is the Young's modulus of single crystalline silicon, d is the distance between the electrodes and the membrane, L is the length of the membrane and t its thickness, N is the axial load on the membrane and w_m is the width of the membrane.

An approximation for the deflection z around z_0 of the (centre of the) membrane, assuming attracting forces along the entire area of the membrane, is given by is given by Equation 6.35.

[1]This positive feed back can be understood as follows: An equilibrium state can be obtained only if the attractive electrostatic force is equal to a restoring force originating from the bending and the stiffness of the membrane. An increase of the driving voltage results in an increase of the attractive electrostatic force, leading to a decrease of the spacing between the membrane and the electrodes. This decrease causes an additional increase of the attractive force. At a certain voltage, the pull-in voltage, the restoring force is no longer able to compensate the attractive force, causing the spacing to go to zero.

$$z = \frac{3}{2}\frac{V^2\epsilon_0\left(\frac{L/2}{2}\right)^4}{d^2Et^3} \tag{6.35}$$

The fundamental resonance frequency of such a clamped-clamped membrane can be calculated to be [TEF91]

$$f_1 = \frac{\omega_1}{2\pi} = \frac{\alpha_1}{2\pi}\frac{h}{L^2}\sqrt{\frac{E}{1-\nu^2}\frac{1}{12\rho}} \tag{6.36}$$

Here $\alpha_1 = 4.730$, a constant depending on the mechanical resonant mode order and $\rho = 2330\,\mathrm{kg/\,m^3}$ is the density of silicon.

Taking $t = 13\,\mu\mathrm{m}$, $L = 3.8\,\mathrm{mm}$ and $d = 650\,\mathrm{nm}$ (z_0-value (900 nm) minus the electrode thickness (250 nm)) for the measurements well acceptable values are calculated for the pull-in voltage, 0.83 V and the resonance frequency 8.0 kHz.

Realisation of the MEMS

The MEMS structure essentially can be produced starting whether from a SOI wafer (the thickness of the membrane is given, local sacrificial etching can be used) or a bare Si wafer (KOH etching from the backside is required for making the membrane). We started with SOI wafers with a thickness of the Si layer being 340 nm which were available in the IOMS group; they were expected to offer flat Si membranes with uniform thickness. However, the membranes with a $3.8 \times 4\,\mathrm{mm}^2$ area broke during processing. Hence we decided to continue starting from bare homogeneous ⟨100⟩Si wafers taking the risk, that the etching would result into membranes with non-uniform thickness while the lower, etched end plane would not be smooth and parallel to the upper plane. The fabrication process of such membranes is briefly described below; a more detailed listing of the processing steps is given in Appendix F.

- The crystallographic orientation is determined;
- On the front side of the ⟨100⟩Si wafer, the membrane structures and alignment marks are lithographically defined and subsequently etched in a RIE process;
- A 40 nm thick LPCVD Si_3N_4 protection layer is grown;

- The Si_3N_4 layer on the backside of the wafer is locally etched off (RIE) in for producing the appropriate openings for the subsequent KOH etching process;
- The wafer is wet-chemically etched in a KOH solution to create the membrane;
- The remaining Si_3N_4 is stripped from both sides of the wafer using a RIE process;
- Finally, the wafer is diced into strips.

6.8 Characterisation of the MEMS

The membrane containing MOEMS

The optical wafer and the membrane strip are bonded together using the direct wafer bonding technique, which is described in Appendix A. Good bonding has been obtained.

The measurement setup

The setup used for determining the performance of the MOEMS is given in Figure 6.20.

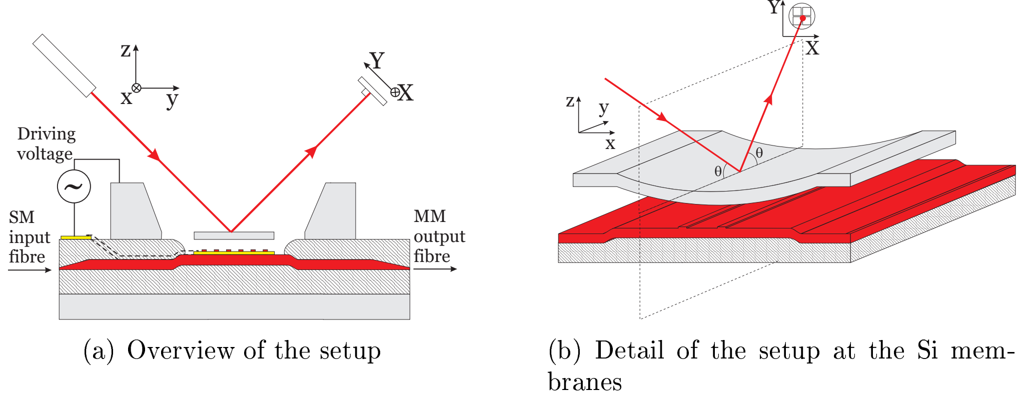

(a) Overview of the setup

(b) Detail of the setup at the Si membranes

Figure 6.20: Setup used for characterisation of the MOEMS containing Si membranes

The optical channel is at the input side connected to a light source by a SM optical fibre and at the output side to a detection unit with a MM fibre.

The light source is a Hewlett-Packard HP-81553SM 1500 nm diode laser and the output power of the fibre is -5 dBm. The detection unit consists of a Hewlett-Packard HP-81536A and its NEP (noise equivalent power) is about 50 pW.

The MOEMS is electrically connected to a voltage source whose output is the sum of a variable DC voltage and a variable (amplitude and frequency) AC voltage. Unfortunately, there is minimum value of the amplitude of the AC voltage being about 100 mV.

For getting more independent information about the deflection of the membrane we decided to monitor this deflection also by measuring the change of the position of a HeNe laser beam, reflected by the centre of the membrane. The change of this position is monitored by a PSD (position sensitive detector) which enables to measure position changes along two mutually perpendicular directions X and Y (see Figure 6.20). Incident beam, reflected beam and PSD are positioned as given in the figure, note that the plane of the PDS is perpendicular to the reflected HeNe laser beam.

Assuming that, at the spot of incidence, the membrane moves parallel to the surface of the IO moves without any deformation, it is expected that the Y-output signal of the PSD will change only. In the framework of this assumption the position change of the reflected beam, Y, is related to the change of the airgap, z, by the simple relation

$$\Delta Y = 2\Delta z \sin\theta \tag{6.37}$$

where θ is the angle of incidence of the laser beam at the membrane surface. In the set up, $\theta = 66.5°$.

The PSD has a sample speed of one sampling per 0.7 seconds. The PSD is calibrated, in that way relating the output voltage to the position change: 450 µm/ V.

Measurements: first series

In a first experiment, the DC voltage, V_{DC}, was stepwise varied while the AC component was held constant at an amplitude of $V_{AC} = 100\,\mathrm{mV}$. The frequency of the AC voltage was 100 Hz. Note that as a consequence of Equation 6.35, the deflection will be proportional to $V_{DC}^2 + 2V_{DC}V_{AC}\sin(2\pi ft) + V_{AC}^2\sin^2(2\pi ft)$ where the last term can be neglected if $V_{AC} \ll V_{DC}$.

In that way both the effect of a DC voltage and the effects of the AC voltage can be determined simultaneously both giving information about the DC position of the membrane.

However, as a consequence of the low sampling rate of the PSD the output signal of the PSD cannot follow the AC voltage frequency but will show a more random character. Results of these measurements are given in Figure 6.21.

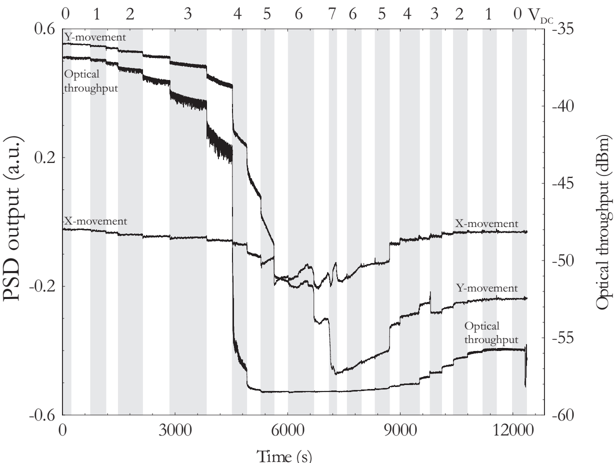

Figure 6.21: Measurement of optical power and PSD output of gyro-demonstrator

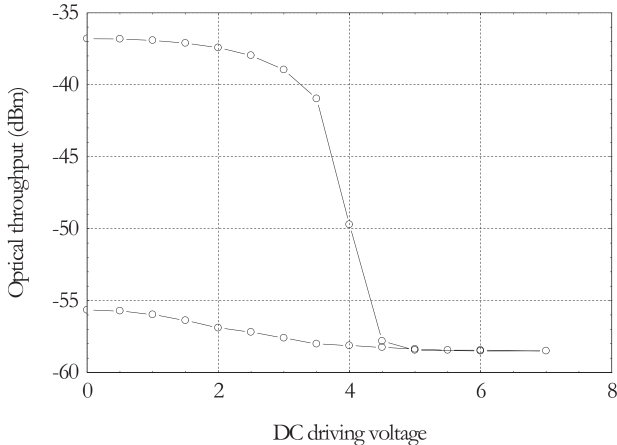

Figure 6.22: Optical throughput in dBm as a function of the applied DC voltage V_{DC}

The experimental results show:

1. The system behaves in an irreversible way: the state of the system at $V_{DC} = 0\,\text{V}$ in the beginning of the experiment is completely different

from the state at $V_{DC} = 0\,\text{V}$ at the end of the experiment. This is additionally shown in figure 6.22.

2. A change of the V_{DC} induces not only a sudden change in the optical throughput (as expected) but also some additional relaxation phenomenon is observed.

3. As expected at increasing V_{DC} the throughput decreases and the amplitude of the AC component of the throughput increases.

4. In addition to an (expected) change of the position of reflected beam in the Y-direction also some position change in the X-direction is observed, pointing to an (unexpected) torsional deformation of the membrane. This latter deformation shows to be reversible.

5. At increasing the voltage to values over $4\,\text{V}$ the change of optical throughput is relatively small or zero even, while the position of the reflected beam is changing remarkably.

6. In the voltage trajectory $7\,\text{V} \rightarrow 0\,\text{V}$ no AC modulation can be observed in the optical throughput signal

These observations lead to the following qualitative picture:

At increasing the V_{DC} the membrane is driven towards the IO wafer, and at first sight the relatively large change in transmission at $V_{DC} = 3\,\text{V} - 4\,\text{V}$ points to the appearance of the pull-in effect causing the membrane to stick to the optical wafer (in spite of the application of the bumps). Also the irreversibility (1) might point to some sticking after which however the transmission decreases yet at increasing the V_{DC} values. Such a decrease can occur if the sticking area of the first sticking does not coincide with the position of the waveguide channel. Then, even after the first sticking, the distance between membrane and waveguide can decrease further, as a result of some further deformation of the membrane. Finally, the transmission would have become that small that the detection limit of the opto-electronic system is reached and further changes of the throughput cannot be detected any more (5). Here it has to be noted, that the experimentally obtained lowest value of the output power, -58 dBm is 12 dB higher than the detection limit of the opto-electronic system , -70 dBm. We ascribe this difference to a constant stray light power incident on the photodiode, which originates from the fiber to chip coupling. Note that at an airgap of 390 nm (corresponding with the height of the bumps) the attenuation is calculated (using Equation 2.10) to be over 200 dB.

An alternative, somewhat speculative, explanation for the irreversibility is the following: As a result of different curvatures of the IO wafer and the MEMS wafer, additional stresses might have been be generated at bonding them together, which might force the membrane to be somewhat curved instead of being flat. Assuming an initial curve as indicated in Figure 6.23(a), at $V_{DC} = 4\,\mathrm{V}$ the membrane might flip from the convex state to a concave one (see Figure 6.23(b)) (at $V_{DC} = 0\,\mathrm{V}$, both states would be energetically identical) but at releasing the voltage the membrane does not return to its original convex state again. Such a flip would also qualitatively explain why the changes of the PSD signal are much higher than theoretically (for a flat membrane) are expected. Adapting this explanation, the low value of the throughput in the concave state at $V_{DC} = 4\,\mathrm{V}$ indicates, that membrane is already very close to the top side of the IO wafer. At higher V_{DC} values the membrane might be driven further to the IO wafer; after decreasing again the V_{DC} to zero, the membrane is left in a concave state in which the torsional deformation (4) has disappeared. This torsional deformation, observed as a change of the X coordinate signal of the PSD is considered to be the result of whether a non-uniformity of the thickness or z_0-position of the membrane or an asymmetry of the applied electrical field.

Another unexpected phenomenon is the observed relaxation. Both the optical throughput signal and the PSD signal show this relaxation so it is improbable that it is an artifact of one of these measurement methods. We may attribute the relaxation to some mechanical phenomena, of which the nature is unknown to us. One can speculate about some gradual disrupture of the bonds between layers, or a gradual shift of the ends of the contacts between the SiO_2 cladding layer and the Si membrane as a result of a process of water adhesion at the surfaces at the corners.

The absence of an AC signal in the throughput signal in the V $7 \rightarrow 0$ trajectory (6) points to locking of the membrane in all these states. In addition however, at these very small distances between membrane and waveguide, squeezing effects may hamper the membrane to follow the 100 Hz AC voltage.

We now will evaluate whether these qualitative pictures can be supported by more quantitative data.

Let we first have a closer look at the PSD data. Starting from the assumption of a solid membrane remaining parallel to the IO wafer, during the electrostatic force induced movements the displacement Δz can be derived from the change of the position of the reflected beam ΔY, using Equation 6.37. However the value of the displacements, calculated from the experimentally obtained maximum Y-signal (1.0 V, see Figure 6.21) and the calibration factor (450 µm/V), is about 450 µm; this is several or-

ders of magnitude higher than the maximum displacement possible with this device, the latter being 510 nm. This clearly points to a simultaneous rotation of the membrane at the laser spot position. Assuming that the changes of the Y-signal were the result of a change in angle only, this change $\Delta\alpha$ can be calculated from the relation

$$\Delta Y = L_{sp} \tan(2\Delta\alpha) \tag{6.38}$$

where L_{sp} is the distance between the centre of the light spot on the membrane and the PSD. Inserting $L_{sp} = 0.29\,\text{m}$ in Equation 6.38, we arrive at $\Delta\alpha = 0.046°$. Taking into account that the membrane is clamped at two sides indeed vertical displacement will be accompanied by some curvature of the membrane and hence by some change of the angle of incidence at the spot on the membrane. Approximating the deflection profile of the membrane as part of a symmetrical triangle, it can be calculated that this change is at least a factor 3 smaller than the experimental one.

However, also imperfections of the MOEMS structure can contribute to this angle change: non-parallelism of the membrane and the driver electrodes (caused by height differences in the cladding of the optical wafer on which the membrane wafer is bonded) or thickness variations of the membrane.

Let we now consider the convex/concave hypothesis and let we assume that in the concave state the membrane would not stick to the IO wafer. Using Equation 6.35 it is expected, that the deflections obtained at identical V_{DC}-values starting from the concave state should be much larger than those starting from the convex state. This is the consequence of the lower distance between membrane and electrodes in the concave state. Also, the compressive stress is expected to favour deflections of the concave state over those of the convex one.

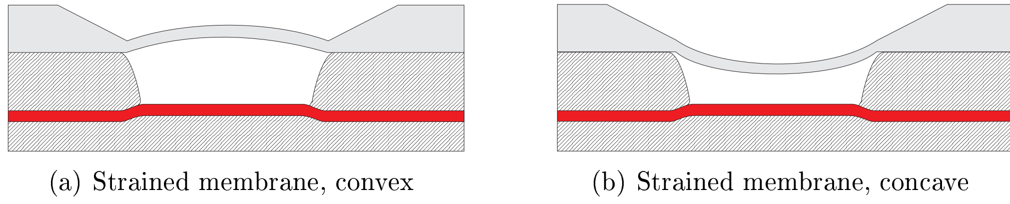

(a) Strained membrane, convex (b) Strained membrane, concave

Figure 6.23: Strained membranes

Considering Equation 6.7, identical displacements of the membranes show the larger effects to the transmission the smaller the original air gap

value. Hence, effects of such a displacement on the transmission should be much larger in the concave state than in the convex one. Hence according the Equations 6.35 and 6.7, both transductions, the electro-mechanical as well as the mechano-optical one, point to larger V_{DC} to T transfer effects in the concave state than in the convex one. However, experimentally, the opposite trend is observed. Hence, whether the idea of a convex and a concave state is wrong or the membrane cannot freely move in the concave state.

In the convex/concave hypothesis, the absolute value of the distance between the centre of the membrane and the neutral plane (the plane of a completely flat membrane at $V_{DC} = 0\,\mathrm{V}$, see Figure 6.23, Δz_0, should be equal in both states. From Equation 6.7 (connecting the membrane displacement to a change of optical throughput T) it can easily be derived from Equation 6.7 that the Δz_0-value can be obtained from the equation:

$$T_1(z_0 + \Delta z_0) - T_2(z_0 - \Delta z_0) = -8.686 c_3'' e^{-c_1 z_0} \left(e^{-c_1 \Delta z_0} - e^{c_1 \Delta z_0} \right) \quad (6.39)$$

in which $T_i = 10 \log \left(\frac{P_{\mathrm{out,i}}(z_0 \pm \Delta z_0)}{P_{\mathrm{out,i}}(z=\infty)} \right)$

For the given structure $c_3'' = -0.56$, $c_1 = 9.16$ (Equations 6.6) while for the flat membrane at $V_{DC} = 0\,\mathrm{V}$ from the structural data of the MOEMS it can be calculated that $z_0 = 900\,\mathrm{nm}$. Taking from Figure 6.21, $T_1(z_0+\Delta z_0) - T_2(z_0-\Delta z_0) = 19\,\mathrm{dB}$, from Equation 6.39 Δz_0 can be calculated to have the value $1.05\,\mu\mathrm{m}$. The result $\Delta z_0 > z_0$ is physically unacceptable. Although inaccuracies of the experimental results may play a role, we interpret this result as slashing our previous hypothesis.

The state in which the membrane is left after the V_{DC} cycle indicated in Figure 6.21) can be modified well by applying an electrical voltage, as is shown in Figure 6.24 below. Here, the membrane is actuated by simultaneous applying a DC voltage $V_{DC} = 3.5\,\mathrm{V}$ and an AC voltage with an amplitude of 3.5 V and a frequency of 0.5 Hz.

From the PSD signals it can be concluded that indeed the membrane deforms at applying the voltages (see the X-signal) but that the membrane starts rotating at the position of the laser spot at higher voltages only. The experimental curve a shown in Figure 6.24 can be fitted (z_0, Δz and $T(z = \infty)$ as fitting parameters) to the theory (using equations 6.7), see Figure 6.25. The values for the fitting parameters here are: $z(V_{DC} = 3.5\,\mathrm{V}) = 0.96\,\mu\mathrm{m}$, $\Delta z = 80\,\mathrm{nm}$ and $T(z = \infty) = -47.9\,\mathrm{dBm}$.

Finally, we have also calculated the pull-in voltage, assuming a flat membrane, at $V_{DC} = 0\,\mathrm{V}$. Starting from Equation 6.34 and inserting a membrane thickness of $13\,\mu\mathrm{m}$ we arrive at: $V_{\text{pull-in}} = 0.85\,\mathrm{V}$.

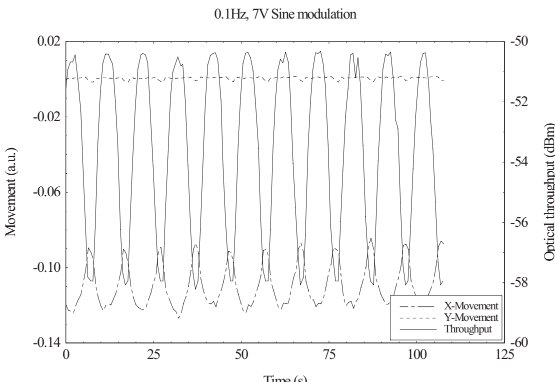

Figure 6.24: Time dependence of the transmission at applying the voltages as given in the text.

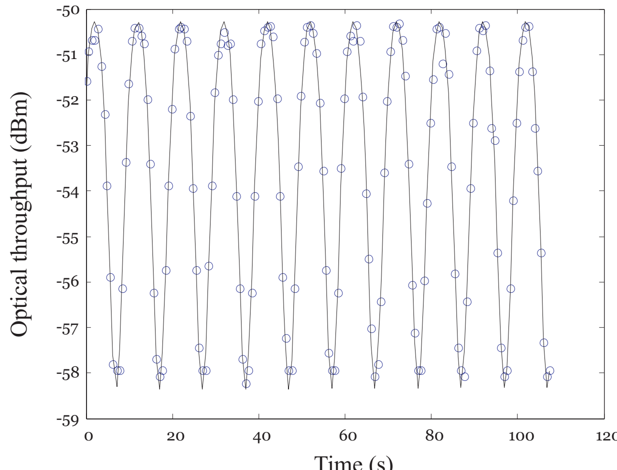

Figure 6.25: Transmission from Figure 6.24 and its theoretical fit.

This value differs appreciably from the value 3.5 V- 4 V (see Figure 6.21), which might be interpreted as a pull-in voltage. The deflection at which pull-in would occur is at one third of the electrode-membrane distance (650 nm), that is, 216 nm.

From the above experimental data and their accompanying calculations, it is clear that the various data sets appear not to correspond with each other.

Although all these deviations between experiment and theory can be discussed further by considering effects of axial loads, they also did us wonder whether they might be caused by a membrane shape which would differ essentially from the flat or convex/concave one with uniform thickness which

we have assumed in the theory.

All above mentioned theoretical formula's and the parameter values calculated from them assume an initially unstressed membrane. When the membrane, at its rest position, would be already subjected to a external force, for example, due to bending of the wafer, these equations will be no longer valid.

So we decided to determine the shape of the back side of the membrane by stylus measurements along various lines over the membrane. Fortunately during these measurements the membrane did not break.

Some results are given in Figures 6.26 and 6.27.

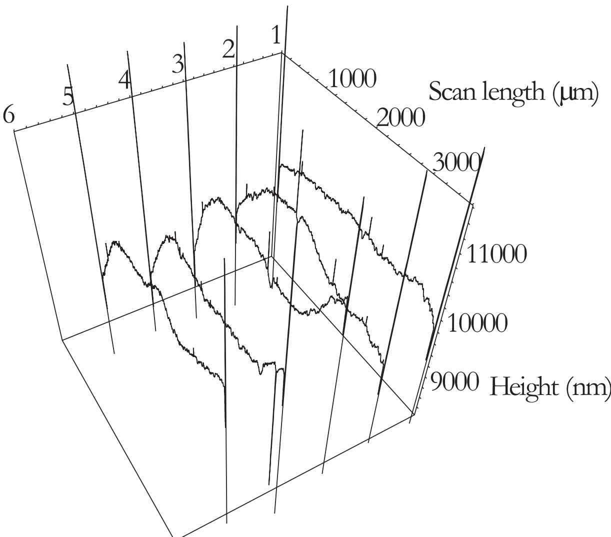

Figure 6.26: Stylus profiler scans parallel to the direction of the waveguides of the silicon membranes at various positions. Measured heights are with respect to the bonding plane of the optical and mechanical wafer.

From the curves in Figure 6.26, we can conclude that the thickness of the membrane is far from homogeneous: the triangular thickenings with a thickness of about 6 μm at the non-clamped edges of the membrane lead to an U-shape of the membrane profile and in between these thickenings the stylus level varies also which can be ascribed to both a non-uniformity of thickness as well as to curvature of the membrane.

Further evaluation of the chosen technological process (see Appendix F) revealed that these triangular thickenings are the consequence of the chosen process steps. In such a structure, the application of the DC voltage may lead to a much more complicated change of position and form of the

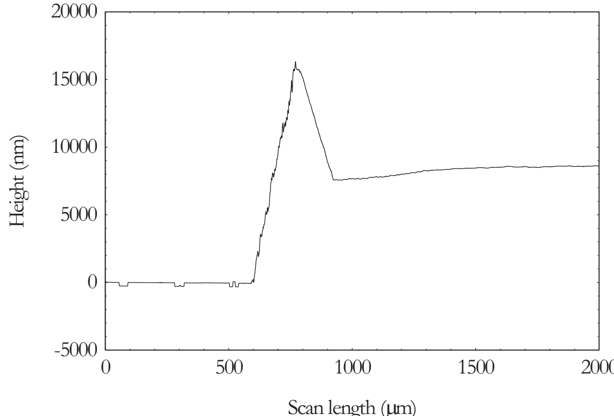

Figure 6.27: Part of the stylus scan along a line parallel to the waveguide axis showing a thickening of the membrane at the membrane edge.

'membrane' than originally envisaged. We did not try to calculate the electromechanical performance of a membrane of this special cross section.

We have to conclude that making a two-sided membrane with uniform thickness without any mechanical tension and analysing the effects of its electrostatically induced displacements on the optical transmission through an adjacent waveguide is much more complicated than originally envisaged and many problems have to be solved yet. This type of MOEMS as produced here are not suited for a quick determination of potential and limitations of the attenuation based optical read out method.

6.9 Read out of Si-plate movements by monitoring the throughput of a free-standing waveguiding channel

Experimental set-up

In these experiments a piece of a Si wafer, which is attached to a piezo-electric actuator is driven into the evanescent field of a free-standing waveguide as is illustrated by the schematic picture of the experimental set up which is given in Figure 6.28.

The IO system containing the free-standing waveguiding channel is placed upon the bottom plate of a massive structure which also encompasses the piezo-actuator provided with a small piece of a Si wafer. For having well defined position changes several orientations have to be properly adjusted:

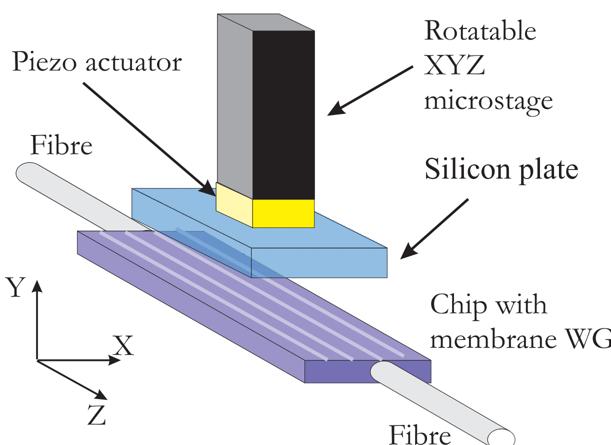

Figure 6.28: Schematic illustration of the measurement setup with the piezo-electric actuated Si-plate.

the direction of the extension of the piezo-electric actuator has to be perpendicular to the upper surface of the IO wafer, while the lower plane of the Si plate has to be parallel to the IO wafer surface. The latter has been accomplished by laying down the Si plate on top of the wafer and subsequently gluing the plate, while it is hold in that position, to a thin bar which is connected to the piezo-actuator. (from attenuation measurements it will be derived later on that in the actual system the angle between both planes was smaller than 0.1°)

The set up shows some weak points:

- thermal drift of the value of the airgap can be expected as a consequence of the fact that the mechanical structure consists of different materials;
- the lower plane of the Si plate had an area of about $3 \times 6\,\mathrm{mm}^2$ and at dynamic operation in air some squeezing effects can be expected.

The piezo-actuator has been characterised by determining the relation between actuation voltage and extension under static conditions (3.65 µm/ V). The piezo-actuator is driven by a voltage supply, whose output is the sum of a variable DC voltage and a variable AC voltage, the minimum value of the latter being 50 mV.

The IO read out system

The IO wafer contains straight ridge-type waveguides which are at the sensing section implemented in a 4 mm long free-standing Si_3N_4 membrane with

a thickness of 100 nm. The membrane section is connected to sections with a core layer thickness of 300 nm by adiabatic tapers. The channel has a width of 4 µm and a ridge height of 4 nm. The thickness of the cladding layer outside the sensing section is 6.0 µm. Hence the smallest value of the airgap is 6.2 µm. As usual the IO circuit is provided of fiber-to-chip coupling sections and V-grooves for attaching the SM input fiber and the MM output fiber. The TM_{00} mode (wavelength 1500 nm) was used for probing the plate deflections.

For states in which the plate is sufficiently far from the waveguide, the following approximate relation for the normalised throughput $T \equiv P_{\text{out}}(z)/P_{\text{out}}(z=\infty)$ can be derived:

$$T = e^{-2k_0 N'' L} \tag{6.40}$$

where $k_0 = \frac{2\pi}{\lambda}$, $\lambda = 1550$ nm and L (=4.0 mm) is the interaction length. N''_{eff} is given by Equation 6.3. Inserting that equation the structure parameters of the interaction section of the waveguide and the wavelength applied, N''_{eff} can be calculated to be:

$$N''_{\text{eff}} = 0.0194e^{-20.63z} (\text{z in } \mu\text{m}) \tag{6.41}$$

From Equations 6.40 and 6.41, the throughput in dB τ can be calculated.

$$\tau \equiv -10 \log T \cong \frac{20 k_0 L N''_{\text{eff}}}{\ln 10} = 2735.7e^{-1.26z} \tag{6.42}$$

And so,

$$z = \frac{\ln(\tau/2735.7)}{-1.26} \tag{6.43}$$

So for the range $z = 6.5 - 11$ µm, the throughput will vary from 0.75 dB to 0.003 dB. It was measured that using a 1550 nm, HP-81553SM photodiode as light source, $P_{\text{out}}(z=\infty) = -26.25$ dBm. So the throughput and its changes are small and power detectors with large sensitivity and good resolution are required.

A first experiment has been performed in which a 0.5Hz AC voltage had been applied to the piezo-actuator of which the value corresponds with a deflection amplitude $\Delta z = 1.1$ µm.

So the airgap z can be given as

$$z = z_0 + 1.1\sin(\pi t)[\mu m] \quad (6.44)$$

Where the value of z_0 is unknown.

Figure 6.29 shows the output power (in dBm) as a function of time, and Figure 6.30 the mechanical amplitude (using Equation 6.43) as a function of the time. We calculated the z_0 value which should give the best fit between theory (Equation 6.42) and the experimental results depicted in Figure 6.29: $z_0 = 9.64\,\mu\text{m}$. There is a small difference between the experimental data and the fitted curve which we ascribe to squeezing effects. The data of Figure 6.30 enables us to calculate z_0 also by using Equation 6.43: $z_0 = 9.75\,\mu\text{m}$.

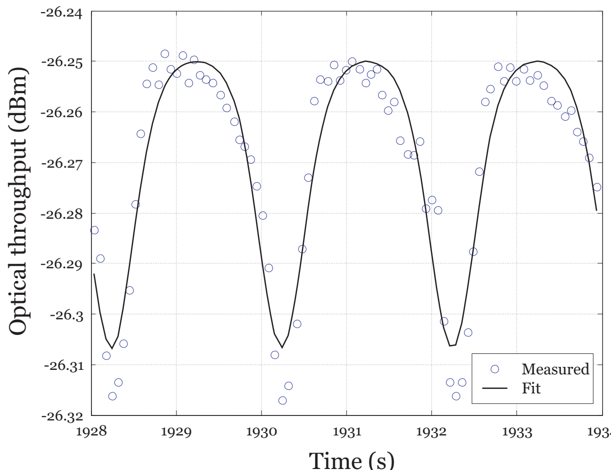

Figure 6.29: Measured throughput of the waveguide as a function of time, with a sinusoidal voltage across the piezo actuator and its best fit with Equation 6.42.

As a second way to compare theory and experiment, we have varied the modulation voltage across the piezo-electric actuators and so, the modulation amplitude Δz. The measured peak-to-peak variation of the optical signal, $\Delta\tau$ is plotted versus Δz in Figure 6.31, indicated by the circles. Theoretical values for $\Delta\tau$ are obtained from Equation 6.42:

$$\Delta\tau = \frac{20}{\log 10} k_0 L C_1 e^{-2\gamma z_0} (e^{-2\gamma\Delta z} - e^{-2\gamma\Delta z}) \quad (6.45)$$

Substituting in Equation 6.45, $z_0 = 9.64\,\mu\text{m}$, the value found in the first experiment and using Equation 6.42, $\Delta\tau$ has been calculated as a function

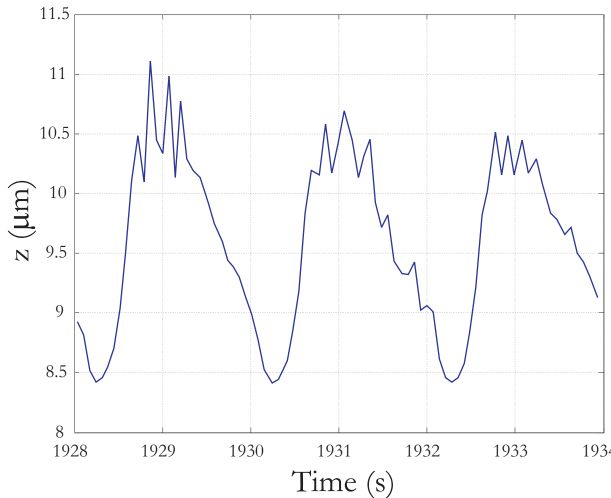

Figure 6.30: Calculated value of z_0 as a function of time.

of Δz (shown as the solid line in Figure 6.31). The measured and calculated $\Delta\tau$-values show good correspondence. The small deviations are attributed to small changes in Δz due to drift in z_0.

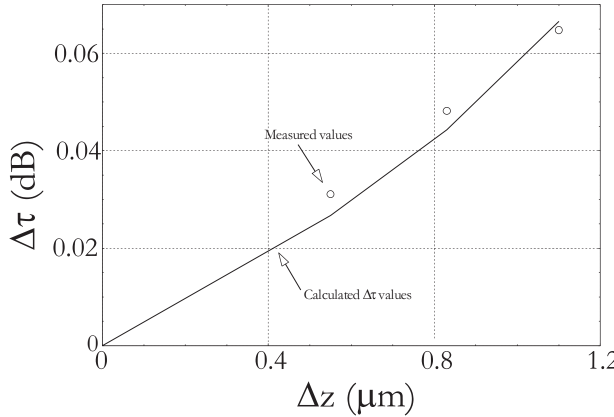

Figure 6.31: Measured throughput variation (peak-to-peak), $\Delta\tau$, as function of Δz.

Although we obtain good correspondence between experiment and theory, this series of experiments cannot be used well for getting an impression of the potential of this method. Although now (opposite to the membrane experiments) the end-plane of the object to be driven into the evanescent field conserves its flatness and its spatial orientation, other, not well con-

trolled, aspects pop up: a small difference in orientation of the Si plate and the surface of the IO wafer may exists and at the AC experiments squeezing may influence the deflections. It appeared not well possible to perform the measurements under vacuum conditions, given the available time. Also, the use of a voltage source, whose output always had to be a superposition of a DC and AC voltage, was very disadvantageous.

6.10 Discussion

Investigation of the potential of attenuation based read out of MOEMS appeared to be more complicated than originally envisaged. Although, for perfect systems, a useful theoretical framework has been developed to describe the performance of those systems, especially imperfectness of the MOEMS hampered a reliable comparison of theory and experiments. And this comparison would have been the base for presenting statements on the potential of the readout method. Also more sophisticated electronics for actuating the MOEMS and processing the output signals would have been welcome. The latter the more because the effectuated changes of optical output power were calculated to be small being in the order of one percent of the power itself. We have to confess, that sometimes from evaluating the experimental results we had to conclude that we had not made the most advantageous configurations for performing and/or analysing the experiments. However, most and most relevant problems arise from imperfectness of technology. For example, the outer surface of the gyro MEMS (produced by Thales-Av), appeared to be provided with contaminations, which prevented any bonding of this MEMS wafer to the optical wafer. These contaminations of unknown nature appeared to withstand all cleaning procedures we had available. Because we were very interested in the potential of the attenuation based readout we decided to spend the remaining short period to produce and characterise two types of MOEMS systems which would mimic the gyro action: a membrane containing MEMS, the membrane driven electrostatically and a Si plate driven piezoelectrically. The membrane system appeared to be more complicated than originally envisaged. Applying the technological scheme we had developed, no membranes with uniform thickness have been obtained, but the thickness appeared to vary strongly in an irregular way with the spatial position.

This had the consequence that we were not able to describe the mechanical behaviour of this membrane adequately. Also, we were confronted with effects of mechanical tensions existing in the MEMS and/or IO wafer. After bonding both wafers together, a MOEMS with also unknown inter-

nal tensions was obtained and these tensions will influence the investigated performance in an unknown way. Also some unexpected relaxation in the membrane-MOEMS phenomena have been observed which we also tend to attribute to imperfect technology. The systems were too uncontrolled for enabling a thorough comparison of theoretical and experimental performance and just this comparison is needed to evaluate the principle. A preliminary experiment has been performed by driving piezoelectrically a Si plate into the evanescent field of the waveguide. Also here more sophisticated auxiliary equipment than was available, should have been used, for example, for characterising the precise relative orientation of plate and IO system and for measuring their distances in an independent way. Controlling the relative position and orientation of the MEMS and IO wafer is also expected to be one of the main problems in non permanently bonded MOEMS. Also, we have to be aware that dynamic behaviour of MEMS close to the IO wafer is influenced by squeezing resulting for example, in lower quality factors and shifts of resonance frequencies in resonating systems such as the micromechanical vibrating gyros. Considering all this, we have to be modest and we can characterise the main part of the research performed in this chapter as exploring only, mainly because the theory has been developed for perfect systems while in practice, up to now, uncontrollable and relevant deviations from perfection have been observed.

For continuing this type of research, whether these imperfections have to be reduced or the systems have to be adequately characterised; a characterisation which should open the doors to a precise theoretical prediction of their (opto-)mechanical behaviour.

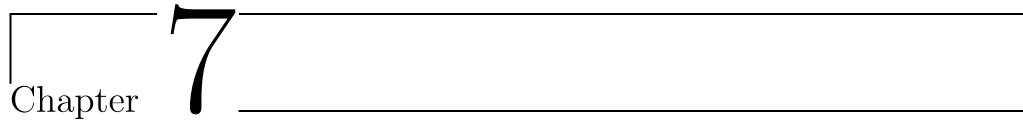

Chapter 7

Summary

In this chapter, the main results of the previous chapters are summarised and a general evaluation of the research is given.

7.1 Summary of the main results

Chapter 1: Preface The research presented in this PhD thesis was part of the European GROWTH project 'Optical Characterisation Methods for MEMS manufacturing (OCMMM)'. The general aim of this project was to develop methods for measuring deflections generated in MEMS systems. These methods, divided into 'full-field' and 'on chip' techniques have been described shortly and the partners participating in this project have been presented. The research described in this thesis was part of the 'on chip' techniques.

Chapter 2: Introduction A brief introduction to integrated optics (IO) has been given, focusing on the description of an IO Mach-Zehnder Interferometer system, which will play a central role in the 'on chip' part. Two classes of MOEMS systems for read-out of the mechanical deflections have been introduced: 'loaded' systems characterised by a monolithic integration of MEMS and IO systems and 'unloaded' systems characterised by a hybrid integration of a MEMS system and an IO read-out system both realised on different Silicon wafers. This PhD thesis focuses on various 'unloaded' MOEMS systems in which the read out of the mechanical deflections is based on evanescent field sensing.

Three demonstrator devices have been planned: devices for read-out of an electrostatically driven rotatable mirror, a piezoelectrically

driven vibrating membrane and a vibratory MEMS gyroscope. Structure, fabrication method and application of these MEMS systems, each of these to be produced by one of the other project partners, have been described shortly. The main tasks of this PhD project are to develop and analyse evanescent field sensing based read-out methods, to design, realise and characterise three dedicated IO read-out systems, to integrate the IO and MEMS systems and to characterise the MOEMS system with a focus on its functional performance.

Chapter 3: Theory In evanescent field sensing based read-out systems the moving part of the MEMS is driven into the evanescent field of a mode propagating through the IO system. The variation of the distance between the outer edge of the moving part and the upper surface of the core layer of a waveguide channel influences in a regular way some properties of the mode propagating through this channel. Very effective, for sensing purposes, is the influence of the moving part on the effective refractive index, N_{eff}, of the mode. Two extremes have been distinguished in which the change of either the real or the imaginary part of is dominant. First extreme results into a local change of the propagation speed and measurement methods based on the detection thereof are called 'refractive'; second case leads to a local variation of the attenuation of the mode and sensing methods based on that are called 'absorptive'. Both methods have been analysed both in a qualitative and a quantitative way. For the quantitative analysis an approximate method based on the ray-picture model has been described and applied.

Application of the SiON technology as has been developed by the IOMS group of MESA+ institute was given as an a priori boundary condition. Common two-layer monomodal SiON waveguides consisting of a Si_3N_4 core layer and a SiO_2 buffer layer are shown to enable measurements of movements in the range 0.5 µm- 1.5 µm only, but in SiON based systems also free-standing waveguides can be made locally, which consist of a single about 100 nm thick Si_3N_4 layer two sided surrounded by air, in which a 1550 nm wavelength TM mode enables measurement ranges up to 11 µm- 15μm.

Chapter 4: free-standing (membrane) waveguides Fabrication of free-standing slab waveguides shaped as an all sided clamped thin membrane consisting of either stoichiometric Silicon nitride, Si_3N_4 (tensile stress), or the low stress material silicon-rich silicon-nitride, Si_RN, has been investigated. A high temperature BHF etching process has been

developed enabling a fast local etching off of about 200 nm thick Si_3N_4 or Si_RN layers without relevant chemical attack of the protecting resist layers. By adjusting the adhesion between the resist layer and the Si_3N_4 layer tapered transition sections in-between the unetched 300 nm thick core layer sections and the etched off 100 nm section have been obtained with a taper angle of about 0.3°, enabling low loss nearly adiabatic propagation of the mode from the thicker to the thinned core layer sections and vice versa. Using a backside KOH etch process for locally removing the underlying silicon, free-standing membranes with thicknesses down to 20 nm and an area of several square millimetres, have been produced with nearly 100% yield. The Si_RN membranes with thickness lower than 45 nm however showed some unexpected wrinkling pointing to the presence of compressive stress in the material. The tensile stress in the Si_3N_4 layer affords for very flat membranes. As a result of the etching the surface roughness of the Si_3N_4 layer was increased and comparing losses of waveguiding channels with free-standing sections with those of waveguides without such sections the membrane induced losses have been measured to be 2.6 dB and 8 dB for the fundamental TE and TM mode respectively.

Chapter 5: The electrostatically driven mirror demonstrator The structure and relevant properties of the rotatable mirror systems, as are produced by the Technical University of Chemnitz are given, just as the requirements to the read out. The size of the mirrors together with the maximal rotation angle, 2.5 degrees, forced us to define large holes in the silicon wafer next to the waveguiding structure in order to enable free movement of the mirror. This could be achieved by producing free-standing waveguides supported at the edges by a thin silicon bridge. Two methods of producing these subsystems have been investigated, in which locally the Si was removed either by front side wet KOH etching starting from trenches in the Si or by back side etching off the silicon starting from well defined openings in the SiON layers which have been applied also on the back side of the wafer. Obtained results lead to initial preference for the latter method.

It was decided to apply a refractive method for read out of the rotation angle applying a Mach-Zehnder interferometer. Taking into account the requirements of spatial and technological compatibility of the MEMS and the IO structures, the IO structure has been designed. Although maintaining the integrity of the MEMS was a starting point, some small features of the MEMS had to be adapted to the IO wafer for enabling their hybrid integration.

The IO wafers have been realised and characterised. Based on preliminary experiments the MEMS and the IO wafer have been bonded together by direct bonding. Next the structure has been provided with a Pyrex wafer, supporting the electrodes for driving the mirror, by a gluing process. Two types of MOEMS systems have been produced. In the first one complete wafers were bonded together and microscopic observation showed well aligned systems without any sticking of the mirror to the membrane. However, at dicing the system the Pyrex wafer was loosened and all systems were destroyed. In a second batch, all wafers were diced individually before providing the Pyrex wafer and the individual 'one system' parts have been provided of an electrode wafer-part afterwards. Unfortunately in all systems the bridge of the IO wafer touched the mirror. Microscopic observation also indicated that the bridges were curved somewhat and this was attributed to stresses generated in the silicon supports of the bridge. Application of DC voltages did not enable physical separation of both parts. Nevertheless, some experiments have been performed on these systems: during applying the actuating voltages both the optical output of the MOEMS and the reorientation of the mirror have been measured. Because methods to determine the relative spatial coordinates inside the bridge-mirror subsystem accurately were missing, the experimental results could not be compared with theoretical predictions.

Chapter 6: The piezo-electrically driven membrane demonstrator Relevant properties of the membrane are given, the topology of the MEMS wafer has been designed and requirements have been set to the membrane demonstrator. The MOEMS will be of the refractive type; for the IO wafer a set of serrodyne modulated MZI's has been designed with a lateral lay out matching that of the membrane wafer. Due to the limited area available, curved MZI's have been designed and a special type of shadow mask has been developed in order to apply locally the ZnO in a laterally curved structure. For enabling the application of electrical connections to the modulator, to be made at the back side of the wafer, Electrical Through Wafer Interconnects (ETWI's) are envisaged. Unfortunately, the MOEMS could not be composed; due to irregularities at the surface of the membrane wafer as produced by our project partner Thales-RT, bonding of the MEMS wafer to the IO wafer was not realisable.

Chapter 7: The MEMS vibratory gyroscope In the MEMS vibratory

gyroscope a rotation of the gyroscope around a given axis expresses itself as a mutually anti-phased movement of two silicon plates along a line perpendicular to an end plane of the MEMS. So at first sight the measurement problem seems to be similar to that in the rotating mirror case. However of the displacements of the plates are in the order of magnitude of 1 nm, that is, about three orders of magnitude smaller than the mirror. Therefore, the focus was shifted from obtaining a large measurement range to a high resolution.

Three sensing configurations have been analysed: two types based on refractive sensing by an MZI and one based on attenuation measurements. It was concluded that all three configurations show similar sensitivities. Finally it was decided to concentrate on the attenuation based method, a decision which was mainly driven by the desire to get familiar with the specific problems arising from implementing this method. Propagation of a TE mode with 1550 nm wavelength through a 'common' type waveguide was calculated to be a good option.

In such a gyroscope, rotations are converted into the aforementioned movements along the vertical direction as a result of Coriolis forces working on the laterally vibrating masses. However, in our experiments we should focus on measuring the small translations of the masses and it was decided to generate these translations in a simpler way: by utilising electrostatic forces.

Relevant properties of the gyro are given by Thales-Av just as a set of requirements which have to be obeyed. A design of the IO structure matched to that of the gyro has been made; integrity of the MEMS could not be maintained and several small modifications have been suggested. A fabrication process for the IO systems has been defined and the IO systems have been produced. However, the bonding plane of the MEMS wafer, as produced by Thales-Av appeared to be contaminated with particles of unknown nature, which could not be removed using cleaning methods common in the MESA+ clean room laboratory. These contaminations hampered any bonding of these wafers to the IO wafer. We decided to replace the gyro by other structures which also show a small well controlled movement along the vertical direction: a vibrating electrostatically driven membrane and a silicon plate driven piezo-electrically into the evanescent field of the mode. Imperfectness of the Si membranes however allowed for measurements which could be interpreted qualitatively only, but a thorough comparison with theory appeared to be impossible. Experiments with the piezo-electrically driven system have been performed

and an acceptable fit of the experimental results with theory could be obtained.

7.2 General evaluation of the research presented in this PhD thesis

We have learned that the objectives defined for this four year project were too ambitious to be reached. However, projects without high ambitions generally score badly in European programmes. During working out the various lines of research, problems have been met which had not been foreseen in the definition stage of the project. Especially the mechanical structures, the MEMS, as delivered by the partners or made by ourselves did not come up to expectations. Due to stresses, initial shapes appeared to deviate from the idealised ones and during actuation often spurious movements and deformations did occur, disturbing the clear relationships between movements and their optical effects as had been obtained theoretically assuming perfect behaviour of these systems. Unfortunately we had no full field optical methods available to measure all these spurious effects and so in general conclusions of qualitative and semi-quantitative nature could be drawn only. Also requirements to obtain the intended wafer bonding could not be fulfilled completely: contamination of the bonding planes of MEMS structures delivered by our partners and too high wafer curvatures often hampered the built up of the intended hybrid MOEMS systems. Also we struggled with the fact that needed MEMS devices often were not delivered timely by the partners. So, in retrospection the research showed more an exploring character in stead that clear statements about the potential of evanescent field methods could be made.

Nevertheless an appreciable progress has been made. A theoretical frame-work for MOEMS systems with evanescent field read-out of the movements has been given.

More insight has been gained in the potential and limitations of the evanescent field based read out methods, both the refractive and the absorptive ones. Main problems have been identified and several of these have been solved.

It was concluded that the measurement range of MEMS deflections can be enlarged enormously by producing free-standing waveguides in the sensing section of the IO structure. A TM_0 mode of wavelength 1550 nm propagating through a free-standing Si_3N_4 membrane with a thickness of 100 nm extends the measurement range of the MZI system to 11μm. Thinner wave-

guides enable even larger measurement ranges.

A method for making free-standing waveguides in SiON technology has been developed and membrane thicknesses down to 30 nm can be obtained with nearly 100% yield. These waveguides are not only suited for this type of optical read-out systems but also for the absorptive sensors with a relative sensitivity larger than unity as suggested in [VPHL00]. A method for bonding already diced pieces of wafers together has been developed. Methods for obtaining small angle vertical tapers, functioning as adiabatic transitions between waveguide sections of different geometry have been improved. When driving a piezo-electrically a silicon plate in the evanescent field of the sensing region optical throughput measurements based on the attenuation method showed a good correspondence with theory.

However, obtaining an evanescent field read-out method of movements of parts of MEMS, which can compete with or even excels the capacitive read out method requires a lot more research in which especially problems concerning imperfect shapes and movements of MEMS systems have to be taken into consideration. Note that evanescent field read out of mechanical *frequencies* is not hampered by the imperfect shapes and movements of the MEMS parts and therefore deserves special attention in future research.

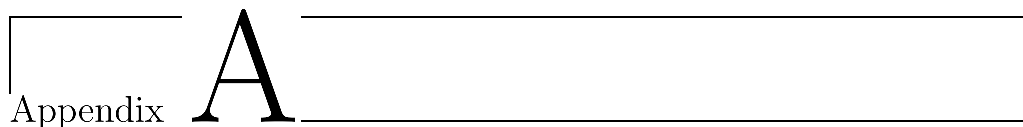

Bonding techniques

A.1 Silicon-fusion bonding

Silicon-fusion bonding is a standard bonding method commonly applied in MEMS fabrication to bond silicon on silicon or silicon on a SION-type layer [GAG+97]. The wafers that have to be bonded have to meet the following requirements:

- the bonding surface should have a surface roughness less then 1 nm;
- the maximum curvature of the wafer should should correspond to a 100 µm height difference between centre and edges of the wafer.

Experiments performed by TUC showed that good Si-Si_3N_4 bonding was achieved by using their standard values for the bonding parameters used for Si-SiO_2 bonding.

The bonding process consists of seven steps:

1. oxygen-plasma treatment to activate the wafer surface (both wafers);
2. alignment of the wafers using a bond-aligner and a special frame that holds both wafers in their aligned state (the wafers are vertically separated by spacers);
3. in their aligned state, the wafers are placed in a vacuum chamber which is then evacuated and heated to 300 ℃;
4. a pin is pressed onto the centre of the top wafer, applying a controlled force to initiate the bonding;

5. the spacers are removed and a controlled pressure is applied to the entire upper wafer by means of a membrane;
6. the two-wafers system is now in the *pre-bond* state;
7. the bonded wafer system is annealed in a nitrogen atmosphere at 200 ℃ for 3 hours to strengthen the bond.

In this way, several test wafers were bonded together and the bond was examined by IR-microscopy (shown in Figure A.1) and from the image, bonding over the entire wafer was concluded. Also the system has been subjected to the Maszara-method to test the bond-strength [MGCM88]. Bond strengths of beyond 2.5 J/ m^2 were measured which are similar to the bond strengths measured for Si-Si bonding or Si-SiO_2 bonding.

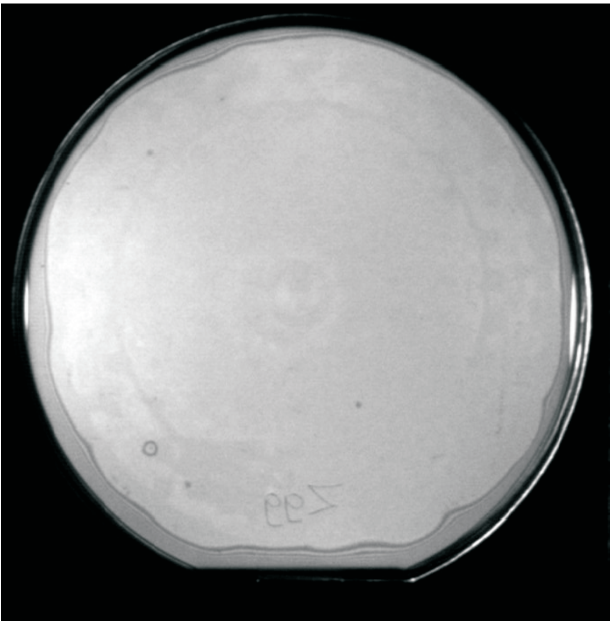

Figure A.1: IR image of two bonded test wafers showing bonding over the entire wafer surface

A.2 SU-8 polymer bonding

A wafer bonding process using an intermediate SU-8 polymer layer has been developed by TUC during the OCMMM project. Also this bonding process consists of seven steps:

1. spin-coating of the SU-8 layer (15 µm thickness) on a Pyrex wafer;
2. patterning of SU-8 layer to match the layout of the MEMS wafer;
3. alignment of the wafers using bond-aligner and a special frame that holds both wafers in their aligned state (the wafers are vertically separated by spacers);
4. in their aligned state, the wafers are placed in a vacuum chamber which is then evacuated and heated for a short time to 95 ℃;
5. a pin is pressed onto the centre of the top wafer, applying a controlled force to the centre of the wafer to initiate the bonding;
6. the spacers are removed and a controlled pressure is applied to the entire wafer by means of a membrane;
7. the temperature is gradually lowered to room temperature;
8. the bonded wafer is then removed from the vacuum chamber placed on a hotplate of 95 ℃ to polymerise the SU-8 layer to strengthen the bond.

A Maszara-method test of these bonded wafers showed bond strengths of 1.3 J/m^2 and beyond, indicating a good bond.

Process scheme for fabrication of MZI demonstrator

Table B.1: Fabrication scheme for the micro-mirror IO-circuit

Step	Description	Crosssections
1	• Thermal oxidation • Determination of crystal orientation • Etching of alignment marks	3 µm 360 µm 3 µm
2	• Lithography (Sensor window) • Wet etching SiO_2 (BHF) from 3 µm to 0 µm thickness • Lithography (modulator section) • Wet etching SiO_2 (BHF) from 3 µm to 1 µm thickness	The left-hand side part of the figure above shows the fibre-to-chip-coupling section, the middle part shows the optional ZnO modulator section and the right-hand side part shows the sensing region.
3	• LPCVD Si_3N_4 (300 nm)	

Continued on the next page

Table B.1: Fabrication scheme for the micro-mirror IO-circuit - continued

Step	Description	Crosssections
4	• Lithography (sensing and FC coupling sections) • Wet etching Si_3N_4 (BHF) from 300 nm to 70 nm (alternatively 0 nm)	
5	• Lithography (waveguide + V-grooves) • Wet etching Si_3N_4 (BHF) 6 nm ridge	In the right-hand side of the figure, the cross-section perpendicular to the propagation direction of the sensing section is added (indicated by the arrow).
6	• Lithography (resist on resist: cover waveguides) • Dry etching Si_3N_4 (RIE) (etching V-groove mask in Si_3N_4)	
7	• PECVD SiO_2 (frontside + backside) • CMP (Polishing upper surface) • Lithography (modulator section and sensing windows) • Wet etching SiO_2 (BHF)	

Continued on the next page

Table B.1: Fabrication scheme for the micro-mirror IO-circuit - continued

Step	Description	Crosssections
8	• LPCVD Si_3N_4 (protection layer) 30 nm (alternatively 100 nm)	
9	• Sputter ZnO (shadow mask)	
10	• PECVD SiO_2 • Lithography (electrodes) • Sputter Cr/Au and lift-off • PECVD SiO_2 Lithography (unwanted oxide) • Wet etching SiO_2 (BHF)	
11	• Lithography (sensing section, frontside) • Dry etching Si_3N_4	
12	• Lithography (sensing section, backside) • Dry etching Si_3N_4 (30 nm) • Wet etching SiO_2 (5 µm) • Dry etching Si_3N_4 (300 nm) • Wet etching SiO_2 (1.5μm)	

Continued on the next page

Table B.1: Fabrication scheme for the micro-mirror IO-circuit - continued

Step	Description	Crosssections
13	• Lithography (bridge WG, Si supports, backside) • Wet etching SiO_2	
14	• Wet etching Si (KOH, until Si_3N_4 is reached) • Wet etching SiO_2 mask (BHF) • Tuning thickness of Si supports (KOH)	
15	• Bonding MM-OPT (Si on Si_3N_4) • Low temperature (<500°C) • Bonding OPT-Electrode wafer (UV-curing glue) • Dicing • Fiber pigtailing	

Sourcecode listings of used Matlab programs

C.1 Main program

```
 1 % Calculates \Delta N_{eff} for waveguides with
 2 % multilayer MEMS in evanescent field
 3 %
 4 % 2001-2005, Hugo Hoekstra, Geert Altena
 5 %
 6 % INPUT:
 7 % wavelength (lambda)
 8 % refractive indices of used layers
 9 % thickness(ranges) of the used layers
10 % (all thicknesses in microns)
11 % reference effective indes of unpertubated structure
12 %
13 % OUTPUT:
14 % real and imaginary effective index changes
15 % attenuation values (dB/cm)
16 %
17 %%%%%%%%%%%%%%%%%%%%%%%%%%%%%%%%%%%%%%%%%%%%%%%%%%%%%%%%%
18
19 % Used stucture
20 %%%%%%%%%%%%%%%%%%%%%%%%%%%%%%%%%%%%%%%%%%%%%%%%%%%%%%%%%
21 % |  MP layer 0
22 % +--------------------------------------
23 % |  MP layer 1
24 % ---------------------------------------
25 % |  MP layer 2
```

```
26 % |       :
27 % |       :
28 % |       :
29 % |  MP layer X
30 % +---------------------------------------
31 % |  Cladding
32 % +---------------------------------------
33 % |  Core layer
34 % +---------------------------------------
35 % |  Cladding
36 % +---------------------------------------
37 %%%%%%%%%%%%%%%%%%%%%%%%%%%%%%%%%%%%%%%%%%%%%%%%%%%%%%%%%
38
39 % Used equation to calculate \Delta N:
40 %%%%%%%%%%%%%%%%%%%%%%%%%%%%%%%%%%%%%%%%%%%%%%%%%%%%%%%%%
41 %
42 %               i         r_{u,1}
43 % \Delta N = ----- * ln(---------)
44 %             k_0*W      r_{u,u-1}
45 %
46 % with:
47 % r_{i,j} : The reflection coefficient at interface i-j
48 % k_0     : The wave number 2*\pi / \lambda
49 % W       : The propagation distance after 1  zig-zag
50 %
51
52 clear;
53 close all;
54
55 % Start definition of used variables
56 %%%%%%%%%%%%%%%%%%%%%%%%%%%%%%%%%%%%%%%%%%%%%%%%%%%%%%%%%
57
58 % Core layer
59 t_c=0.1;                         % thickness
60 n_c=1.97929;                     % refractive index
61
62 % Air cladding
63 t_cl0=1;                         % clad thickness start
64 t_cl1=1;                         % clad thickness end
65 dt_cl=.05;                       % clad thickness change
66 i_cl=(t_cl1 - t_cl0)/dt_cl + 1;
67 n_cl=1;
68
69 % MP layer 1
70 t_m0=.001;                       % MP1 thickness start
71 t_m1=.2;                         % MP1 thickness end
72 dt_m=0.001;                      % MP1 thickness change
```

```
73  i_m=(t_m1 - t_m0)/dt_m + 1;
74  %n_m=1.44-15.955i;              % Al
75  n_m=0.18-10.21i;                % Au
76  %n_m=1.45;                      % SiO2
77  %n_m=5.31-7.04i;                % Pt
78  %n_m=0.44-12.9i;                % Ag
79  %n_m=4.18-4.96i;                % Cr
80
81  % MP substrate (layer 0)
82  n_s=3.47;                       % Si
83  %n_s=1.45;                      % SiO2
84  %n_s=2.44;                      % PZT
85
86  lambda=1.55;                    % Used wavelength
87  k0=2*pi/lambda;                 % Wavevector
88
89
90  %n=[n_s n_cl n_c n_m];          % index 0 MP layer
91  n=[n_s n_m n_cl n_c n_cl];      % index 1 MP layer
92
93  q=length(n);
94  l_cl=q-2;                       % clad layer number
95  l_c=q-1;                        % core layer number
96
97  esp=n.^2;
98
99  % Effective index of undisturbed structure
100 n1=1.012081864;                 % Si3N4 100nm core
101
102 % End of variable definitions
103 %%%%%%%%%%%%%%%%%%%%%%%%%%%%%%%%%%%%%%%%%%%%%%%%%%%%%%%%%
104
105 % Start of calculation
106 %%%%%%%%%%%%%%%%%%%%%%%%%%%%%%%%%%%%%%%%%%%%%%%%%%%%%%%%%
107
108 result=[];
109
110 for t_cl=t_cl0:dt_cl:t_cl1
111    for t_m=t_m0:dt_m:t_m1
112
113       % definition of the thickness and index vectors
114       %%%%%%%%%%%%%%%%%%%%%%%%%%%%%%%%%%%%%%%%%%%%%%%%%%%
115
116       %t=[0 t_cl t_c 0];          % Thickness 0 layer
117       t=[0 t_m t_cl t_c 0];      % Thickness 1 layer
118
119
```

```
120        % Calculate W
121        %%%%%%%%%%%%%%%%%%%%%%%%%%%%%%%%%%%%%%%%%%%%%%%%%%
122        b1=k0*n1;
123        fi_c=(esp(l_c) - n1^2)^0.5 * 2*k0*t_c;
124        [ref,tran,alf]=REF_TM(b1,lambda,t,esp,l_c,l_cl);
125        thet=angle(ref);
126        thet1=-fi_c+2*angle(ref);
127
128        n2=n1+1e-6;
129        b2=k0*n2;
130        fi_c=(esp(l_c)-n2^2)^0.5 * 2*k0*t_c;
131        [ref,tran,alf]=REF_TM(b2,lambda,t,esp,l_c,l_cl);
132        thet2=-fi_c+2*angle(ref);
133
134        W=(thet2-thet1)/(b2-b1);
135
136        % Calculate \Delta N_{eff}
137        %%%%%%%%%%%%%%%%%%%%%%%%%%%%%%%%%%%%%%%%%%%%%%%%%%
138        [r31,tran,alf]=REF_TM(b1,lambda,t,esp,l_c,1);
139        [r32,tran,alf]=REF_TM(b1,lambda,t,esp,l_c,l_cl);
140
141        d_neff=i/k0/W * log(r31/r32);
142        dre_neff=real(d_neff);
143        dim_neff=imag(d_neff);
144
145        att=20*log10(exp(-k0*1000*dim_neff));
146
147        %antw=[t_cl t_c dre_neff dim_neff att];   % 0 layer
148        antw=[t_m t_cl t_c dre_neff dim_neff att];% 1 layer
149        result=[result;antw];
150
151    end
152 end
153
154 % EOF
155 %%%%%%%%%%%%%%%%%%%%%%%%%%%%%%%%%%%%%%%%%%%%%%%%%%%%%%%%%%
```

C.2 Auxiliary program

```
  1 function [ref,tran,alf]=REF_TM(beta,lambda,t1,esp1,l1,l2);
  2
  3 q=abs(l1-l2)+1;
  4 if l1>l2
  5  for l=1:q
```

```
 6    t(l)=t1(l1-l+1);
 7    esp(l)=esp1(l1-l+1);
 8   end
 9  else
10    for l=1:q
11     t(l)=t1(l1+l-1);
12     esp(l)=esp1(l1+l-1);
13    end
14  end
15
16  k0=2*pi/lambda;
17  alf=(beta^2-k0^2*esp).^0.5;
18  % Re(alf)>0, unless Re(alf)=0, then Im(alf)>0
19  for m=1:q
20   if real(alf(m))<0
21    alf(m)=-alf(m)
22   end
23   if real(alf(m))==0
24    if imag(alf(m))<0
25     alf(m)=-alf(m)
26    end
27   end
28  end
29  ur(q)=1;
30  % only outgoing plane waves, or decaying waves,
31  % ur = H_y, vr =H_y'
32
33  vr(q)=-alf(q);
34
35  for l=q-1:-1:2
36   wexp=exp(alf(l)*t(l));
37   wexpi=1/wexp;
38   csh=(wexp+wexpi)/2;
39   snh=(wexp-wexpi)/2;
40   if abs(alf(l))>1e-8
41    h1=snh/alf(l);
42    else
43    h1=t(l);
44   end;
45   h2=snh*alf(l);
46   ur(l)=ur(l+1)*csh-vr(l+1)*h1*esp(l)/esp(l+1);
47   vr(l)=-ur(l+1)*h2+vr(l+1)*csh*esp(l)/esp(l+1);
48  end
49
50  if abs(alf(1))<eps
51     ref=-1;
52     tran=0;
```

```
53 else
54     ap=(alf(1)*ur(2)+vr(2)*esp(1)/esp(2))/(2*alf(1));
55     am=(alf(1)*ur(2)-vr(2)*esp(1)/esp(2))/(2*alf(1));
56     ref=ap/am;
57     tran=1/am;
58 end
59
60 % EOF
```

Electrical Through Wafer Interconnects

Applying the electrical connections to the modulator electrodes on the frontside of the IO wafer, that is, the wafer side that has to be bonded to the MEMS wafer requires that holes are made in the MEMS wafer to access these electrodes. If applying the wires at the backside, these holes are not needed and the integrity of the MEMS wafer is maintained. Backside wiring requires Electrical Through Wafer Interconnects

To enable these electrical connections at the backside of the wafer, several technologies have been considered [Hes99, CCP$^+$02]. Consideration of the technological facilities, which are available in the MESA$^+$ cleanroom laboratory, the fabrication steps needed for realising the different feedthrough structures together with the requirement that these technologies have to be compatible with the implementation of membrane structures resulted in a strong preference for a special type of Electrical Through-Wafer Interconnect structures [CCP$^+$02], of which two different modifications are shown in Figure D.1: an unshielded version and a shielded version.

These types of interconnects have three major advantages over other types. Firstly, these ETWI's can be fabricated as a first step in the processing of the optical wafer. As such, they don't interfere with the later, sometimes critical, steps in the fabrication process. Secondly, the planar structure of the wafer is maintained as the holes which are etched in the wafer are refilled in subsequent steps and the wafer surface after the ETWI fabrication is smooth enough to allow the fabrication of the optical layer stack without the need for adding special preparation steps. Thirdly, because the holes are refilled with Si, the structural integrity of the wafer is maintained.

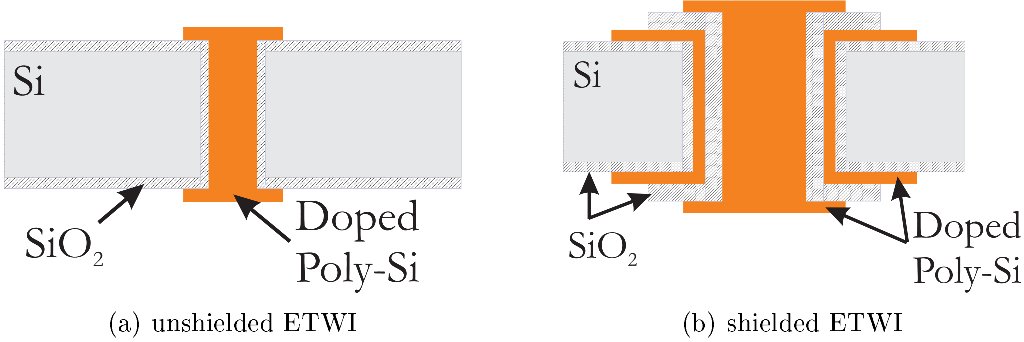

Figure D.1: Two different ETWI technologies

In the unshielded structure a single SiO_2 layer is applied to electrically isolate the poly-Si conductive channel from the Si substrate; hence an electrical capacity is created in between the Silicon wafer and the poly-Si. This type of ETWI are well suited for applications in which the capacity of the device is much larger than that of the ETWI, as is the case with the electro-optic modulation of ZnO. In the shielded ETWI type, the conducting channel is surrounded by an additional layer stack consisting of conductive poly-Si and SiO_2 to allow active isolation by grounding the outer poly-Si layer (the coaxial cable principle).

However, the additional shielding layer stack increases the complexity of the integration of the ETWI into the IO fabrication process. Therefore, LioniX and IOMS decided to use the unshielded ETWI type for the PZT-membrane demonstrator.

The fabrication of the ETWI starts with a DRIE processes to etch a trench through the entire wafer. In order to increase the aspect ratio (depth over the smallest lateral dimension) of the the trenches, the trenches are etched in two steps, first from the front side of the wafer to half of the wafer thickness, next in a similar way from the backside. Next, by an LPCVD process, a TEOS SiO_2 passivation layer is deposited on the walls of the trench and the surfaces of the wafer. One should expect as a next step the deposition of *doped* Si. Unfortunately, MESA$^+$ clean room restrictions did not allow this. So, we had to created the doped poly-Si channels in an alternative way by applying a solid-source boron-dope (SSD) as described in [TvMB$^+$05, Gro68].

After the doping procedure, the bondpads on the wafer surface are created by using a Si_RN mask and KOH etching. So, for fabrication of these ETWI we had to follow a more complicated procedure than described in [CCP$^+$02].

A photograph of a topview of a realised ETWI, as produced by LioniX, is shown in Figure D.2. Visible are the filled trench (visible as the small depression) in the centre of the large rectangular bondpad.

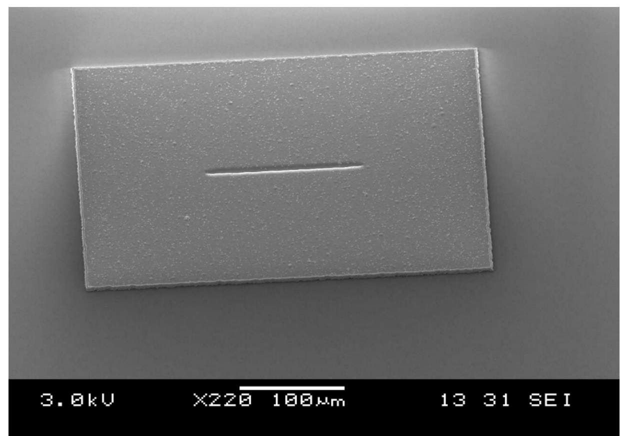

Figure D.2: SEM photograph of a realised ETWI (topview)

Lionix has produced various geometries for the ETWI: the trench width is kept constant at 10 µm, the trench length, l_{trench}, has been varied between 10 µm and 1280 µm. The electrical resistance of two sets of produced ETWI's, was measured by LioniX by depositing a 15 nm Cr/230 nm Au layer on the backside of the wafer, acting as a common electrode and then measuring the resistance between this electrode and the individual ETWI bondpad. The electrical resistance appear to be in the range between 5 Ω and 100 kΩ, being the lower the larger the trench length.

It was concluded that the above described technique is suited for creating ETWI's. The measured resistance values are comparable to the results described in [CCP+02]. Based on the experimental electrical resistance data, it was decided to use ETWI's with with a width of 10 µm and a length of 160 µm for the vibrating membrane demonstrator.

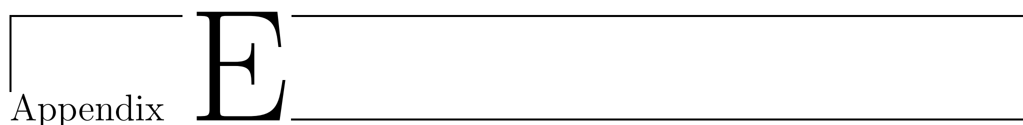

Appendix E

Processflow for the IO wafer of the attenuation based demonstrator

Table E.1: Fabrication scheme for the gyro demonstrator IO-circuit

Step	Description	Crosssections
1	Determine crystal orientation • Lithography 'crystal orientation' • BHF Etch SiO_2 • KOH etch Si Etch alignment marks • Lithography 'alignment' • BHF Etch SiO_2	
2	Create buffer tapers (in two steps) • Lithography 'buffer tapers 1' • Exposure 'buffer tapers 2' • BHF Etch SiO_2 (1.05μm) • Develop 'buffer tapers 2' • BHF Etch SiO_2 (1.05μm)	
3	Definition of the bumps • Lithography 'bumps' • BHF Etch SiO_2 (200nm)	

Continued on the next page

Table E.1: Fabrication scheme for the gyro demonstrator IO-circuit - continued

Step	Description	Crosssections
4	Apply alignment marks on backside for bond alignment • Lithography 'backside' • BHF Etch SiO_2 on backside Define surfaces for ellipsometer measurements on front side • Lithography 'backside' • BHF Etch SiO_2 (6μm) at front side	
5	Create waveguide core layer • LPCVD deposition 210nm Si_3N_4	
6	Define tapers for fiber-chip coupling • Lithography 'nitride taper' • BHF Etch Si_3N_4 (160nm)	
7	Define waveguide channels • Lithography 'waveguides' • BHF Etch Si_3N_4 (10nm)	
8	Define V-grooves in core layer (Do not strip resist from previous step!) • Lithography 'v-groove' • Etch Si_3N_4	
9	Create buffer layer • PECVD deposition 3μm SiO_2	

Continued on the next page

Table E.1: Fabrication scheme for the gyro demonstrator IO-circuit - continued

Step	Description	Crosssections
10	Transfer V-groove pattern to Si substrate • Lithography 'V-groove' • BHF Etch SiO_2	
11	Create V-grooves • Etch V-grooves • KOH Etch 100min	
12	Smoothen wafer surface for bonding • CMP	
13	Open the sensing windows • Lithography 'cladding tapers 1' • Exposure 'cladding tapers 2' • Etch SiO_2 (0.45μm) • Develop 'cladding tapers 2' • Etch SiO_2 (0.45μm)	
14	Define excitation electrodes • Lithography 'electrodes' • Sputter deposition Cr (50nm) • Sputter deposition Au (200nm) • Lift off	
15	Finalise fiber-chip coupling region • Dice V-grooves incouple plane	

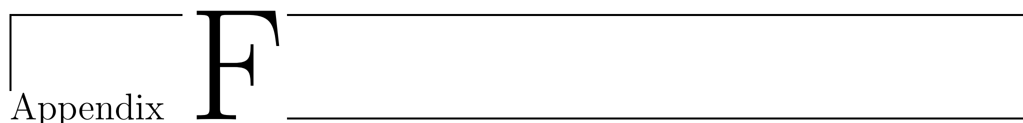

Appendix F

Processflow for creating the silicon membranes

Table F.1: Fabrication scheme for the Si membranes

Step	Description	Crosssections
1	Definition of membrane • Lithography silicon membrane definition • Deep RIE etch silicon (20μm)	
2	Deposition masking layer • Deposition LPCVD Si_3N_4 (40nm)	
3	Opening backside • Lithography backside etch • RIE etch Si_3N_4 backside	
4	Etching membrane • KOH etch backside	
5	Finalising membranes • RIE Si_3N_4 removal • Dicing into strips	

The thickenings at the edges of the membrane, as mentioned in Section 6.8, are due to way the membranes are defined in the silicon wafer (step 1). The straight-angled corners of the Si_3N_4 masking layer (marked as point 'A' in Figure F.1) act as a partial etch-stop for the KOH etch. The Si at the Si-Si_3N_4 interface (the edges of the membrane) etches away from the edges, although somewhat slower than the bulk Si. This thing (illustrated in Figure F.1) results in the triangular shaped thickenings as observed in the stylus scans shown in Section 6.8.

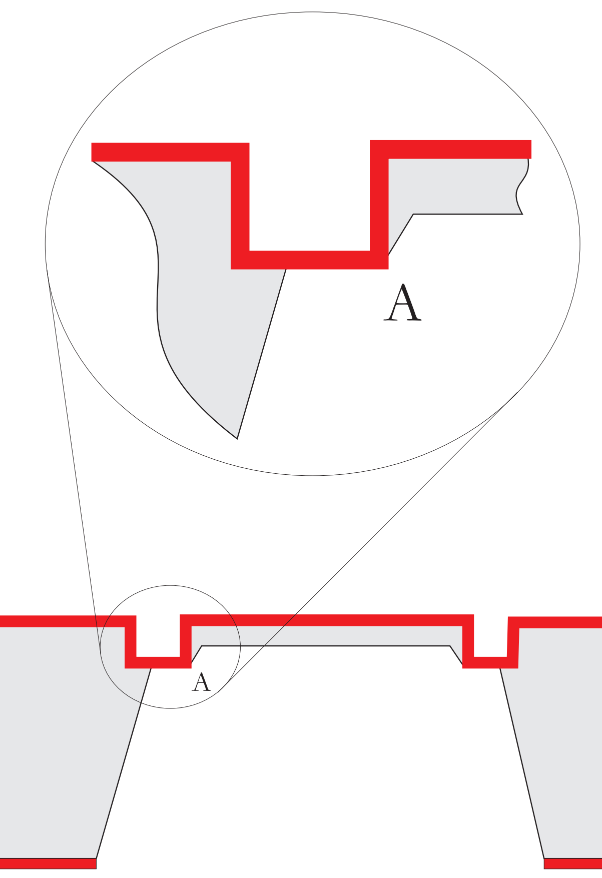

Figure F.1: Illustration of the formation of the triangular thickenings at the edges of the Si membranes

To prevent the formation of these thickenings, the definition of the membranes should have been done by KOH etching. In that case, the angles at the edges of the Si_3N_4 masking layer are smaller and no (partial) etch-stop is created. However, definition of the membranes using KOH then requires additional technological steps: KOH etch mask deposition and removal.

Bibliography

[APB+00] V.A. Aksyuk, F. Pardo, C.A. Bolle, S. Arney, C.R. Giles, and D.J. Bishop. Lucent microstar micromirror array technology for large optical crossconnects. In *Proceedings of SPIE, Vol. 4178*, pages 320–324, 2000.

[BdRWA96] T.R. Bearda, R.M de Ridder, K. Wörhoff, and P.V. Lambeck H. Albers. Stress and birefringence in pecvd sioxny waveguides. In *Proceedings IEEE/LEOS Benelux Chapter, Enschede 1996*, pages 222–225, 1996.

[C2V] C2V Software. OlympIOs, version 5.1.12. http://www.c2v.nl.

[CCP+02] E. M. Chow, V. Chandrasekaran, A. Partridge, T. Nishida, M. Sheplak, C.F. Quate, and T.W. Kenny. Process compatible polysilicon-based electrical through-wafer interconnects in silicon substrates. *Journal of Microelectromechanical Systems*, 11(6):631–640, 2002.

[CG04] C. Chao and L.J. Guo. Reduction of surface scattering loss in polymer microrings using thermal-reflow technique. *Photonics Technology Letters*, 16(6):1498–1500, 2004.

[Com] Comsol Group. Femlab/comsol multiphysics. http://www.comsol.com.

[Ş04] A. Şabac. *Etude, réalisation et caractérisation d'un microinterféromeètre de Mach-Zehnder intégré sur membrane silicium active.* PhD thesis, Université de Franche-Comté, 2004.

[DL97] R. Dangel and W. Lukosz. Electro-nanomechanically actuated integrated-optical interferometric switches. In *OSA Technical Digest Series*, volume 10, pages 170–174. OSA, 1997.

[DL98] R. Dangel and W. Lukosz. Electro-nanomechanically actuated integrated-optical interferometric intensity modulators and 2x2 space switches. *Optics Communications*, 156(1-3):63–76, 1998.

[GAG+96] C. Gui, H. Albers, J.G.E. Gardeniers, M. Elwenspoek, and P.V. Lambeck. Fusion bonding of rough surfaces with polishing technique for silicon micromachining. *Reseach Journal Micro System Technologies*, 3(3):122–128, 1996.

[GAG+97] C. Gui, H. Albers, J.G.E. Gardeniers, M. Elwenspoek, and P.V. Lambeck. Fusion bonding of rouch surface with polishing technique for silicon micro machining. *Microsystem Technologies*, 3:122–128, 1997.

[GBKN92] P. Greiff, B. Boxenhorn, T. King, and L. Niles. Silicon monolithic micromechanmical gyroscope. In *Digest of Techical Papers, Transducers 1991, San Francisco 1991*, pages 966–968, 1992.

[GKK+00] T. Gessner, S. Kurth, C. Kaufmann, J. Markert, and W. Dötzel. Micromirrors and micromirror arrays for scanning applications. In *Proceedings of SPIE, Vol. 4178, September 2000, Santa Clara, CA, USA*, 2000.

[GL97] W. Gabathuler and W. Lukosz. Electro-nanomechanically wavelength-tunable integrated optical bragg-reflectors. *Optical Communications*, 135(4-6):385–393, 1997.

[GL98] W. Gabathuler and W. Lukosz. Electro-nanomechanically wavelength-tunable integrated optical bragg-reflectors. part ii: Stable device operation. *Optical Communications*, 145(1-6):258–264, 1998.

[Gro68] A.S. Grove. *Physics and Technology of Semiconductor Devices.* John Wiley & Sons Inc., New York, USA, 1968.

[GTV96] J.G.E Gardeniers, H.A.C Tilmans, and C.C.G. Visser. LPCVD silicon-rich nirtride films for applications in micromechanics,

studied with statistical experimental design. *Journal of Vacuum Science Technology A*, 14(5):2879–2892, 1996.

[GVK+98] C. Gui, G.J. Veldhuis, T.M. Koster, P.V. Lambeck, J.W. Berenschot, J.G.E. Gardeniers, and M. Elwenspoek. Nanomechanical optical devices fabricated with aligned wafer bonding. In *Proceedings of the IEEE Micro Electro Mechanical Systems (MEMS)*, pages 482–487, 1998.

[Hes99] M. Heschel. *Multiple through-wafer interconnects for stacking of microelectromechanical devices.* PhD thesis, Lyngby: MICŮMikroelektronik Centret, Technical Univ. Denmark, 1999.

[HL97] R.G. Heideman and P.V. Lambeck. Simple and reusable fibre-to-chip interconnection with adjustable coupling efficiency. *Proceedings of SPIE*, 3099, 1997.

[HL99] R.G. Heideman and P.V. Lambeck. Remote opto-chemical sensing with extreme sensitivity: design, fabrication and performance of a pigtailed integrated optical phase-modulated Mach-Zehnder interferometer system. *Sensors and Actuators B*, 61:100–127, 1999.

[HvSK93] H.J.W.M. Hoekstra, J.C. van't Spijker, and H.M.M. Klein Koerkamp. Ray picture for prism-film coupling. *Journal of the Optical Society of America A*, 10(10):2226–2230, 1993.

[Kos00] T.M. Koster. *TE/TM based integrated optical sensing platforms.* PhD thesis, University of Twente, 2000.

[Kro54] R. Kronig. *Leerboek der natuurkunde.* Scheltema & Holkema, 1954.

[LDG] University of Twente 'Lighwave Device Group. ATRguide.

[Luk92] W. Lukosz. Integrated optical nanomechanical devices as modulators, switches and tunable wavelength filters and as acoustical sensors. In *Proceedings of SPIE, Vol. 1793*, pages 214–234, 1992.

[Mat] The Mathworks Inc. Matlab. http://www.mathworks.com.

[McD] McDaggah & O'Laughlain. Simulayer. http://daglain.com/.

[MGCM88] W.P. Maszara, G. Goetz, A. Caviglia, and J.B. McKitterick. Bonding of silicon wafers for silicon-on-insulator. *Journal of Applied Physics*, 64(10):4943–4950, 1988.

[Pet90] D. Peters. *Herstellung und untersuchung von PECVD-Siliziumoxinitrideschichten für die integrierte optik*. PhD thesis, Technischen Universität Hamburg-Harburg, 1990.

[PL91] P. Pliska and W. Lukosz. Integrated optical interferometer as a light modulator and microphone. *Sensors and Actuators A*, 26(1-3):337–340, 1991.

[PL94] P. Pliska and W. Lukosz. Integrated optical acoustical sensors. *Sensors and Actuators A*, 41-42(1-3):93–97, 1994.

[TEF91] H.A.C Tilmans, M. Elwenspoek, and J.H.J. Fluitman. Micro resonant force gauges. *Sensors and Actuator A*, 30:35–53, 1991.

[TL94a] H.A.C Tilmans and R. Legtenberg. Electrostatically driven vacuum-encapsulated polysilicon resonators. part i. design and fabrication. *Sensors and Actuators A*, 45:57–66, 1994.

[TL94b] H.A.C Tilmans and R. Legtenberg. Electrostatically driven vacuum-encapsulated polysilicon resonators. part ii. theory and performance. *Sensors and Actuators A*, 45:67–84, 1994.

[TvMB+05] R.M. Tiggelaar, P. van Male, J.W. Berenschot, J.G.E. Gardeniers, R.E. Oosterbroek, M.H.J.M. de Croon, J.C. Schouten, A. van den Berg, and M.C. Elwenspoek. Fabrication of a high-temperature microreactor with integrated heater and sensor patterns on an ultrathin silicon membrane. *Sensors and Actuators A*, 119(1):196–205, 2005.

[Vel98] G.J. Veldhuis. *Bent-waveguide Devices and Mechano-optical Switches*. PhD thesis, University of Twente, 1998.

[vL05] J. van Lith. *Novel integrated optical sensing platforms for chmical and immuno-sensing*. PhD thesis, University of Twente, 2005.

[vLLH+05] J. van Lith, P.V. Lambeck, H.J.W.M. Hoekstra, R.G. Heideman, and R.R. Wijn. The segmented waveguide sensor: principle and experiments. *Journal of Lightwave Technology*, 23(1):355–363, 2005.

[VPHL00] G.J. Veldhuis, O. Parriaux, H.J.W.M. Hoekstra, and P.V. Lambeck. Sensitivity enhancement in evanescent optical waveguide sensors. *Journal of lightwave technology*, 18(5):677–682, 2000.

[WDL+99] K. Wörhoff, A. Driessen, P.V. Lambeck, L.T.H. Hilderink, P.W.C. Linders, and Th.J.A. Popma. Plasma enhanced chemical vapor deposition silicon oxynitride optimized for application in integrated optics. *Sensors and Actuators A: Physical*, 74(1-3):9–12, 1999.

[WLA+97] K. Wörhoff, P.V. Lambeck, H. Albers, O.J.F. Noordam, N.F. van Hulst, and T.J.A. Popma. Optimisation of lpcvd silicon oxynitride growth to large refractive index homogeneity and layer thickenss uniformity. In *Proceedings of SPIE, Vol. 3099*, pages 257–268, 1997.

[Wör96] K. Wörhoff. *Optimised LPCVD SiO_xN_y waveguides covered with calixarene for non-critically phase-matched second harmonic generation.* PhD thesis, University of Twente, 1996.

[YAN98] N. Yazdi, F. Ayazi, and K. Najafi. Micromachined inertial sensors. In *Proceedings of the IEEE*, volume 86, pages 1640–1659, 1998.

Publications

- G. Altena, M. Dijkstra, G. van Elzakker, G. Venhorst, P.V. Lambeck, and H.J.W.M. Hoekstra. *A novel moems device: Detection of MEMS movements using free-standing Si_3N_4 suspended optical waveguides.* In Proceedings of the 8th Annual Symposium IEEE/LEOS Benelux Chapter, pages 25-28, University of Twente, Enschede, The Netherlands, November 2003. IEEE/LEOS Benelux Chapter.

- G. Altena, M. Dijkstra, G. van Elzakker, G. Venhorst, P.V. Lambeck, and H.J.W.M. Hoekstra. *Ultra-thin free-standing Si_3N_4 membrane waveguides for application in evanescent field sensing of MEMS movements.* In Book of Abstracts Seventh European Conference on Optical Chemical Sensors and Biosensors EUROPT(R)ODE VII, page 57, Madrid, Spain, April 2004. Complutense University, Madrid, Spain.

- G. Altena, M. Dijkstra, H.J.W.M. Hoekstra, and P.V. Lambeck. *Ultra-thin free-standing Si_3N_4 membrane waveguides for evanescent sensing of MEMS movements.* In Book of Abstracts 12th European Conference on Integrated Optics (ECIO), pages 506-509, Grenoble, France, April 2005.

- R.M. de Ridder, G. Altena, D.H. Geuzebroek, and R. Dekker (editors). *Proceedings of the Annual Symposium 2003 IEEE/LEOS 2003.* IEEE/LEOS Benelux Chapter c/o University of Twente, Faculty of Electrical Engineering, Mathematics and Computer Sciences, November 2003.

- J. van Lith, G. Altena, H.J.W.M. Hoekstra, M. Dijkstra, R. Wijn, and P.V. Lambeck. *Integrated optical sensors.* In MESA+ Annual Meeting, Enschede, The Netherlands, October 2003. University of Twente.

- H.J.W.M. Hoekstra, P.V. Lambeck, G. Altena, J. van Lith, M. Dijkstra, and R. Wijn. *Novel integrated optic sensors.* In Proceedings

Conference 'Sense of Contact', Wageningen, The Netherlands, March 2005. F.H.I. ISBN: 90-74702-51-1.

- G. Altena, J. van Lith, and R.R. Wijn. *Novel integrated optic sensors.* In MESA+ Annual Meeting, Enschede, The Netherlands, September 2005. University of Twente.

- G. Altena, M. Dijkstra, H.J.W.M. Hoekstra, and P.V. Lambeck. *Accurate displacement sensing with integrated optics.* In International Symposium in Modern Optics and Its Applications, pages 15-20, Bandung, Indonesia, August 2005.

Samenvatting (Dutch)

In dit hoofdstuk worden de belangrijkste resultaten uit de vorige hoofdstukken samengevat en word een algemene evaluatie van het onderzoek gegeven.

Samenvatting van de belangrijkste resultaten

Hoofdstuk 1: Voorwoord Het onderzoek dat beschreven is in dit proefschrift was onderdeel van het Europese GROWTH poject 'Optical Characterisation Methods for MEMS manufacturing (OCMMM)'. Het doel van dit project was het ontwikkelen van methoden voor het meten van mechanische uitwijkingen in MEMS systemen. Deze methoden zijn onderverdeeld in de zogenaamde 'full-field' en 'on chip' methoden. Beide type methoden worden kort beschreven en de deelnemende partners in het project worden gepresenteerd. Het onderzoek beschreven in dit proefschrift was een onderdeel van de 'on chip' methoden.

Hoofdstuk 2: Introduktie Een korte introduktie over geïntegreerde optica (IO) word gegeven waarbij de nadruk ligt op de beschrijving van een geïntegreerd optische Mach-Zehnder Interferometer (MZI). Dit type interferometer zal een centrale role spelen in de 'on chip' methoden. De 'on chip' methoden worden onderverdeeld in twee klasses: 'loaded' systemen waarbij het IO systeem en het MEMS systeem monolitisch geïntegreerd zijn en de 'unloaded' systemen waarbij de IO systemen en MEMS systemen in afzonderlijke silicium wafers gerealiseerd worden en vervolgens middels een hybride integratie gecombineerd worden. Dit proefschrift behandeld verschillende 'unloaded' MOEMS system waarin de uitlezing van de mechanische uitwijkingen gebaseerd is op evenescente veld meetmethoden.

Drie prototypes zijn gepland waarbij verschillende MEMS systemen worden bemeten: een electrostatisch aangedreven roterende microspiegel, een piëzoelectische aangedreven vibrerend membraan en een

micromechanische gyroscoop. Van elk prototype worden kort de fabricage methoden, toepassingen en betrokken partners alsmede hun taken besproken. De hoofdtaken binnen dit promotieonderzoek behelzen het analyseren en ontwikkelen van de evanescent veld meetmethoden, het ontwerpen, realiseren en karakteriseren van de benodigde IO structuren, het integreren van deze IO structuren met de MEMS systemen en het karakteriseren van de gerealiseerde MOEMS prototypes.

Hoofdstuk 3: Theorie Bij meetsystemen gebaseerd op de evanescent veld meetmethode drijft men het bewegende onderdeel van de MEMS in het evanescente veld van de lichtmodus welke in het IO systeem propageert. De variatie van de afstand tussen het bewegende MEMS onderdeel en de bovenkant van het golfgeleiderkanaal beïnvloedt een aantal eigenschappen van de lichtmodus welke in het kanaal propageert. Voor meting van verplaatsing kan vooral de invloed op de effectieve brekingsindex, N_{eff}, benut worden. Twee extrema worden hierbij onderscheiden: een waarbij de verandering van het reele deel van N_{eff} dominant is en een ander waarbij de verandering van het imaginaire deel overheerst. Het eerste extreem resulteert in een lokale verandering van de voortplantingssnelheid van de lichtmodus en de bijbehorende meetmethode word 'refractief' genoemd; het tweede extreem resulteert in een lokale demping van de lichtmodus en de bijbehorende meetmethode word 'absorbtief' genoemd. Beide meetmethoden zijn zowel kwalitatief als kwantitatief onderzocht. Voor de kwantitatieve kant van het onderzoek is een benaderend model gebaseerd op het stralenmodel van licht beschreven en toegepast.

Op voorhand was vastgelegd dat de SiON technologie zoals ontwikkeld door de IOMS groep van het MESA+ onderzoeksinstituut gebruikt zou gaan worden. Een standaard tweelaags monomodale SiON golfgeleider, bestaande uit een Si_3N_4 kernlaag en een SiO_2 bufferlaag heeft een vrij beperkt meetbereik voor de beschreven bewegingen: ongeveer 0.5 µm- 1.5 µm. Echter, met de SiON technologie kunnen ook lokaal vrijstaande golfgeleiders gemaakt worden, deze golfgeleiders bestaan uit bijvoorbeeld een 100 nm dikke Si_3N_4 laag welke aan twee kanten omgeven is door lucht. Bij dit type golfgeleiders is, bij gebruik van een golflengte van 1550 nm en TM polarisatie, een meetbereik haalbaar tot ongeveer 11 µm- 15 µm.

Hoofdstuk 4: Vrijdragende (membraan) golfgeleiders De fabricage van vrijdragende golfgeleiders welke aan elke zijde vast zitten aan de

bulk van het substraat en welke bestaan uit stoiciometrisch silicium-nitride, Si_3N_4 (tensiele materiaal spanning) of silicium-rijk silicium-nitride, Si_RN (compressieve materiaal spanning), is onderzocht. Een BHF etsprocess op verhoogde temperatuur is ontwikkeld om op een snelle manier ongeveer 200 nm Si_3N_4 of Si_RN te etsen zonder noemenswaardige aantasting van de beschermende fotolithografishe lak. Door het aanpassen van de hechting tussen de lak en de Si_3N_4 laag zijn graduele overgangen (zogenaamde *tapers*) met taperhoeken van ongeveer 0.3° gecreëerd tussen de ongeetste, 300 nm dikke, delen van de kernlaag en de geetste, 100 nm dikke, delen. Door deze overgangen is een praktisch verliesvrije propagatie mogelijk tussen de dikke en dunne delen van de kernlaag en vice-versa.

Miet een KOH ets process waarbij lokaal het SiON lagenpakket aan de achterkant van de wafer is verwijderd, zijn vrijdragende membranen gerealiseerd met diktes van 20 nm en hoger en een oppervlak van enkele vierkante millimeters bij een opbrengst van bijna 100%. De Si_RN membranen met een dikte beneden de 45 nm vertonen onverwachte rimpelingen van het oppervlak wat wijst op een compressieve spanning in het materiaal. De membranen van Si_3N_4 zijn volledig vlak hetgeen te danken is aan de tensiele spanning. Door het etsen is de oppervlakte ruwheid van de Si_3N_4 lagen verhoogd. Door het vergelijken van de optische verliezen van golfgeleiders met en zonder zulke membranen zijn de membraan-geïduceerde verliezen voor de fundamentele TE en TM modus vastgesteld op respectievelijk 2.6 dB en 8 dB.

Hoofdstuk 5: Het elektrostatisch aangedreven spiegel prototype

De structuur en de relevante eigenschappen van het elektrostatisch aangedreven microspiegelsysteem, zoals geproduceerd door de Technische Universiteit van Chemnitz, worden beschreven, alsmede de vereisten aan de uitlezing. Door de afmetingen van de spiegels, gecombineerd met hun maximale rotatiehoek van 2.5°, zijn we genoodzaakt om in de optisch wafer grote gaten te defineren naast de golfgeleider structuur om de vrije beweging van de spiegel mogelijk te maken. Dit kan bereikt worden door gebruik te maken van vrijdragende golfgeleiders welke ter versteving aan weerszijden ondersteund worden door een smalle silicium brug. Twee methoden om een dergelijk brugsysteem te fabriceren zijn onderzocht: bij de eerste methode zijn er sleuven geetst aan de voorzijde van de wafer en word middels KOH etsen door deze sleuven het Si onder de kernlaag verwijderd; bij de tweede methode word het Si weggeetst door openingen in de SiON

lagen aan de achterkant van de wafer. Experimentele resultaten resulteren in een voorkeur voor de laatste methode.

Om de rotatiehoek uit te lezen is gekozen voor het toepassen de refractieve uitleesmethode met een MZI. Een ontwerp voor de IO structuur is gemaakt met inachtneming van de eisen aan de ruimetelijke en technologische compatibiliteiten van MEMS en IO structuur. Hoewel een van de uitgangspunten het behoud van de integriteit van het MEMS systeem was, waren kleine veranderingen aan de MEMS noodzakelijk om de hybride integratie met de IO wafer mogelijk te maken.

De IO wafers zijn gerealiseerd en gekarakteriseerd. Uitgaande van inleidende experimenten zijn de MEMS wafer en IO wafer gecombineerd door 'direct' waferbonding. De resulterende structuur is vervolgens middels een verlijmingsprocess voorzien van en Pyrex wafer waarop zich de aansturings electroden bevinden. Twee series MOEMS systemen zijn gerealiseerd. De eerste serie bleek, na het waferbonden, goed uitgelijnd te zijn en vertoonde geen verkleving van spiegel en membraan. Echter, tijdens het verzagen van het systeem liet de Pyrex wafer los van de rest van het systeem hetgeen resulteerde in de vernietiging van alle spiegel systemen. In de tweede serie werden de wafers verzaagd voor combinatie met de Pyrex wafer. Na verzaging zijn alle individuele '1 systeem' delen voorzien van een electrode-onderdeel. Helaas bleken alle brugstructuren van de IO wafer de spiegel te raken. Onder de microscoop leken de bruggen enigszins gebogen en dit wijten we aan spanningen in het silicium van de brug. Het aanbrengen van een grote gelijkspanning heeft niet geleid tot scheiding van spiegel en brug. Desondanks zijn er een aantal experimenten met deze systemen uitgevoerd: tijdens het aanbrengen van een aandrijfspanning zijn zowel het optische uitgangssignaal als de orientatie van de spiegel gemeten. Doordat de onderlinge afstand tussen spiegel en brug niet gemeten kon worden door de afwezigheid van geschikte apparatuur konden de experimentele resultaten niet vergeleken worden met de verwachte theoretische waarden.

Hoofdstuk 6: Het piëzoelektrisch aangedreven membraan prototype De relevante eigenschappen van het membraan worden gegeven, de topologie van de MEMS wafer is ontworpen en de vereisten aan het prototype zijn vastgesteld. Het MOEMS systeem zal van het refractieve type zijn. Het ontwerp van de IO wafer is voorzien van serrodyne gemoduleerde MZI's en de laterale layout komt overeen met die van de MEMS wafer. Door de beperkte beschikbare ruimte op

de MEMS wafer zijn er gebogen MZI's ontworpen en een speciaal schaduwmasker is ontwikkeld dat het lokaal deponeren van ZnO in een bochtstructuur mogelijk maakt. Om de elektrische verbindingen voor de modulator aan de achterkant van de wafer mogelijk te maken zijn zogenaamde Electrical Through Wafer Interconnects (ETWI's) voorgesteld. Helaas kon het MOEMS systeem niet gerealiseerd worden vanwege vervuiling van de oppervlak van de MEMS wafer welke geproduceerd word door projectpartner Thales-RT. Deze vervuiling bleek niet verwijderd te kunnen worden en maakte het bonden van de wafers onmogelijk.

Hoofdstuk7: De MEMS gyroscoop In een MEMS gyroscoop van het vibratie-type manifesteert een rotatie van de gyroscoop om een gegeven as zich als een, in fase tegengestelde, beweging van twee silicium platen in de richting loodrecht op het eindvlak van het MEMS systeem. Op het eerste gezicht lijkt het meetprobleem sterk op dat van het spiegelsysteem. Echter, de verplaatsing van beide platen ligt in de orde grootte van 1 nm, ongeveer 3 ordes van grootte kleiner dan bij de spiegel. Dus, in plaats van het realiseren van een groot meetbereik is de nadruk bij dit systeem gelegd op het verkrijgen van een hoge resolutie.

Drie meetconfiguraties zijn geanalyseerd: twee types gebaseerd op refractief meten met een MZI en een gebaseerd op absorptieve metingen. De uitkomst was dat de drie configuraties vergelijkbare gevoeligheden hadden. Uiteindelijk werd besloten om de absorptieve variant te gebruiken, voornamelijk om bekend te geraken met deze meetmethode en de daarmee gerelateerde problemen. Berekeningen leerden dat een standaard golfgeleider structuur en bij gebruik van TE gepolariseerd licht met een golflengte van 1550 nm een goede kandidaat was.

In zo'n gyroscoop worden rotaties omgezet naar een beweging in de vertical richting als een gevolg van de Coriolis krachten die werken op de horizontaal bewegende vibrerende massa's. In onze experimenten wilden we ons concentreren op het meten van de kleine uitwijkingen van deze massa's en daarom werd er besloten om deze uitwijkingen te genereren op een minder ingewikkelde manier: door middel van electrostatische krachten.

De relevante eigenschappen van de gyroscoop en de randvoorwaarden en eisen aan het systeem zijn gegeven door Thales-Av. Een ontwerp voor de IO structuur dat compatibel is met dat van de gyroscoop is gemaakt. De integriteit van het MEMS systeem kon niet geheel be-

houden blijven, een aantal kleine veranderingen zijn voorgesteld aan Thales-Av. Het fabricageprocess voor de IO systemen is gedefineerd en de IO systemen zijn vervolgens gemaakt. Echter, het bondoppervlak van de door Thales-Av gemaakte MEMS wafer bleek verontreinigd te zijn met onbekende deeltjes welke niet verwijderd konden worden met de in de MESA$^+$ cleanroom beschikbare schoonmaak methoden. Deze verontreinigingen maakten het bonden van de MEMS wafers op de IO wafer onmogelijk. Er is vervolgens besloten om de gyroscoop te vervangen door andere mechnische structuren die voorzien in een goed gecontrolleerde vertikale beweging: een vibrerend, electrostatisch aangedreven Si membraan en een piëzo-elektrisch aangedreven silicium plaat. Door imperfecties in de Si membranen hadden de metingen hiermee een louter kwalitatief karakter; een vergelijk met de verwachtte theoretisch waarden bleek onmogelijk. Experimentele resultaten verkregen van het systeem met de piëzo-elektrisch aangedreven Si plaat leverden een redelijk goede overeenkomst met de theoretische berekeningen.

Algemene evaluatie van het onderzoek gepresenteerd in dit proefschrift

We hebben moeten constateren dat de doelen die voor dit vierjarige project gesteld waren te ambitieus waren. Echter, projecten zonder hoge ambities scoren over het algemeen slecht in Europese programma's. Tijdens de verschillende onderdelen van het onderzoek zijn we tegen problemen aangelopen welke niet voorzien waren bij aanvang van het project. In het bijzonder presteerden de mechanische structuren, de MEMS, hetzij geleverd door de projectpartners, hetzij door onszelf gemaakt, niet naar verwachting. Door mechanische spanningen in de materialen weken de verwachtte initiele vormen van de systemen af van de vormen zoals aangenomen bij het ontwerp. Ook kwamen tijdens aansturing van de MEMS systemen parasitaire bewegingen en deformaties voor welke de theoretisch verkregen relatie tussen deze bewegingen en hun optische effect verstoorden. Helaas waren zogenaamde 'full field' optische methoden om deze parasitaire bewegingen en deformaties te meten niet beschikbaar zodat er enkel kwalitatieve en semi-kwantitatieve conclusies getrokken konden worden. Ook kon er niet geheel voldaan worden aan de eisen welke gesteld waren aan de wafer bonding: verontreinigingen van de bond-oppervlakken van de MEMS structuren welke geleverd werden door verschillende projectpartners en te hoge waferkrom-

mingen verstoorden de fabricage van de hybride MOEMS systemen. Tevens werden de benodigde MEMS structuren vaak niet op tijd geleverd door de partners. Dus, terugkijkend, heeft het onderzoek een meer aftastend karakter gehad in plaats van dat er een duidelijk signaal is afgegeven over het potentieel van de evanescent veld meetmethoden.

Desalnietemin is er een aanzienlijke voortgang geboekt. Er ligt een theoretische basis voor MOEMS systemen met evanescent veld uitlezing. Er is meer inzicht verkregen in het potentieel en beperkingen van de evanescent veld meetmethode, zowel van het refractieve als van het absorptieve type. De belangrijkste problemen zijn vastgesteld en een aantal van deze zijn opgelost.

We kunnen concluderen dat het meetbereik van MEMS uitwijkingen enorm vergroot kan worden door het toepassen van vrijdragende golfgeleiders in de meetsectie van de IO structuur. Bij gebruik van een TM_0 modus, een golflengte van 1550 nm en een vrijdragende Si_3N_4 golfgeleider met een dikte van 100 nm kan een meetbereik tot 11 µm gehaald worden. Dunnere golfgeleiders maken nog grotere bereiken mogelijk.

Een methode voor het fabriceren van vrijdragende golfgeleiders in SiON technologie is ontwikkeld en membraan diktes zo dun als 30 nm kunnen gemaakt worden met een opbrengst van bijna 100%. Deze golfgeleiders zijn niet alleen geschikt voor dit type optische uitlezing maar ook voor absorptieve sensoren met een relatieve gevoeligheid groter dan 1 zoals beschreven is in [VPHL00]. Tevens is een methode om verzaagde delen van wafers te bonden ontwikkeld en zijn methodes verbeterd voor het verkrijgen van verticale tapers met kleine hoeken welke verliesvrije overgangen tussen golfgeleidersecties van verschillen diktes mogelijk maken. Als een piëzo-elektrisch aangedreven silicium plaat in het evanescente veld van de meetsectie gedreven word corresponderen de gemeten optische signalen (gebaseerd op het absorptieve effect) goed met de theorie.

Echter, voor het realiseren van een evanescent veld uitleesmethode voor bewegingen van MEMS-onderdelen welke kan concurreren met de huidige capacitieve uitleesmethoden, of deze zelfs voorbij van streven, is nog nog veel meer onderzoek nodig. In het bijzonder behoeven de problemen gerelateerd aan de imperfectie van de vorm en beweging van de MEMS meer aandacht. Merk op overigens dat het evanescent veld uitlezen van mechanische *frequenties* niet belemmerd word door deze imperfecties en dit verdiendt speciale aandacht in toekomstig onderzoek.

Dankwoord

De voorgaande hoofdstukken zijn het resultaat van de afgelopen vier, vijf jaar die ik aan de UT heb doorgebracht. Deze laatste bladzijden beslaan echter een periode die beduidend langer was dan die vier, vijf jaar. Als ik het niet zo naar mijn zin had gehad in deze periode had ik waarschijnlijk de eerste zin van deze alinea nooit hoeven schrijven. Dus, voor iedereen die het mogelijk heeft gemaakt dat ik die eerste zin *wel* heb mogen schrijven,

Bedankt en Houdoe!

Dit geeft goed de strekking weer wat er in de rest van deze bladzijden geschreven gaat worden en het laat zien dat ik inmiddels redelijk goed ben ingeburgerd in Eindhoven.

Allereerst wil ik beginnen met het bedanken van de IOMS leden van het OCMMM-team. Mijn promotor Paul Lambeck, ik heb erg veel van je geleerd. Ik wil je bedanken voor je erg nuttige opmerkining en voor je geduld als dingen soms niet helemaal liepen zoals ze hoorden. Hugo Hoekstra, mijn assistent-promotor, ook jou wil ik hartelijk bedanken voor je hulp bij allerhande mathematische vraagstukken. Ook je rust en kalmte was erg welkom tijdens de hectische momenten. Als laatste natuurlijk Meindert. Ik denk niet dat iemand zich een betere cleanroomtechnoloog kan wensen. Ik ben erg blij met de resultaten die we samen bereikt hebben!

Ook de rest van mijn Europesche OCMMM-collega's wil ik bedanken voor de samenwerking en de gastvrijheid tijdens de projectvergaderingen. In het bijzonder moet ik Andreas Bertz en Rolf Hoffmann van de TU Chemnitz noemen voor hun werk aan de spiegel-demonstrator, Rolf und Andreas, hertzligen dank! Verder ook de mensen van LioniX: Melis Jan, Marcel, René en Hans, bedankt voor de prettige samenwerking.

Naast Paul en Hugo nemen Dr. Krijnen, prof. Popma, prof. Driessen en Dr. Gorecki zitting in mijn promotiecommissie. Ook hen wil ik langs deze weg bedanken voor hun bijdrage.

De (ex-)collega's van de Lightwave Devices Group, de Integrated Optical

MicroSystems groep mogen ook niet ontbreken in dit dankwoord. Allereerst mijn mede-AIO's, bedankt voor de uiterst fijne werksfeer, de congresbezoeken, borrels en beroemde IOMS indoor Kerst Borrel-BQs. Douwe, Arne (JA!), Henri, Henry (wanneer gaan we BBQ-en?), Freddy, Murali, Ronald (bedankt voor je speciale 'versie-voor-Geert' variant van SimuLayer), Edwin, Wico, Didit, Joris (G'day!), Cazimir, Gamar, Ton (terug van weggeweest), allen hartelijk bedankt voor de leuke afgelopen jaren. Hardewarenspecialisten Henk en Anton, zonder jullie had ik vast vaak met de handen in het haar gezeten, ik ben blij dat ik her en der wat dingen terug heb kunnen doen voor alle moeite die jullie gedaan hebben. Voorts wil ik natuurlijk ook de rest van de IOMS groep bedanken: Gabriël, Kerstin, Rita, Mart, Lucy, Chris, Dion, Marcus, Iwan, Sami, Feridun, Jonathan (succes met met je Nederlands!) en René, bij deze. Als laatste wil ik Gunter Venhorst en Gijs van Elzakker noemen omdat ze het aangedurft hebben om bij mij hun afstudeeropdracht te doen. Heren, bedankt.

Nu moet ik terugkomen op de tweede zin van deze bladzijde, er is meer dan alleen werk namelijk. Tijdens mijn tijd aan de UT heb ik een stel geweldige vrienden gemaakt. Ik ga ze niet allemaal noemen, jullie weten wie jullie zijn! Piranha Onderwaterhockey, heel veel dank voor de geweldige tijd, de borrels, uitjes en de soms broodnodige 'verstand op nul, blik op oneindig' afreageermomenten. De voltallige Mono- en Global clan. Eerst alleen op de UT, nu door heel Nederland en zelf daarbuiten. Ik ga er vanuit dat we op dezelfde toer doorgaan. Verder, het vaste meubilair van de VriMiBo, bedankt voor de erg fijne weekafsluitingen.

Xiaoxin wil ik bedanken voor haar steun, geduld en liefde. We zullen nog even heen en weer moeten reizen tussen Enschede en Eindhoven maar dat komt vast wel goed.

Als laatste wil ik mijn ouders en mijn zus bedanken. In de afgelopen jaren heb ik altijd op ze kunnen rekenen, voor alles, zelfs in de afgelopen donkere tijden. Pa, ma, Marieke, bedankt, voor alles.

Geert.

Biografie

Geert Altena werd geboren in Doetinchem op 26 Maart 1974 en hij groeide op in Steenderen. Hij volgde de VWO-opleiding aan het Stedelijk Lyceum (thans Stedelijk Daltoncollege) te Zutphen. Hierna begon hij aan de universitaire opleiding Technische Natuurkunde aan de Universiteit van Twente in Enschede. Deze studie rondde hij af in november 2000 met een afstudeeropdracht bij de vakgroep 'Lightwave Devices Group' (thans 'Integrated Optical MicroSystems'), naar een geïntegeerd optische luchtvochtigheidssensor. Hierna begon hij met het promotieonderzoek 'Evanescent field sensing in hybrid integrated optical MEMS devices' aan dezelfde vakgroep, onder leiding van professor Paul Lambeck. Thans is hij werkzaam als onderzoeker bij IMEC-NL te Eindhoven.

In zijn vrije tijd is Geert voornamelijk in de buurt van water (in zowel vloeibare als vaste vorm) te vinden voor onderwaterhockey, sportduiken, freediving en snowboarden.